School of Engineering and Material Science,

Queen Mary, University of London

Finite Block Method and Applications in Engineering with Functional Graded Materials

Chao SHI

Thesis submitted to the Queen Mary University of London for the degree of

Doctor of Philosophy

Queen Mary and Westfield College

University of London

Mile End Road

London E1 4NS,UK

Declarations

I, Chao SHI, confirm that the research included within this thesis is my own work or that where it has been carried out in collaboration with, or supported by others, that this is duly acknowledged below and my contribution indicated. Previously published material is also acknowledged below.

I attest that I have exercised reasonable care to ensure that the work is original, and does not to the best of my knowledge break any UK law, infringe any third party's copyright or other Intellectual Property Right, or contain any confidential material.

I accept that the College has the right to use plagiarism detection software to check the electronic version of the thesis.

I confirm that this thesis has not been previously submitted for the award of a degree by this or any other university.

Signature:

Date:

Acknowledgements

Firstly, I would like to thank my supervisor *Dr Pihua Wen*, School of Engineering and Material Science at Queen Mary, University of London. His professional knowledge, serious attitude and emotions against research guided and supported me a lot during my four years study. Without his drive and patience for explaining the problems I met, completing this research would have been very difficult.

Secondly, I would like to express my warm gratitude to number of my colleagues, *Dr Xuejiao Huang* and *Mr Perry Hinneh* who are also students of Dr Pihua Wen. In addition, I would like to express my gratitude to the staff of School of Engineering and Material Science.

Thirdly, I am also grateful to *Dr Weizhi Liu* and *Dr Miao Lin*, and all other friends for all the support and encouragement.

Last but not the least, I would like to show my gratitude to my parents and my wife as well. In my four years study, they provide me with unfailing support and continuous encouragement through the process of researching and writing this thesis. This accomplishment would not have been possible without them. Thank you

Chao SHI

Abstract

Fracture mechanics plays an important role in understanding the performance of all types of materials including Functionally Graded Materials (FGMs). Recently, FGMs have attracted the attention of various scholars and engineers around the world since its specific material properties can smoothly vary along the geometries.

In this thesis, the Finite Block Method (FBM), based on a 1D differential matrix derived from the Lagrangian Interpolation Method, has been presented for the evaluation of the mechanical properties of FGMs on both static and dynamic analysis. Additionally, the coefficient differential matrix can be determined by a normalized local domain, such as a square for 2D, a cubic for 3D. By introducing the mapping technique, a complex real domain can be divided into several blocks, and each block is possible to transform from Cartesian coordinate (xyz) to normalized coordinate ($\xi\eta\varsigma$) with 8 seeds for two dimensions and 20 seeds for three dimensions. With the aid of coefficient differential matrix, the differential equation is possible to convert to a series of algebraic functions. The accuracy and convergence have been approved by comparison with other numerical methods or analytical results.

Besides, the stress intensity factor and *T*-stresses are introduced to assess the fracture characteristics of FGMs. The Crack Opening displacement is applied for the calculation of the stress intensity factor with the FBM. In addition, a singular core is adopted to combine with the blocks for the simulation of *T* stresses. Numerical

examples are introduced to verify the accuracy of the FBM, by comparing with Finite Element Methods or analytical results.

Finally, the FBM is applied for wave propagation problems in two- and three-dimensional porous mediums considering their poroelasticities. To demonstrate the accuracy of the present method, a one-dimensional analytical solution has been derived for comparison.

Table of Contents

List of Tables

List of Figures

Abbreviations

FGM	Functionally Graded Material
ODE	Ordinary Differential Equations
PDE	Partial Differential Equations
FDM	Finite Differential Method
FEM	Finite Element Method
FVM	Finite Volume Method
SIFs	Stress Intensity Factors
NDT	Non-Destructive Testing
NRL	Naval Research Laboratory
COD	Crack Opening Displacement
LEFM	Linear Elastic Fracture Mechanics
SPH	Smooth Partial Hydrodynamics
DEM	Diffuse Element Method
MLPG	Meshless Local Petro-Galerkin
RKPM	Reproducing Kernel Particle Method
RBF	Radial Basis Functions
MLS	Moving Least Square
PIM	Point Interpolation Method
LRPIM	Local Radial Point Interpolation Methods

FBM	Finite Block Method
UV	ultraviolet
BEM	Boundary Element Method
MCC	Modified Crack Closure
DCT	Displacement Correlation Technique
GKS	Generalized Kelvin Solution
EFEM	Extended Finite Element Method
EFG	Element Free Galerkin
WBM	Wave Based Method
CQM	Convolution Quadrature Method

Nomenclature

Π	Potential Energy
W_s	Energy needed to create a new surface
γ_s	Surface energy
r	Radius
θ	Angle
μ	Shear modulus
U, V	Displacement and velocity for initial conditions
$\mathbf{D}_x, \mathbf{D}_y$	Partial differential matrix
b_x, b_y	Body force
a	Crack length
A, B	Coefficients for William series
E, G	Young's and shear modules
$H(t)$	Heaviside function
l	Number of samples in Laplace domain
M, N	Number of seeds in FBM
$n(n_x, n_y)$	Vector normal to the boundary
(ξ, η)	Normalized coordinate system
(r, θ)	Polar coordinate system

r_0	Size of singular core
R	Radius of disk
s_l	Laplace parameter
u_x, u_y	Displacements
$\sigma_x, \sigma_y, \tau_{xy}$	stresses
$\varepsilon_x, \varepsilon_y, \gamma_{xy}$	Strains
$\mathbf{T}$	Transform matrix
N_i	Shape functions
$\mathbf{J}$	Jocabian matrix
β_{ij}	Elastic compliance
ν	Poisson's Ratio
Ω, Γ	Physical domain and boundary
t_x, t_y	tractions
$K_{\mathrm{I}}, K_{\mathrm{II}}$	Stress intensity factor for mode I and mode II
ρ	Density
c	Velocity
q_i	Specific flux
κ	Permeability
$\tilde{\sigma}_x, \tilde{\sigma}_y, \tilde{\tau}_{xy}$	Stresses in Laplace domain
$\tilde{u}_x, \tilde{u}_y,$	Displacement along the *x* and *y* coordinate
K^*, G^*	Normalized bulk modulus and shear modulus

φ	Friction of volume
κ^*	Normalized permeability
s^*	Normalized Laplace parameter
p^*	Normalized pressure
R^*	Normalized Biot's coefficient parameter

Chapter 1

Introduction

1.1 Background and Motivation

As technology develops in the twenty first century, the urgent need to solve complex engineering problems while maintaining a high level of safety and efficiency has led to the urgent demand for comprehensive study of material performance. In some cases, this has led to the creation of new materials for better design applications and adaptability. Therefore, the study of material science is significant for modern engineering.

Recently, material science has seen a rapid improvement because of the increased cooperation between the different engineering disciplines. Through research, the discovery of new methods and experimental technology has also contributed to the development of material science. Advances in the field of material science have led to the invention of Functionally Graded Materials (FGMs).

Functionally Graded Materials (FGMs) has attracted the attention of various scholars and engineers around the world. This is due to specific positive properties of FGM. Originally, FGMs aimed to satisfy the high-performance requirements for aerospace applications. This includes the material capability to withstand high speed and temperature which is required for designing a modern supersonic aircraft. To achieve this, any proposed material must endure flight speed of approximate 900km/h and a surface temperature as high as 2000℃. In solving this problem, a new concept of

combining irreconcilable properties in the same composite has been proposed [1]. Apart from isotropic materials and composite materials, FGMs can be designed with several materials of different properties, by continuously varying the structure and composite of these materials, resulting in corresponding changes via the geometry[2]. Hence, FGM possesses these material advantages. For example, unlike homogeneous materials, this FGM can behave like a ceramic material with high temperature and chemical resistivity on one side, while on the other side of the FGM material it may perform as a metal with high mechanical strength and toughness [3]. In most cases, cracks can initiate from the sharp interface of the traditional composite material. However, FGMs utilize a gradient interface along the thickness, thus, a smooth transition of the FGM material property is observed from one side of FGM materials to the other side. This is a strong feature which can be an option to resolve practical problems in the future.

Large research investigations have been aimed at mechanical behaviors of FGMs, which is critical for a wide variety of problems in engineering applications. Experimental technology and theoretical analysis have both been applied to evaluate the mechanical properties of FGMs. In the study of mechanical properties of FGMs, it is undoubtedly clear that the result by experimental testing is more accurate and convincing than by numerical analysis. However, mechanical testing would lead to a new challenge for FGMs. This includes the expense of designing and manufacturing FGM specimens. In addition, the engineer must consider the difficulty of experimental setup and the collation of data. When working with FGMs in a controlled environment, the behavior of the complex microstructure can also be difficult to predict. Now, considering the challenges outline above, it is therefore reasonable to perform assessment of FGMs by numerical means. Numerical analyses have gradually become

the best approach to resolve some of the problems outlined as the development of computer processing power continues to grow.

1.2 Numerical Analysis

Generally, the natural behavior of all physical processes, whether mechanic, electric, biologic or geologic, can be described using algebra, differential or integral equations. However, the complexity of most engineering problems makes it unfortunately difficult for researchers to obtain the exact solutions for these problems. Therefore, an approximation technique has been employed to deal with different types of practical problems for engineers and scientist alike. These methods are used to transform the complex practical issues into simple discrete forms under appropriate mathematical descriptions, and then with computer assistance, recreate and solve the problems. Using the analytical data, the description of this phenomena can be observed virtually. Under a proper approximation, the solution error, compared to the analytical one, can be less than 1%, which is evidently acceptable for engineering applications. Furthermore, the assistant of a computer makes it possible to work out thousands of algebraic equations created by suitable approximation in seconds. In contrast to expensive experimental processes, the expense for the numerical analysis is only the computer. That is also one of the reasons why more engineers and scientists have been attracted by the computational numerical techniques to solve practical problems. If an effective numerical method has been applied, there is always a possibility to obtain an approximate solution for a practical problem.

In solving numerical problems, most analyst follow similar procedures as outlined below and this will often lead to acceptable result. The necessary steps are shown below:

1. Under a proper simplification and acceptable assumption, mathematical models have been established.
2. Boundary conditions and initial conditions are used to complete the mathematical models, which are generally described by the governing equations. These governing equations usually consist of ordinary differential equations (ODE), partial differential equations (PDE), or integral equations.
3. Obviously proper numerical techniques are needed to solve the governing equations and then produce computer code to perform the numerical simulation.
4. Finally, the results can be visualized and observed.

In this prescribed procedure, a brief idea about the numerical simulation has been proposed. In order to obtain a reasonable result, a reliable and efficient numerical technique is essential. Up to now, the accuracy and convergence of vast numerical methods have been verified by researchers, using existing numerical methods such as Finite Differential Method (FDM), Finite Element Method (FEM), Finite volume Method (FVM) and Meshless or Meshfree Method. Several of these methods will be discussed in detail later in Chapter 2.

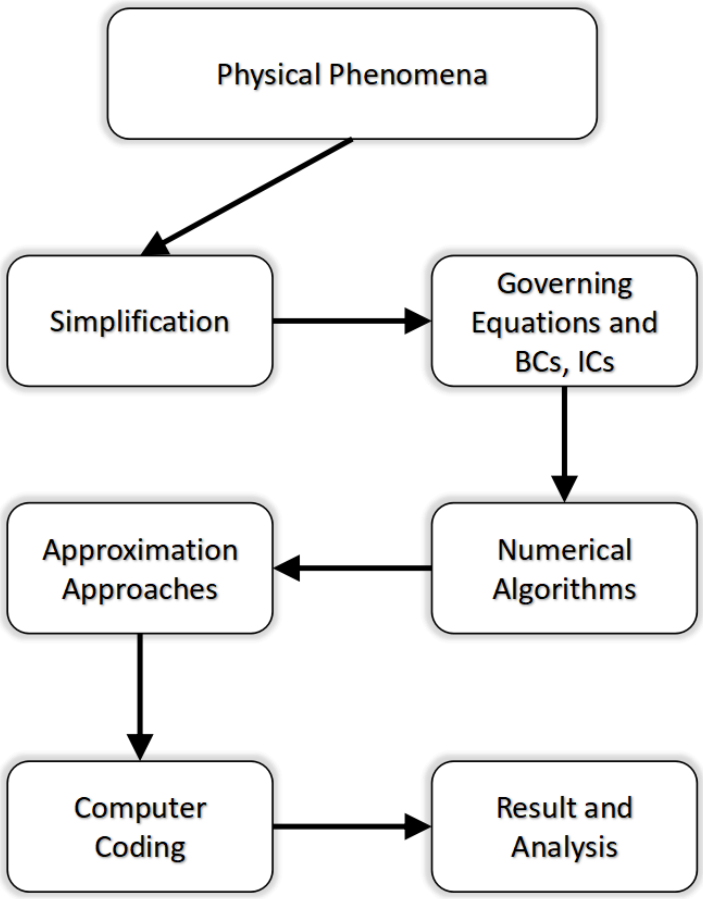

Figure 1.1 Procedure of conducting a numerical simulation.

1.3 Fracture Mechanics

In the study of mechanical behaviors, fracture mechanics plays an important role in understanding the performance of the materials. During the process of manufacturing, inevitably, the presence of crack, which greatly affected the mechanical property, become a critical factor in evaluation of all types of materials. Cracks exist to some extent in all structures. This is probably due to fabrication defects or localized damage in service and this may grow to critical levels.

Crack propagation can result in a weakness of mechanical strength. Therefore, when the residual strength of materials fails to withstand the applied stress, crack grows and may cause the failure of the structure.

Fracture is an issue that engineers have been concerned with for centuries since the origin of man-made structures. This problem has become worse in recent years due to the rapid development in modern technology, such as the invention of airplanes and high-rise buildings. If catastrophic failures occur in such facilities, it is not only detrimental to the economy, but also may lead to loss of lives. In 1983, a report estimated that the annual cost of fracture failures in the U.S. in 1987 amounted to $119 billion dollars [4]. Also, on the 28th of January 1986, the Challenger Space Shuttle broke apart 73 seconds into its flight. This was because an O-ring seal in the right solid rocket booster failed to respond well under low temperature. Before the launch of the shuttle, a group of engineers at the rocket booster facility suspected a potential problem of the O-ring seals. Unfortunately, there were insufficient data to persuade their managers to stop the launch. Seven crew members lost their lives in the end. Until now, The Challenger disaster is still a case study on the topics of engineering safety and workplace ethics. Therefore, numerous researches have been devoted to the understanding of how materials fail and the ability to avoid such failures.

Fortunately, with the assistance of advances in the field of fracture mechanics, it is possible for engineers to predict and offset the potential dangers, thus to prevent structure failures. As the case of the Challenger disaster discussed above, if engineers succeeded in simulating the problem and reported it properly, maybe that tragic event could have been prevented. It is imponderable the number of lives that have been saved or how many property damages have been avoided by applying the theory of fracture mechanics. However, there is no doubt that, in the last few decades, with the knowledge

of fracture mechanics, engineers have protected a vast number of structures from failure.

There are three critical variables in the assessment of fractures. These include the property of the material and the applied stress, as well as flaw size. Over the last several decades, researchers have already developed a great number of ways to characterize the initiation and propagation of crack. Theoretically, these approaches can be classified into two alternative methods: the energy criterion and the stress intensity factors.

As the development of computer processing capability continues, the numerical analysis approach is an important tool to understand the behavior of fracture mechanics. Numerical analysis is extensively applied to the study of fracture mechanics to gain a comprehensive understanding of the initiation and propagation of cracks, also to prove the theoretical failure prediction with real life failures. Furthermore, by employing a proper numerical method, a complicated structure can be simplified. It is uncomplicated for engineers to change the analysis parameters, including the geometry of the model, material property, and the size of the crack. Unlike experimental studies, repeated analysis can be achieved without the process of structure design and manufacture, material selection and physically varying the boundary conditions. This is comparatively a time-saving and high-proficient approach to performing fracture analysis.

In terms of fracture mechanics for FGMs, that was first proposed by Erdogan in 1995, to describe the failure of materials [5]. In 2002, Dolbow et al. proposed an interaction energy integral method to accurately assess mixed-mode stress intensity factors at crack tips of FGMs [6]. Kim and Paulino provided techniques for evaluating mixed-mode stress intensity factors (SIFs), J-integrals, interaction integrals, *T*-stress, and crack initiation angles under static and quasi-static conditions for both isotropic and

orthotropic materials [7, 8]. Wen and Li [9] proposed a new method and successfully applied this to fracture mechanics of functionally graded materials.

1.4 Research Objectives

Finite Element Method has been widely accepted as the preferred numerical method for various engineering analysis, including fracture mechanics. In term of most solids and structures, the accuracy and convergence of FEM have been approved in thousands of cases. ABAQUS, a well-developed commercial software based on FEM, has also contributed to the prevalent of this method when dealing with engineering issues. However, this is a mesh-based method. The results are highly affected by the quality of the meshes or elements. Considering a problem with complex structure, the number of elements used can be extremely large to satisfy the requirement of the accuracy. And FEM is not guaranteed to work when poor meshes or distorted meshes are created. This drives the researchers searching for further advance numerical methods.

In 2013, the Finite Block Method (FBM), based on the Lagrange interpolation method has been first proposed by Wen and Li [10] to solve the heat conduction problem in the functionally graded media and anisotropic materials. This is a mesh reduced method which is based on a first order differential matrix derived from Lagrange interpolation method.

In this thesis, this method will be continually applied to solve the following problems:

1. To evaluate the stress intensity factor and *T*-stress for FGMs-Statics. The stress intensity factor and *T*-stress can be determined by the Finite Block Method for crack problems on both isotropic and anisotropic FGMs. The governing equations for elastic

materials can be transferred to a set of algebraic functions by the aid of Finite Block Method. Besides, a complex problem domain can be separated into several blocks and every block is related to its neighbor block by sharing a line for 2D problems or a face for 3D problems. The crack opening displacement is utilized for the calculation of the stress intensity factor. In addition, a singular core is applied to obtain the *T*-stress by the assistance of William's series.

2. To determine the stress intensity factor and *T*-stress for FGMs-Dynamics; For dynamic analysis, similar as static ones, the Finite Block Method is applied for the space related variables in the setup of system functions (a group of differential equations). Moreover, the Laplace transform parameters are used for the time dependent variables. The solutions are compared with the analytical ones or other methods to verify the accuracy and convergence of Finite Block Method. In the end, a wave propagation in the solid FGMs can be observed in the figures of the results.

3. To explain wave propagation in Poroelastic Materials. The governing equations for the dynamic analysis of porous materials is established with the Biot's theory. Compare to the dynamic analysis of the solid FGMs, a term influenced by the pressure of porous is added into the system equations. Besides, the boundary conditions are also affected by the pressure and fluid convection. The Finite Block Method and the Laplace transform parameters are still applied for the calculation of space and time dependent variables, respectively. The solutions are compared with the analytical solutions for a 1D case. Two different materials are introduced in the examples.

The accuracy of the stress intensity factor, the *T*-stress and the wave propagation as determined by the Finite Block Method will be verified by FEM (ABAQUS) and published papers. This is a reliable way to confirm the validity of the FBM.

1.5 Scope of the Present Thesis

Remaining chapters of this thesis are outlined as follows:

Chapter 2 starts with an overview of fracture mechanics. Three types of crack models are introduced in this chapter. After that, the analysis methods of fracture mechanics are reviewed. Besides, a summary of FEM and Meshless Method has been proposed.

Chapter 3 introduces the FBM, including the basic function of Lagrange Interpolation Method. One-dimension differential matrix, two-dimension differential matrix and mapping technology are systemically discussed in this chapter. In the end, the order of accuracy which relies on the number of nodes is illustrated with a simple case.

Chapter 4 presents the application of FBM for FGMs under static analysis. In this chapter, the formulation of FBM for FGMs is introduced in detail. In addition, Williams series is utilized to describe the stress field at the crack tip to formulate the system equations together with FBM for the evaluation of *T*-stress. Several numerical examples are carried out by both FBM and ABAQUS simulation. Great agreement has been shown by the comparisons between results when a proper number of nodes selected.

Chapter 5 covers the dynamic analysis of FGMs by FBM. In addition, a combination of *T*-stress and FBM is introduced for dynamic analysis. The Laplace transform parameter has been applied to assist the analysis of dynamic problems for FGMs. Isotropic materials and orthotropic materials are both discussed in examples. A singular core has been applied to characterize the stress distribution around the crack tip. Finally, numerical examples are reported.

Chapter 6 explores the influence of wave propagation in Poroelastic Materials. The formulation of Poroelastic Materials relies on Biot's effective stress coefficient is set up with FBM. The process of nondimensionalization is thoroughly presented. The accuracy of the numerical solutions can be verified by comparing with analytical result and published papers.

Chapter 7 summarizes this thesis with key findings and contributions. The future work to improve this method and the applications is suggested.

Chapter 2

Literature Review

2.1 Fracture Mechanics

In the study of material science, fracture mechanics is a field for investigating the discipline of crack propagation in material and engineering structures. It contains two alternative methods to evaluate the resistance behavior of materials under certain conditions, one is numerical analysis and the other is experimental testing. By considering the physical properties of materials, with the elastic and plastic theories proposed in published papers and references, engineers can predict the failure of macro-structures based on the micro-crystallographic defects detected by Non-Destructive Testing (NDT), including ultrasonic and x-ray.

The prediction of crack growth is an important discipline in the study of fracture mechanics and the three-generic displacement modes to enable a crack to propagate are:

1) **Mode I fracture** – Opening mode (a tensile stress normal to the plane of the crack), which is the most common fracture mode in engineering problems and utilized in the experiment of material toughness tests,

2) **Mode II fracture** – Sliding mode (a shear stress acting parallel to the plane of the crack and perpendicular to the crack front), and

3) **Mode III fracture** – Tearing mode (a shear stress acting parallel to the plane of the crack and parallel to the crack front).

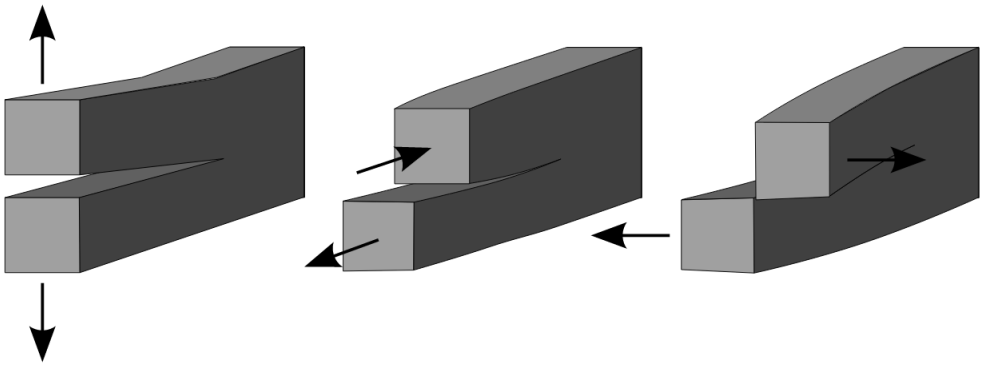

Figure 2.1 Three displacement modes in fracture mechanics [11].

Several centuries earlier, experiments carried out by Leonardo da Vinci confirmed that the strength of the wire, was inversely proportional to the length of the wire. Therefore, it was implicated that the strength of the material was affected by the flaws in the material, the longer the wire, the higher the possibility the material contains a flaw. His experiments suggested the first clue to the main cause of fracture. In 1920, Griffith [12] successfully predicted that the strength of the materials was related to the flaw size. He applied a stress to an elliptical hole up to the unstable propagation limits of the crack. And the results showed that the maximum tensile stress around the crack tip is more than ten times as great as the tensile strength of the material. In this concept, when crack length increases, the strain-energy produced is just sufficient to overcome resistance to crack growth from the surface energy of the material. At this point, crack

propagation will occur. However, Griffith's work has been validated only for ideal brittle materials. In 1939, Westergaard [13] presented a numerical method to analyze the stress and displacement distribution around the crack tip. In 1956, George Irwin [14], the leader of a group research on fracture mechanics at Naval Research Laboratory (NRL) in the U.S.A proposed the principle of energy release rate, which was an extension of Griffith theory, but more powerful to solve engineering problems. One year later, Irwin [15] utilized Westergaard's method to illustrate that the stress and displacement around the crack tip can be characterized by a single constant, and also he determined a relation between this constant and the energy release rate. Later, this constant parameter became part of the description for the stress and displacement near the crack tip, and this was termed the stress intensity factor.

Around 1960, when the fundamentals of linear elastic fracture mechanics (LEFM) was well established, the analysis of yielding at the crack tip did attract the attention of many researchers. In 1960-1961, several researchers correctly applied numerical methods to study the displacement at the crack tip, for example, Irwin [16], Dugdale [17], Barenblatt [18]. The plastic zone correction was proposed by Irwin in [16], while Dugdale [17] and Barenblatt [18] defined the plastic zone size. In 1963, Wells [19] sought the distribution of displacement along the crack as an alternative fracture criterion. He noticed that, the crack propagated with a plastic deformation, which led to the development of crack tip opening displacement (CTOD). In 1968, Rice [20] proposed a line integral which was independent of the path surround the crack tip, and this line integral was known as the J-integral method. Later on, several researchers successfully applied the J-integral to fracture mechanics for nonlinear materials, such as

Hutchinson [21], Rice and Rosengren [22], Begley and Landes [23] et al. The J-integral is considered as a fracture criterion as well as the stress intensity factor and the energy release rate.

In the next section, the energy release rate and stress intensity factor will be noted in two ways: the energy approach and the stress intensity approach. The relationship between these two factors for the evaluation of cracks is introduced as well.

2.2 Analysis Methods of Fracture Mechanics

In this section, the emphasis remains on the development of linear elastic fracture mechanics (LEFM), specifically, the characterizing parameters at the crack tip: stress-intensity factor and energy release rate. At the assistance of these two parameters, the major damage tolerance of the materials can be quantified, thus it is possible for engineers to design tools with less material failures under specific circumstance since the 1960s.

2.2.1 Energy Release Rate

The first law of thermodynamics is the law of energy conservation. This law states that the total energy of an isolated system is constant. which can be transformed from one form to another, but neither created nor destroyed. In 1920, Griffith [12] applied this idea to form the Griffith energy balance to describe the process of crack propagation. In order to increase the crack, the potential energy inside the crack area must be greater or at least equal to the surface energy of the materials.

Consider a uniformly stressed infinite plate containing a central crack of length $2a$, as shown in Figure 2.2. The Griffith energy balance can be explicated as follows:

$$\frac{dE}{dA} = \frac{d\Pi}{dA} + \frac{dW_s}{dA} = 0 \tag{2.1a}$$

or

$$-\frac{d\Pi}{dA} = \frac{dW_s}{dA}, \tag{2.1b}$$

where E is the total energy, Π is the potential energy, W_s represents the work required to create a new surface, A is the surface area.

For a plate with central crack shown in Fig 2.2, with the aid of the work by Inglis [24] , the potential energy as a function of stress can be expressed as

$$\Pi = \Pi_0 - \frac{\pi\sigma_0^{\,2}a^2B}{E} \tag{2.2}$$

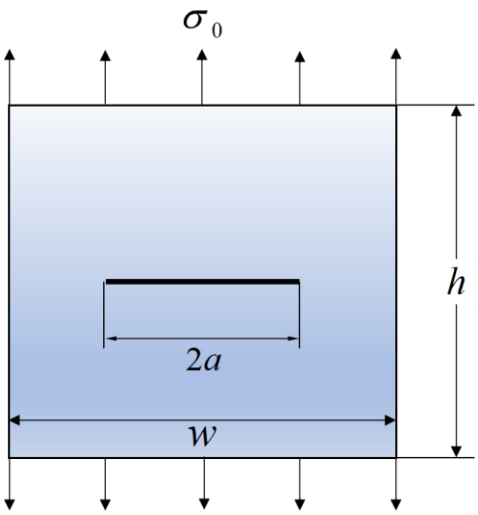

Figure 2.2 A through-thickness crack in an infinitely wide plate subjected to a remote tensile load. $w >> a, h >> a$.

where B indicates the plate thickness. There are two new surfaces created when a crack propagates, thus W_s is given by

$$W_s = 4aB\gamma_s, \tag{2.3}$$

in which γ_s is the surface energy of the material. Therefore

$$-\frac{d\Pi}{dA} = \frac{\pi\sigma_0^2 a}{E} \tag{2.4a}$$

and

$$\frac{dW_s}{dA} = 2\gamma_s . \tag{2.4b}$$

Substituting Eq. (2.4a) and Eq. (2.4b) into Eq. (2.1b), one obtains

$$\sigma_f = (\frac{2E\gamma_s}{\pi a})^{1/2}, \tag{2.5}$$

here σ_f denotes the critical stress used to create the crack, also known as the fracture stress. In 1956, Irwin [14] proposed a new parameter called the energy release rate G to evaluate the energy required for crack propagation:

$$G = -\frac{d\Pi}{dA}, \tag{2.6}$$

The term G is the negative derivative of potential energy with respect to crack area only. From Eq. (2.4a), the parameter G for an infinite plate with a central crack as shown in Figure 2.2 is given by

$$G = \frac{\pi\sigma_0^2 a}{E}. \tag{2.7}$$

When the energy release rate $G \geq G_c$, the crack extension occurs. Hence, G_c is the critical energy release rate, a parameter used for measuring the fracture toughness of a material. The critical energy release rate G_c is defined as a constant parameter only

related to the property of the materials, and it is independent of the applied force and the geometry of the model.

2.2.2 Stress Intensity Factor

In 1960s, Irwin [16] showed that the stress and displacement states in the close neighborhood of a smooth internal boundary of a plane crack in a linearly elastic solid under general loading conditions may be expressed in terms of three stress intensity factors $K_{\mathrm{I}}, K_{\mathrm{II}}$ and K_{III} associated with the symmetric opening, in-plane or forward shear, and anti-plane shear modes of deformation, respectively (Figure 2.1).

Assume a polar coordinate system with the origin at the crack tip shown in Figure 2.3, the stress distribution in any linear cracked body can be described by

$$\sigma_{ij} = (\frac{k}{\sqrt{r}}) f_{ij}(\theta) + \sum_{m=0}^{\infty} A_m r^{m/2} g_{ij}^{(m)}(\theta), \tag{2.8}$$

where σ_{ij} represents the stress tensor, r and θ are defined in Figure 2.3, k is constant parameter, f_{ij} denotes the dimensionless function of θ in the first term at the right side of Eq. (2.8), $g_{ij}^{(m)}$ is the dimensionless function of θ for the m^{th} term, A_m is a series of unknown coefficients.

It is apparent that when $r \to 0$, as the first term on the right-hand side of Eq. (2.8) approaches infinity, the other terms can be eliminated.

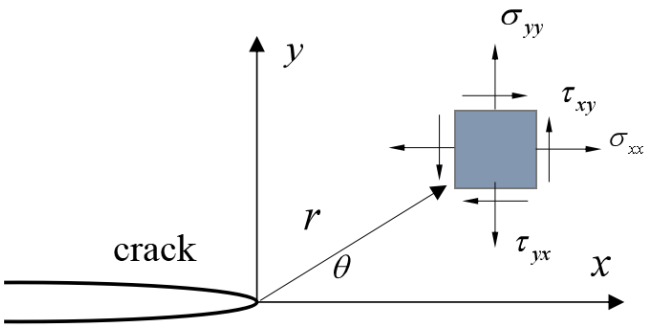

Figure 2.3 Definition of the coordinate axis in front of the crack tip.

There are three types of modes that a crack can extend, as shown in Figure 2.1. For this thesis, only mode I and mode II are considered. The expressions describing the stress and displacement distribution for mode I and mode II are shown in Table 2.1 and Table 2.2, respectively.

Table 2.1 Stress distribution near the crack tip for Mode I and Mode II in linear elastic, isotropic materials.

	Mode I	Mode II
σ_x	$\frac{K_{\mathrm{I}}}{\sqrt{2\pi r}}\cos(\frac{\theta}{2})[1-\sin(\frac{\theta}{2})\sin(\frac{3\theta}{2})]$	$\frac{K_{\mathrm{II}}}{\sqrt{2\pi r}}\sin(\frac{\theta}{2})[2+\cos(\frac{\theta}{2})\cos(\frac{3\theta}{2})]$
σ_y	$\frac{K_{\mathrm{I}}}{\sqrt{2\pi r}}\cos(\frac{\theta}{2})[1+\sin(\frac{\theta}{2})\sin(\frac{3\theta}{2})]$	$\frac{K_{\mathrm{II}}}{\sqrt{2\pi r}}\sin(\frac{\theta}{2})\cos(\frac{\theta}{2})\cos(\frac{3\theta}{2})$
τ_{xy}	$\frac{K_{\mathrm{I}}}{\sqrt{2\pi r}}\cos(\frac{\theta}{2})\sin(\frac{\theta}{2})\cos(\frac{3\theta}{2})$	$\frac{K_{\mathrm{II}}}{\sqrt{2\pi r}}\cos(\frac{\theta}{2})[1-\sin(\frac{\theta}{2})\sin(\frac{3\theta}{2})]$

Table 2.2 Crack-tip displacement distribution for Mode I and Mode II in linear elastic, isotropic materials.

	Mode I	Mode II
u_x	$\frac{K_{\mathrm{I}}}{2\mu}\sqrt{\frac{r}{2\pi}}\cos(\frac{\theta}{2})[\kappa-1+2\sin^2(\frac{\theta}{2})]$	$\frac{K_{\mathrm{II}}}{2\mu}\sqrt{\frac{r}{2\pi}}\sin(\frac{\theta}{2})[\kappa+1+2\cos^2(\frac{\theta}{2})]$
u_y	$\frac{K_{\mathrm{I}}}{2\mu}\sqrt{\frac{r}{2\pi}}\sin(\frac{\theta}{2})[\kappa+1-2\cos^2(\frac{\theta}{2})]$	$-\frac{K_{\mathrm{II}}}{2\mu}\sqrt{\frac{r}{2\pi}}\cos(\frac{\theta}{2})[\kappa-1-2\sin^2(\frac{\theta}{2})]$

Consider pure Mode I stress applied on the cracked plate, where $\theta = 0$. According to Table 2.1 and Table 2.2, the stress near the crack tip can be expressed as:

$$\sigma_x = \sigma_y = \frac{K_{\mathrm{I}}}{\sqrt{2\pi r}} \tag{2.9a}$$

and the displacement on the crack surface

$$u_y = \frac{K_{\mathrm{I}}}{2\mu}\sqrt{\frac{r}{2\pi}}(\kappa\text{-}1), \quad u_x = 0, \tag{2.9b}$$

where $\kappa = 3 - 4\nu$ (plane strain) and $\kappa = (3-\nu)/(1+\nu)$ (plane stress), ν is Poisson's ratio, μ is shear modulus.

Note that Eq. (2.9a) and Eq. (2.9b) are only valid when $r/a << 1$. Also, it states that each displacement and stress component is proportional to a constant parameter K_{I} for mode I, and K_{II} for Mode II. If the constant K_{I} and K_{II} are known, the entire displacement and stress distribution around the crack tip can be solved. Conversely, if the displacement or the stress distribution is already known, the stress intensity factor K_{I} can be obtained as well. Eq. (2.9b) can be rewrite as

$$K_{\mathrm{I}} = \frac{\Delta u_y \mu}{\kappa\text{-}1}\sqrt{\frac{2\pi}{r}}, \tag{2.10}$$

where Δu_y is also known as the Crack Opening Displacement (COD), and Eq. (2.10) can be used to solve stress intensity factor in Linear Elastic materials by COD method. Due to the importance of the stress intensity factors on the evaluation of fracture characteristics of a material, some accurate values of stress intensity factors for standard specimens have been recorded in handbooks or on computer database. In practice, engineers are faced with much complicated configurations and loads. So that, the results

given in handbooks and computer databases are not sufficient and therefore a full scale computational analysis is often necessary.

In this thesis, Crack Opening Displacement method is applied to calculate the stress intensity factors for the evaluation of crack problems on both isotropic and orthotropic materials. The Equations of stress intensity factors for orthotropic materials will be discussed later in chapter 4.

2.3 Finite Element Method

Finite element method, with the revolution of computers, has attracted the attention of most engineers and scientists in solving the problems in engineering fields numerically. In the early fifties, FEM was first used in the field of linear structural analysis, such as aircraft static structure and dynamic characteristics analysis in order to obtain the deformation of the structure, stresses, natural frequencies and vibration modes. Because of the validity of this method, the application of FEM has been extended from the linear problems to nonlinear problems, and from elastic material to plastic, visco-elastic, visco-plastic and composite materials.

At the beginning, the idea of FEM is to separate a large structure into finite small areas called elements. The individual elements are connected by a topological map called a mesh. To be specific, the elements are linked-up to each other by means of the nodes. The deformation and stress can be described by a simple interpolation function. In the solution process, only the stress and deformation in the junction need to be calculated. The stress and deformation in the non-junction area can be obtained by interpolation functions, in other words, the finite element method does not solve deformation or stress of any point within the area.

In fact, if the divided area is sufficiently small, the results for the deformation and stress in each area can be very close to the real situation. It can be proved in theory that when a sufficient number of elements exist, the solution of the finite element will converge to an exact solution. However, as the number of elements increases, the steps for computation increase as well. For this reason, the actual work is always to find the balance between computation and accuracy.

While it is difficult to quote an exact date for the invention of FEM, its development can be traced back to Ritz [25] in 1909 who developed an effective method for the approximate solution of problems in the mechanics of deformable solids. In 1943, Courant [26] considerably introduced a particular linear function over triangular regions to increase the feasibility of Ritz's method, and applied the method to solve torsion problems. The term "finite element" was first introduced in [27] by Clough in 1960, who successfully applied this method to plane stress analysis. Since then, the FEM achieved its real pick time in the 1960s and 1970s by the contributions of J. H. Argyris [28], Turner [29], Hrennikov [30] and et al. The first book for the FEM was written by Zienkiewicz and Chung [31] in 1967, to introduce the basic method of finite element method and solve several engineering problems. Due to the ability to handle very complex geometry, the FEM method has been used in a wide range of engineering problems, such as solid mechanics, dynamics, heat problems, fluids and electrostatic problems et al. Several commercial software (ABAQUS, ANSYS et al) are based on FEM originated in the 1970s. In this thesis, the result by ABAQUS is considered as benchmark, to compare with the result by numerical approach for a confirmation of accuracy.

After plenty of applications in engineering practices and more than half a century of development, FEM has been proved to be an effective method for the simulation of engineering problems. Thus, FEM has played a significant role in the progress of industrial technology. On the other hand, FEM has the inherent shortcomings of numerical methods which rely on meshes or elements that are connected by nodes in a predefined manner. When analyzing challenging problems where the materials can move around (computational fluid dynamics) or solid structures with areas of large deformation, it is difficult to generate the meshes without introducing some level of error. Thus, there is an urgent demand for a new concept of approximation methods.

In other words, to ensure equality between finite element boundaries and the moving discontinuities, fine mesh is required in the FEM. In the meantime, finer meshes indicate an extra cost of computing time and program effort. Therefore, the concept of mesh free methods has been proposed, in which elements are eliminated or reduced.

2.4 Meshless Method

The Meshfree or Meshless method, abbreviated MFree method, is used to transfer a series of differential equations or integral equations to a series of algebraic equations for the entire model without the creation of meshes and elements. Consequently, the equilibrium conditions and the boundary conditions are no longer applied to meshes but rather to the exact nodes. Without the formation of meshes, these nodes are related to each other by the interpolation methods. MFree method has a great advantage in solving difficult problems without the elements, such as crack propagation, large deformation et

al. In this section, several applications and development of Meshless Methods are introduced briefly.

The advent of MFree method can be traced to 1977, with Monaghan and Gingold [32] and Lucy [33] developing a Lagrangian method based on the Kernel Estimates method to model astrophysics problems, which is well-known as Smooth Partial Hydrodynamics (SPH). However, due to the powerful computational mechanics analysis of FEM and FDM, not until 1990s, with the rapid development of the computer, the MFree method continually appeared in literature. In 1988, Monaghan [34] presented the derivation of the equations for SPH (smoothed particle hydrodynamics) and describes their application to a wide variety of problems in compressible gas flow. In 1992, Monaghan [35] proposed the SPH method to calculate free surface incompressible flows. The results of the simulation can prove that it is an optimized method for the generation of boundary conditions. Besides, In 2009, a Lagrangian corrected SPH method was introduced by Chen [36] for the simulation of connected conditions on the interface of the particulate composites. Furthermore, Shao [37] improved this SPH method for the simulation of liquid sloshing dynamics. The Reynolds Averaged turbulence model was presented with the SPH method to perform the turbulence effects. A development of the accuracy was made by the adoption of a coupled dynamic solid boundary treatment (SBT) algorithm to deal with the boundary areas on the solid part.

In 1992, Nayroles etc. proposed the Diffuse Element Method [38] which based on the shape function of moving least square (MLS). Compared with FEM, the advantages of this method, is the generation of shape functions can be simply applied to the given nodes, so that their derivatives can be successfully estimated. Many authors stated that it

was that after the Diffuse Element Method (DEM) the MFree Method attracted the interest of the engineers and scientists. In 2004, Breitkopf [39] improved this method with a quadrature scheme, so called as Hermite MLS shape functions, for the calculation of the drilling problems.

In 1994, Belytschko [40] and his colleagues stated the Element-Free Galerkin Method (EFG), which was as an extended version of Nayroles' method based on the moving least square (MLS). Compared by DEM, EFG is advanced in accuracy although its computational steps increase.

The invention of Reproducing Kernel Particle Method (RKPM) was very close to the EFG method by Liu [41], in order to systematically correct the lack of consistency in the SPH method. The RKPM has been successfully used in multi-scale techniques [42], acoustics analysis [43], fluid dynamics [44] and many other applications.

During this period, Finite Point Method has been proposed by Onate and colleagues in 1996 [45]. It was only used for the problems of dynamic fluid at the beginning, and later applied to simulate other mechanics problems, such as elasticity and plate bending. Combination of Collocation Point Technique and any of the following approximation techniques, such as Least Square Approximation, Weighted Least Square Approximation or Moving Least Squares, is the basic idea of this method.

In 1998, Atluri and Zhu [46] presented a new path to achieve MFree method, named the Meshless Local Petro-Galerkin method (MLPG), which might be a big step in understanding the MFree Method. This method implements the numerical integration in MFree sense, and its basic idea is the Local weak form without the existence of the background cell. In order to simplify the integrand of the weak form, the Petrov-Galerkin method is used in the MLPG. Originally, this method was used the

MLS technique and later Atluri extended the MLPG method to other MFree approximation techniques. The freedom of choice for the test function in the Petrov-Galerkin method gives rise to different MLPG schemes [47].

Another significant invention of MFree method was Radial Basis Functions (RBF) which was first introduced by Kansa [48] in 1991, when a technique built on the direct Collocation method and the Multiquadric RBF was applied to simulate fluid dynamics. Comparatively, it is simple to perform with the direct Collocation procedure by Kansa, although because of the mix of governing equations and boundary conditions it results in an asymmetric system of equations. Additionally, the existence of Multiquadric RBF results in global approximation, which leads to a system of equations that is characterized by a dense stiffness matrix. Lee and his colleagues [49] stated a local multiquadric approximation for solving boundary value problems in 2003, which avoid the global approximation and result in a sparse stiffness matrix. In the last decade, the RBF approximation technique has gone through a rapid development. However, the majority of papers on this topic only concern its mathematical proof and foundations. Until 2003, an introduction of the mathematical background of RBFs is presented in [50]. RBFs has been successfully applied in dealing with some physical problems, such as transport phenomena [51], heat conduction [52], Kirchoff Plates and Euler-Bernoulli beam problems.

Liu and Gu [53] greatly contributed to the approximation of Point Interpolation Method (PIM) based on the Polynomial Interpolation, which is seen as an alternative of the Moving Least Square (MLS). One year later, the definition of MFree Method has been proposed by GR Liu in [54]. At first, the singularity of the interpolation matrix and the uncertain continuity of the approximation function by the PIM, based on the

Galerkin method, has been an obstruction. Several approaches have been investigated by Liu in order to solve these questions [55]. Improvements have been obtained using the Local Petrov-Galerkin method and Multiquadric radial basis functions. This procedure resulted in Local Radial Point Interpolation methods (LRPIM). The LRPIM has been applied to solid mechanics, fluid flow problems and others. These applications are referred to and examined in detail in [56].

2.5 Summery

In this section, the importance of the fracture mechanics has been discussed. Besides, the basic strategy to evaluate the fractures including the energy release rate and stress intensity factors is discussed. Several applications for the determine of the stress intensity factors for the fracture problems have been presented with numerical analysis.

In addition, the FEM and its applications is presented above. This method has been approved to be an optimized method for most physical problems with suitable mesh generation. Several commercial softwares (FEM, ANSYS, et al), based on the FEM, are admitted by plenty of the engineers and scholars.

Furthermore, the historical improvement and relatively applications of MFree methods have been discussed previously, including SPH, MLPG, RBF and many others. A new MeshFree method, which is known as Finite Block Method (FBM), first proposed by Wen will be discussed comprehensively in chapter 3.

Chapter 3

Finite Block Method

3.1 Introduction

Finite Block Method (FBM), based on the one-dimensional differential matrix derived from the Lagrange interpolation, was first proposed by Li and Wen [10] to solve transient heat conduction problems of both isotropic and orthotropic materials. In addition, the FBM was applied on static elasticity problems for functionally graded materials in 2014 by Wen [9]. In 2015, the FBM was developed to solve the problems on frictional contact analysis with strong form by Li and Wen [57]. Besides, combined with Local Petrov-Galerkin method (LPGM), the Finite Block Petrov-Galerkin method (FBPG) was presented to transfer the partial differential equations in a weak form to a series of algebraic equations with two-dimensional Lagrange series by Li and Wen [58]. In 2016, combined with William's series of stress function in a singular core, the FBM was employed to study interface crack in bi-materials by Wen [59]. In 2017, Li and Wen [60] proposed the use of FBPGM subjected to Reissner plate for the analysis of nonlinear and post buckling problems.

In this chapter, the basic strategy of FBM which is the Lagrangian interpolation method will be discussed. Additionally, the coefficient differential matrix can be determined by a normalized local domain, such as a square for 2D problems and a cubic for 3D problems. By introducing the mapping technique, a complex real domain can be

divided into several blocks, and each block is allowed to transform from Cartesian coordinate (xyz) to normalized coordinate $(\xi\eta\varsigma)$ with 8 seeds for two dimensions and 20 seeds for three dimensions. With the aid of coefficient differential matrix, the differential equation is possible to convert to a series of algebraic functions. In the end, compared with analytical solutions, several examples will be illustrated to confirm the convergence and accuracy of the FBM.

3.2 Lagrange Interpolation Method

3.2.1 Introduction

In the discipline of mathematical analysis, interpolation is the method of approximating an unknown function at a point in a domain by using a range of discrete set of known data points neighboring it or around it. In engineer projects, people always utilize a list of data points, attained by experimental test, which perform as a solution of an equation for a limited number of values. In this case, it is often necessary for engineers to explicit that function for an intermediate value by interpolation method.

There are several interpolation methods, including Piecewise Constant Interpolation Method, Linear Interpolation Method and Polynomial Interpolation Method. As expressed in the paragraph above, for FBM, Lagrange interpolation method, which is a type of Polynomial Interpolation Method is introduced.

In this chapter, the basic function of Lagrange Interpolation Method will be discussed in details and one-dimensional differential matrix, as well as two-dimensional differential matrix will be introduced.

3.2.2 Lagrange Interpolation Method

In numerical analysis, Lagrange polynomials are used for polynomial interpolation. Consider a number of discrete points, the Lagrange polynomial is the polynomial of lowest degree that assumes at each point the corresponding value (i.e. the functions coincide at each point).

Although named after Joseph Louis Lagrange, who published the Lagrange Interpolation Method in 1795, the method was first proposed in 1779 by Edward Waring. Consequently, it is also a formulation rediscovered by Leonhard Euler. In 1988, Jeffreys H. and Jeffreys B.S. introduced this method comprehensively in [61].

Consider a set of nodes: $(\xi_1, u_1), (\xi_2, u_2), ...(\xi_k, u_k)$, where no two $\xi_j \ (j = 1, 2, ..., k)$ are the same, the interpolation polynomial in the Lagrange form is a linear combination of Lagrange basis polynomials as:

$$u(\xi) = \sum_{j=1}^{N} u_j \varphi_j(\xi), \tag{3.1}$$

where

$$\varphi_j(\xi) = \prod_{\substack{k=1 \\ k \neq j}}^{N} \frac{(\xi - \xi_k)}{(\xi_j - \xi_k)}, \tag{3.2}$$

Note that, $\varphi_j(\xi) = 1,$ when $\xi = \xi_j$, and for all other nodes, $\varphi_j(\xi) = 0.$ Therefore, it exactly satisfies $u(\xi_j) = u_j$ at each collocation point. The function in Eq. (3.2) is also defined as a shape function in the Lagrangian interpolation method.

3.2.3 One-Dimensional Differential Matrix

As the section mentioned above, consider a set of nodes for one dimensional problems. The first order differential matrix $\mathbf{D}_0$ can be evaluated by the use of Lagrange series of interpolation. The function $u(\xi)$ is approximated as Eq. (3.1), then the first order derivative is determined by

$$\frac{du}{d\xi}=\sum_{j=1}^{N}u_j\prod_{k=1,k\neq j}^{N}(\xi_j-\xi_k)^{-1}\sum_{i=1}^{N}\prod_{k=1,k\neq j,k\neq i}^{N}(\xi-\xi_k). \tag{3.3}$$

Then the nodal value of derivative of function $u(\xi)$ can be written in matrix form as

$$\mathbf{U}_{\xi}=\mathbf{D}_0\mathbf{u}, \tag{3.4}$$

where $\mathbf{U}_{\xi}=[u_1^{'},u_2^{'},...,u_N^{'}]^T$, $u'=du/d\xi$ is a vector of nodal value of first order derivative with respect to coordinate ξ, $\mathbf{u}=[u_1,u_2,...,u_N]^T$. For the second order derivatives at each node, we have approximately

$$\mathbf{U}_{\xi}^{(2)}=\mathbf{D}_0\mathbf{U}_{\xi}=\mathbf{D}_0^2\mathbf{u}, \tag{3.5}$$

in which $\mathbf{U}_{\xi}^{(2)}=[u_1^{''},u_2^{''},...,u_N^{''}]^T$, $u''=d^2u/d\xi^2$ is a vector of nodal value of the second order derivative. Simply, by pre-multiplying the first order differential matrix $\mathbf{D}_0$ to Eq (3.5) the higher order differential matrix can be obtained straightaway.

As for a regular node distribution, $\xi_i=-1+2(i-1)/(N-1)$, $i=1,2,...,N$, as shown in Figure 3.1, the coefficient of first order differential matrix $\mathbf{D}_0$ can be determined as follows ($N\leq 6$):

$$\mathbf{D}_0=\frac{1}{2}\begin{pmatrix}-3 & 4 & -1\\ -1 & 0 & 1\\ 1 & -4 & 3\end{pmatrix}_{3\times 3},$$

$$\mathbf{D}_0 = \frac{1}{4}\begin{pmatrix} -11 & 18 & -9 & 2 \\ -2 & -3 & 6 & -1 \\ 1 & -6 & 3 & 2 \\ -2 & 9 & -18 & 11 \end{pmatrix}_{4\times 4},$$

$$\mathbf{D}_0 = \frac{1}{6}\begin{pmatrix} -25 & 48 & -36 & 16 & -3 \\ -3 & -10 & 18 & -6 & 1 \\ 1 & -8 & 0 & 8 & -1 \\ -1 & 6 & -18 & 10 & 3 \\ 3 & -16 & 36 & -48 & 25 \end{pmatrix}_{5\times 5},$$

$$\mathbf{D}_0 = \frac{1}{24}\begin{pmatrix} -137 & 300 & -300 & 200 & -75 & 12 \\ -12 & -65 & 120 & -60 & 20 & -3 \\ 3 & -30 & 20 & 60 & -15 & 2 \\ -2 & 15 & -60 & 20 & 30 & -3 \\ 3 & -20 & 60 & -120 & 65 & 12 \\ -12 & 75 & -200 & 300 & -300 & 137 \end{pmatrix}_{6\times 6}.$$

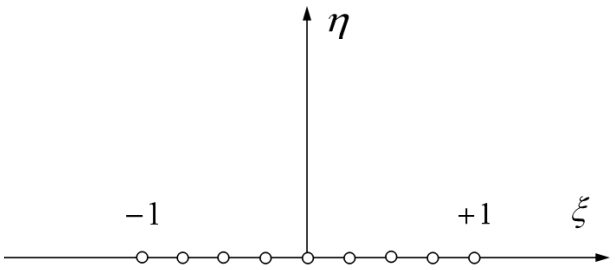

Figure 3.1 One dimensional regular node distribution.

The uniform nodes distribution has been introduced above. However, in most of physical problems, there is a requirement for a concentration of an area such as the boundaries. In this case, the irregular node distribution can be proposed. For example, the Chebyshev nodes distribution, $\xi_i = -\cos((i-1)\pi/(N-1))$, $i = 1,2...,N$ as shown

in Figure 3.2, and consequently, the first order differential matrix of irregular node distribution are as follows ($N \le 6$):

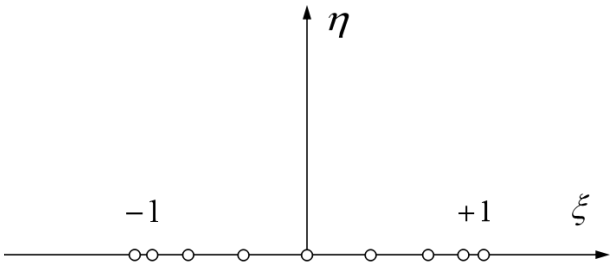

Figure 3.2 One dimensional Chebyshev nodes distribution.

$$\mathbf{D}_0 = \begin{pmatrix} -1.500 & 2.000 & -0.500 \\ -0.500 & 0 & 0.500 \\ 0.500 & -2.000 & 1.500 \end{pmatrix}_{3\times 3},$$

$$\mathbf{D}_0 = \begin{pmatrix} -3.167 & 4.000 & -1.333 & 0.500 \\ -1.000 & 0.333 & 1.000 & -0.333 \\ 0.333 & -1.000 & -0.333 & 1.000 \\ -0.500 & 1.333 & -4.000 & 3.167 \end{pmatrix}_{4\times 4},$$

$$\mathbf{D}_0 = \begin{pmatrix} -5.500 & 6.828 & -2.000 & 1.172 & -0.500 \\ -1.707 & 0.707 & 1.414 & -0.707 & 0.293 \\ 0.500 & -1.414 & 0 & 1.414 & -0.500 \\ -0.293 & 0.707 & -1.414 & -0.707 & 1.707 \\ 0.500 & -1.172 & 2.000 & -6.828 & 5.500 \end{pmatrix}_{5\times 5},$$

$$\mathbf{D}_0 = \begin{pmatrix} -8.500 & 10.472 & -2.894 & 1.528 & -1.106 & 0.500 \\ -2.618 & 1.171 & 2.000 & -0.894 & 0.618 & -0.276 \\ 0.724 & -2.000 & 0.171 & 1.618 & -0.894 & 0.382 \\ -0.382 & 0.894 & -1.618 & -0.171 & 2.000 & -0.724 \\ 0.276 & -0.618 & 0.894 & -2.000 & -1.717 & 2.618 \\ -0.500 & 1.106 & -1.528 & 2.894 & -10.472 & 8.500 \end{pmatrix}_{6\times 6}.$$

It is noticeable that for the matrix $\mathbf{D}_0 = (d_{ij})$ above, it satisfies that $d_{ij} = -d_{N+1-i,N+1-j}$ $(i, j = 1,2,...,N)$ and $\sum_{j=1}^{N} d_{ij} = 0$ $(i = 1,2,...,N)$ for both regular node distribution and irregular node distribution. In addition, the irregular node distribution can be applied to an area near the boundary or at the boundary where high nodal concentration is required. Besides a problem of damping for the solutions was proposed by Runge in 1901 for all Polynomial Interpolation Methods when the number of nodes increased, including the Lagrange Interpolation Method, and this limitation of polynomial interpolation method also known as the Runge's Phenomenon. This shows that in some cases the accuracy of the solution is not improved by using higher order polynomials. However, by applying Chebyshev nodes, this problem is guaranteed to diminish as increasing the order of the polynomials.

3.2.4 Two-Dimensional Differential Matrix

For two dimensional problems, assume a normalized square domain, similar to one dimensional problems, the first order differential matrix at point p can be defined as

$$U_{\xi p}(\xi_p, \eta_p) = \frac{\partial u}{\partial \xi}(\xi_p, \eta_p) \tag{3.6}$$

The total number of point p is $N \times (j-1) + i$ in global numbering system as Figure 3.3, where i is the number of column, j is the number of row. In addition, the first order partial differentials can be expressed in a matrix form

$$\mathbf{U}_{\xi} = \mathbf{D}_{\xi}\mathbf{u}, \tag{3.7}$$

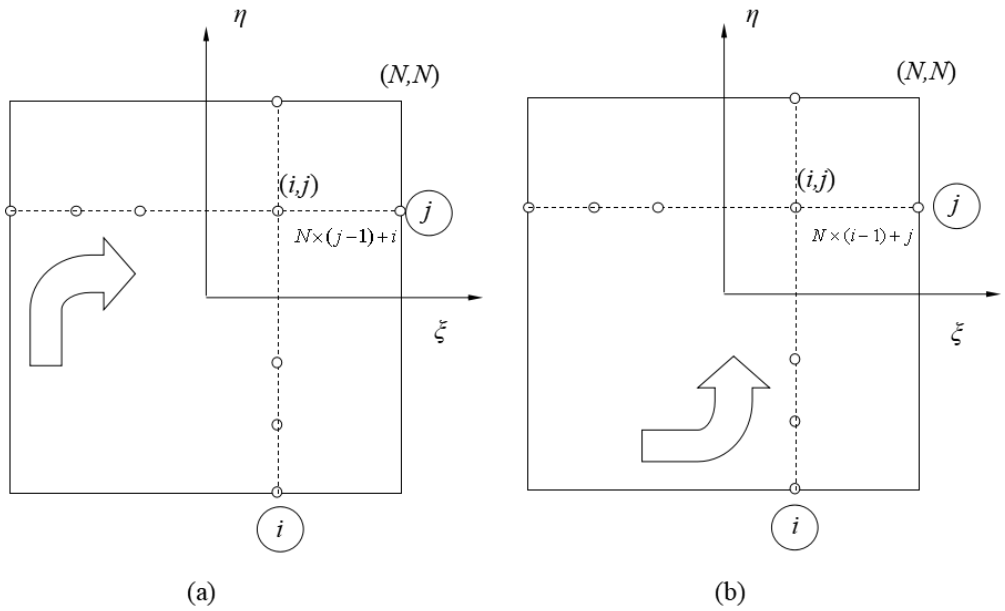

Figure 3.3 Transformation of numbering system: (a) global numbering system, (b) local numbering system.

where the vector of first order differentials $\mathbf{U}_\xi = [U_{\xi 1}, U_{\xi 2}, ..., U_{\xi M}]^T$ and M is the total number of collocation points ($M = N \times N$ from network shown in Figure 3.3). For a square domain in normalized coordinate and numbering system, the first order differential matrix in global numbering system for all nodes is

$$\mathbf{D}_\xi = \underbrace{\begin{pmatrix} \mathbf{D}_0 & 0 & ... & 0 \\ 0 & \mathbf{D}_0 & 0 & 0 \\ ... & ... & ... & ... \\ 0 & 0 & 0 & \mathbf{D}_0 \end{pmatrix}}_{M \times M},$$

in which $\mathbf{D}_0$ is differential matrix obtained for one-dimension problems with the size of $N \times N$. Similarly, the nodal value of the partial differential with respect to axis η is

$$U_{\eta p}(\xi_p, \eta_p) = \frac{\partial u}{\partial \eta}(\xi_p, \eta_p), \tag{3.8}$$

which can be written in the matrix form as in local number system $(p = N \times (i-1) + j)$ as shown in Figure 3.3(b)

$$\overline{\mathbf{U}}_{\eta} = \mathbf{D}_{\xi}\overline{\mathbf{u}}\,, \tag{3.9}$$

in the local system for the collocation points. By using transform matrix, the first order derivative with respect to η in global numbering system can be written as

$$\mathbf{U}_{\eta} = \mathbf{T}\overline{\mathbf{U}}_{\eta}, \quad \mathbf{u} = \mathbf{T}\overline{\mathbf{u}}\,. \tag{3.10}$$

Consider the collocation point $p = N \times (j-1) + i$ in the global number system is the collocation point $p = N \times (i-1) + j$ in local numbering system, therefore in the transform matrix $\mathbf{T}$, all elements are zero except $T_{N\times(j-1)+i,N\times(i-1)+j} = 1, (i, j = 1,2,...,N)$.

Simply rearrange the number of nodes, Equation (3.8) can be rewritten in the global system as

$$\mathbf{U}_{\eta} = \mathbf{T}\mathbf{D}_{\xi}\mathbf{T}^{-1}\mathbf{u} = \mathbf{D}_{\eta}\mathbf{u},\ \mathbf{T}^{-1} = \mathbf{T}^{T}\,. \tag{3.11}$$

Besides, it is not difficult to extend this idea to higher order differentials in 2D dimension with respect to both coordinates ξ and η:

$$U_{\xi\eta}^{(mn)}(\xi_p, \eta_p) = \frac{\partial^{m+n} u}{\partial \xi^m \partial \eta^n}(\xi_p, \eta_p)\,, \tag{3.12}$$

and the nodal values of the above partial differentials are obtained in the matrix form as

$$\mathbf{U}_{\xi\eta}^{(mn)} = \mathbf{D}_{\xi}^{m}\mathbf{D}_{\eta}^{n}\mathbf{u}. \tag{3.13}$$

The partial differentials for 2D and 3D domains at each node can be obtained by 1D differential matrix of first order $\mathbf{D}_0$, which is different from that by using either the moving least square or radial bases function interpolation with support domain technique [56]. Undoubtedly, the program effort should be reduced as only one differential matrix $\mathbf{D}_0\ (N \times N)$ is utilized [62].

3.3 Mapping Technique of FBM

3.3.1 Two Dimensions

Mapping technique is employed to transfer from a normalized domain ($\xi o \eta$) to a real domain (xoy), 8 seeds are selected in the real domain corresponding to the normalized domain. For 2D problem, a block with 8 seeds is shown in Figure 3.4. The shape functions are given as

$$\begin{aligned} N_i &= \frac{1}{4}(1+\xi_i\xi)(1+\eta_i\eta)(\xi_i\xi+\eta_i\eta-1) \quad \text{for} \quad i=1,2,3,4, \\ N_i &= \frac{1}{2}(1-\xi^2)(1+\eta_i\eta) \quad \text{for} \quad i=5,7, \\ N_i &= \frac{1}{2}(1-\eta^2)(1+\xi_i\xi) \quad \text{for} \quad i=6,8 \end{aligned} \tag{3.14}$$

and their partial differential with respect to normalized axes ξ and η are

$$\begin{aligned} \frac{\partial N_i}{\partial \xi} &= \frac{\xi_i}{4}(1+\eta_i\eta)(2\xi_i\xi+\eta_i\eta), \\ \frac{\partial N_i}{\partial \eta} &= \frac{\eta_i}{4}(1+\xi_i\xi)(\xi_i\xi+2\eta_i\eta) \quad \text{for} \quad i=1,2,3,4, \\ \frac{\partial N_i}{\partial \xi} &= -\xi(1+\eta_i\eta), \\ \frac{\partial N_i}{\partial \eta} &= \frac{\eta_i}{2}(1-\xi^2) \quad \text{for} \quad i=5,7, \\ \frac{\partial N_i}{\partial \xi} &= \frac{\xi_i}{2}(1-\eta^2), \\ \frac{\partial N_i}{\partial \eta} &= -\eta(1+\xi_i\xi) \quad \text{for} \quad i=6,8. \end{aligned} \tag{3.15}$$

The coordinate of the real domain transferred from mapping domain is defined

$$x=\sum_{k=1}^{8}N_k(\xi,\eta)x_k,\ \ y=\sum_{k=1}^{8}N_k(\xi,\eta)y_k\ . \tag{3.16}$$

For partial differentials of function $u(x,y)$ in Cartesian coordinate system, one has

$$\frac{\partial u}{\partial x}=\frac{1}{J}\left(\beta_{11}\frac{\partial u}{\partial \xi}+\beta_{12}\frac{\partial u}{\partial \eta}\right),\ \ \frac{\partial u}{\partial y}=\frac{1}{J}\left(\beta_{21}\frac{\partial u}{\partial \xi}+\beta_{22}\frac{\partial u}{\partial \eta}\right), \tag{3.17}$$

where

$$J=\begin{vmatrix}\dfrac{\partial x}{\partial \xi} & \dfrac{\partial x}{\partial \eta}\\ \dfrac{\partial y}{\partial \xi} & \dfrac{\partial y}{\partial \eta}\end{vmatrix},\beta_{11}=\frac{\partial y}{\partial \eta},\beta_{12}=-\frac{\partial y}{\partial \xi},\beta_{21}=-\frac{\partial x}{\partial \eta},\beta_{22}=\frac{\partial x}{\partial \xi}. \tag{3.18}$$

Therefore, the first partial differential matrices can be written as

$$\mathbf{U}_x=\mathbf{\Delta}_{11}\mathbf{U}_\xi^{(1)}+\mathbf{\Delta}_{12}\mathbf{U}_\eta^{(1)}=\left(\mathbf{\Delta}_{11}\mathbf{D}_\xi+\mathbf{\Delta}_{12}\mathbf{T}\mathbf{D}_\xi\mathbf{T}^{-1}\right)\mathbf{u}=\mathbf{D}_x\mathbf{u}\ , \tag{3.19}$$

$$\mathbf{U}_y=\mathbf{\Delta}_{21}\mathbf{U}_\xi^{(1)}+\mathbf{\Delta}_{22}\mathbf{U}_\eta^{(1)}=\left(\mathbf{\Delta}_{21}\mathbf{D}_\xi+\mathbf{\Delta}_{22}\mathbf{T}\mathbf{D}_\xi\mathbf{T}^{-1}\right)\mathbf{u}=\mathbf{D}_y\mathbf{u}\ , \tag{3.20}$$

where

$$\mathbf{\Delta}_{ij}=\begin{pmatrix}\beta_{ij}^{(1)}/J^{(1)} & 0 & \ldots & 0\\ 0 & \beta_{ij}^{(2)}/J^{(2)} & \ldots & 0\\ \ldots & \ldots & \ldots & \ldots\\ 0 & 0 & \ldots & \beta_{ij}^{(M)}/J^{(M)}\end{pmatrix} \tag{3.21}$$

and $\beta_{ij}^{(p)}/J^{(p)}$ is obtained by Equation (3.18) at collocation point (ξ_p,η_p). So that matrix $\mathbf{D}_x$ and $\mathbf{D}_y$ can be solved by $\mathbf{D}_\xi$ and $\mathbf{D}_\eta$. It means that the first partial derivatives in the real domain (xoy) can be determined in terms of the first order differential matrix in the normalized domain $\xi o\eta$ ($|\xi|\le 1;|\eta|\le 1$) with nodal value vector.

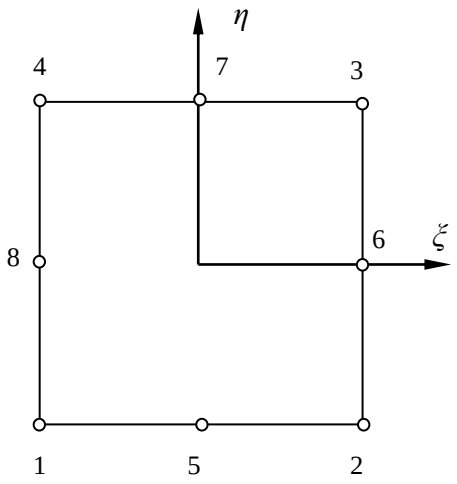

Figure 3.4 Quadratic element and its node distribution for two-dimension.

3.3.2 Three Dimensions

For three-dimensional problems, consider a cubic with uniform length as shown in Figure 3.5 in coordinate system $\xi\eta\varsigma$ and define

$$U_{\xi p}(\xi_p,\eta_p,\varsigma_p)=\frac{\partial u}{\partial \xi}(\xi_p,\eta_p,\varsigma_p) \tag{3.22}$$

and the number of point $p=N^2\times(k-1)+N\times(j-1)+i$, where i, j and k denote the number of rows and the number of columns respectively. Similar as 2D cases, this numbering system is defined as global numbering system in the numerical simulations. The value of the partial differentials for each node can be expressed, in a matrix form, as

$$\mathbf{U}_{\xi}=\mathbf{D}_{\xi}\mathbf{u}\,, \tag{3.23}$$

where the vector of derivative nodal value $U_{\xi}=[U_{\xi 1},U_{\xi 2},...,U_{\xi M}]^T$ and M is the number of total collocation points ($M=N\times N\times N$ shown in Figure 3.5). For a cubic

domain in the normalized coordinate and numbering system, the first order differential matrix in global numbering system for all nodes is

$$\mathbf{D}_{\xi} = \underbrace{\begin{pmatrix} \mathbf{D}_0 & 0 & \ldots & 0 \\ 0 & \mathbf{D}_0 & 0 & 0 \\ \ldots & \ldots & \ldots & \ldots \\ 0 & 0 & 0 & \mathbf{D}_0 \end{pmatrix}}_{M\times M\times M}, \tag{3.24}$$

in which $\mathbf{D}_0$ is differential matrix for one-dimension given in Eq. (3.24) with dimension $N \times N \times N$. For a three-dimensional case, the global numbering system is shown in Figure 3.5. Following the same way for two-dimension and using transform matrix, one has

$$\mathbf{U}_{\eta} = \mathbf{T}_{\eta}\mathbf{D}_{\xi}\mathbf{T}_{\eta}^{-1}\mathbf{u} = \mathbf{D}_{\eta}\mathbf{u} \tag{3.25}$$

and

$$\mathbf{U}_{\varsigma} = \mathbf{T}_{\varsigma}\mathbf{D}_{\xi}\mathbf{T}_{\varsigma}^{-1}\mathbf{u} = \mathbf{D}_{\varsigma}\mathbf{u}\,. \tag{3.26}$$

The definition of the collocation point p can be illustrated in three numbering systems, including one global numbering and two local numbering systems. For example, in global system (ξ), $p = N^2(k-1) + N\times(j-1) + i$, while in the local system (η), $p = N^2(k-1) + N\times(i-1) + j,$ and in the local system (ζ), $p = N^2(i-1) + N\times(j-1) + k.$ Hence, in coordinate transformed matrices $\mathbf{T}_{\eta}$ and $\mathbf{T}_{\varsigma}$, all elements are zero except $T^{\eta}_{N^2\times(k-1)+N\times(j-1)+i,\,N^2\times(k-1)+N\times(i-1)+j} = 1$ and $T^{\varsigma}_{N^2\times(k-1)+N\times(j-1)+i,\,N^2\times(i-1)+N\times(j-1)+k} = 1$ $(i, j, k = 1,2,\ldots,N)$ respectively. Besides, the different orders of derivatives with respect to all coordinates ξ, η and ς can be simply obtained as follow:

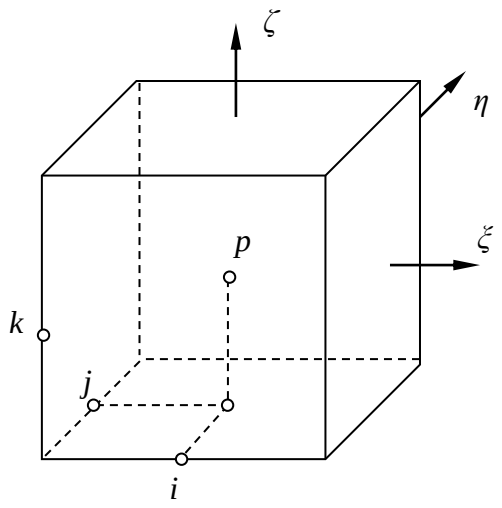

Figure 3.5 Numbering system for three-dimensional problem.

$$U_{\xi\eta\varsigma}^{(mnl)}(\xi_p,\eta_p,\varsigma_p)=\frac{\partial^{m+n+l}u}{\partial\xi^m\partial\eta^n\partial\varsigma^l}(\xi_p,\eta_p,\varsigma_p) \tag{3.27}$$

and Eq. (3.27) can be rewrite, in matrix form, as

$$\mathbf{U}_{\xi\eta\varsigma}^{(mnl)}=\mathbf{D}_{\xi}^{m}\mathbf{D}_{\eta}^{n}\mathbf{D}_{\varsigma}^{l}\mathbf{u}. \tag{3.28}$$

Eq. (3.28) indicates that, for any order of derivatives based on the coefficient of differential matrix which can be derived from the one-dimensional differential matrix $\mathbf{D}_0$.

For three-dimensional problems, quadratic shape function with 20 seeds is used. Shape functions can be written as follows

$$N_i=\frac{1}{8}(1+\xi_i\xi)(1+\eta_i\eta)(1+\varsigma_i\varsigma)(\xi_i\xi+\eta_i\eta+\varsigma_i\varsigma-2) \text{ for } i=1,2,3,4,5,6,7,8$$

$$N_i=\frac{1}{4}(1-\xi^2)(1+\eta_i\eta)(1+\varsigma_i\varsigma) \text{ for } i=9,11,17,19$$

$$N_i=\frac{1}{4}(1-\eta^2)(1+\varsigma_i\varsigma)(1+\xi_i\xi) \text{ for } i=10,12,18,20 \tag{3.29}$$

$$N_i = \frac{1}{4}(1-\varsigma^2)(1+\xi_i\xi)(1+\eta_i\eta) \quad \text{for} \quad i = 13,14,15,16$$

Their partial differentials of shape function are listed as below

$$\frac{\partial N_i}{\partial \xi} = \frac{\xi_i}{8}(1+\eta_i\eta)(1+\varsigma_i\varsigma)(2\xi_i\xi+\eta_i\eta+\varsigma_i\varsigma-1),$$

$$\frac{\partial N_i}{\partial \eta} = \frac{\eta_i}{8}(1+\xi_i\xi)(1+\varsigma_i\varsigma)(\xi_i\xi+2\eta_i\eta+\varsigma_i\varsigma-1),$$

$$\frac{\partial N_i}{\partial \varsigma} = \frac{\varsigma}{8}(1+\xi_i\xi)(1+\eta_i\eta)(\xi_i\xi+\eta_i\eta+2\varsigma_i\varsigma-1) \quad \text{for } i = 1,2,3,4,5,6,7,8$$

$$\frac{\partial N_i}{\partial \xi} = -\frac{1}{2}\xi(1+\eta_i\eta)(1+\varsigma_i\varsigma),$$

$$\frac{\partial N_i}{\partial \eta} = \frac{1}{4}\eta_i(1-\xi^2)(1+\varsigma_i\varsigma),$$

$$\frac{\partial N_i}{\partial \varsigma} = \frac{1}{4}\varsigma_i(1-\xi^2)(1+\eta_i\eta) \quad \text{for } i = 9,11,17,19 \tag{3.30}$$

$$\frac{\partial N_i}{\partial \xi} = \frac{1}{4}\xi_i(1-\eta^2)(1+\varsigma_i\varsigma),$$

$$\frac{\partial N_i}{\partial \eta} = -\frac{1}{2}\eta(1+\varsigma_i\varsigma)(1+\xi_i\xi),$$

$$\frac{\partial N_i}{\partial \varsigma} = \frac{1}{4}\varsigma_i(1-\eta^2)(1+\xi_i\xi) \quad \text{for} \quad i = 10,12,18,20$$

$$\frac{\partial N_i}{\partial \xi} = \frac{1}{4}\xi_i(1-\varsigma^2)(1+\eta_i\eta),$$

$$\frac{\partial N_i}{\partial \eta} = \frac{1}{4}\eta_i(1-\varsigma^2)(1+\xi_i\xi),$$

$$\frac{\partial N_i}{\partial \varsigma} = -\frac{1}{2}\varsigma(1+\xi_i\xi)(1+\eta_i\eta) \quad \text{for} \quad i = 13,14,15,16$$

Same as two-dimensional problems, the coordinate transform (mapping) can be written as

$$x=\sum_{k=1}^{20}N_k(\xi,\eta,\varsigma)x_k,\ \ y=\sum_{k=1}^{20}N_k(\xi,\eta,\varsigma)y_k\ \ \ z=\sum_{k=1}^{20}N_k(\xi,\eta,\varsigma)z_k\ . \tag{3.31}$$

Then the partial differentials of shape functions are

$$\begin{aligned}
\frac{\partial u}{\partial x}&=\frac{1}{J}\left(\frac{\partial u}{\partial \xi}\beta_{11}+\frac{\partial u}{\partial \eta}\beta_{12}+\frac{\partial u}{\partial \varsigma}\beta_{13}\right),\\
\frac{\partial u}{\partial y}&=\frac{1}{J}\left(\frac{\partial u}{\partial \xi}\beta_{21}+\frac{\partial u}{\partial \eta}\beta_{22}+\frac{\partial u}{\partial \varsigma}\beta_{23}\right),\\
\frac{\partial u}{\partial z}&=\frac{1}{J}\left(\frac{\partial u}{\partial \xi}\beta_{31}+\frac{\partial u}{\partial \eta}\beta_{32}+\frac{\partial u}{\partial \varsigma}\beta_{33}\right),
\end{aligned} \tag{3.32}$$

where

$$J=\begin{vmatrix}
\dfrac{\partial x}{\partial \xi} & \dfrac{\partial x}{\partial \eta} & \dfrac{\partial x}{\partial \varsigma}\\
\dfrac{\partial y}{\partial \xi} & \dfrac{\partial y}{\partial \eta} & \dfrac{\partial y}{\partial \varsigma}\\
\dfrac{\partial z}{\partial \xi} & \dfrac{\partial z}{\partial \eta} & \dfrac{\partial z}{\partial \varsigma}
\end{vmatrix} \tag{3.33}$$

and coefficients

$$\beta_{11}=\frac{\partial y}{\partial \eta}\frac{\partial z}{\partial \varsigma}-\frac{\partial y}{\partial \varsigma}\frac{\partial z}{\partial \eta},\beta_{12}=-\frac{\partial y}{\partial \xi}\frac{\partial z}{\partial \varsigma}+\frac{\partial y}{\partial \varsigma}\frac{\partial z}{\partial \xi},\beta_{13}=\frac{\partial y}{\partial \xi}\frac{\partial z}{\partial \eta}-\frac{\partial y}{\partial \eta}\frac{\partial z}{\partial \xi}, \tag{3.34a}$$

$$\beta_{21}=-\frac{\partial x}{\partial \eta}\frac{\partial z}{\partial \varsigma}+\frac{\partial x}{\partial \varsigma}\frac{\partial z}{\partial \eta},\beta_{22}=\frac{\partial x}{\partial \xi}\frac{\partial z}{\partial \varsigma}-\frac{\partial x}{\partial \varsigma}\frac{\partial z}{\partial \xi},\beta_{23}=-\frac{\partial x}{\partial \xi}\frac{\partial z}{\partial \eta}+\frac{\partial x}{\partial \eta}\frac{\partial z}{\partial \xi}, \tag{3.34b}$$

$$\beta_{31}=\frac{\partial x}{\partial \eta}\frac{\partial y}{\partial \varsigma}-\frac{\partial x}{\partial \varsigma}\frac{\partial y}{\partial \eta},\beta_{32}=-\frac{\partial x}{\partial \xi}\frac{\partial y}{\partial \varsigma}+\frac{\partial x}{\partial \varsigma}\frac{\partial y}{\partial \xi},\beta_{33}=\frac{\partial x}{\partial \xi}\frac{\partial y}{\partial \eta}-\frac{\partial x}{\partial \eta}\frac{\partial y}{\partial \xi}. \tag{3.34c}$$

Therefore, substituting Eq. (3.33) and Eq. (3.34) to Eq. (3.32) , in matrix form, as

$$\mathbf{U}_x=\mathbf{\Delta}_{11}\mathbf{U}_\xi^{(1)}+\mathbf{\Delta}_{12}\mathbf{U}_\eta^{(1)}+\mathbf{\Delta}_{13}\mathbf{U}_\varsigma^{(1)}=\left(\mathbf{\Delta}_{11}\mathbf{D}_\xi+\mathbf{\Delta}_{12}\mathbf{D}_\eta+\mathbf{\Delta}_{13}\mathbf{D}_\varsigma\right)\mathbf{u}=\mathbf{D}_x\mathbf{u}, \tag{3.35a}$$

$$\mathbf{U}_y=\mathbf{\Delta}_{21}\mathbf{U}_\xi^{(1)}+\mathbf{\Delta}_{22}\mathbf{U}_\eta^{(1)}+\mathbf{\Delta}_{23}\mathbf{U}_\varsigma^{(1)}=\left(\mathbf{\Delta}_{21}\mathbf{D}_\xi+\mathbf{\Delta}_{22}\mathbf{D}_\eta+\mathbf{\Delta}_{23}\mathbf{D}_\varsigma\right)\mathbf{u}=\mathbf{D}_y\mathbf{u}, \tag{3.35b}$$

$$\mathbf{U}_z=\mathbf{\Delta}_{31}\mathbf{U}_\xi^{(1)}+\mathbf{\Delta}_{32}\mathbf{U}_\eta^{(1)}+\mathbf{\Delta}_{33}\mathbf{U}_\varsigma^{(1)}=\left(\mathbf{\Delta}_{31}\mathbf{D}_\xi+\mathbf{\Delta}_{32}\mathbf{D}_\eta+\mathbf{\Delta}_{33}\mathbf{D}_\varsigma\right)\mathbf{u}=\mathbf{D}_z\mathbf{u}, \tag{3.35c}$$

where $\mathbf{\Lambda}_{ij}$ is defined in Eq. (3.21), matrix $\mathbf{D}_{\eta}$ and $\mathbf{D}_{\varsigma}$ are defined in previous sections, which can be written in terms of $\mathbf{D}_{\xi}$ by a transformation matrix derived by the numbering system. Again, the first partial differentials can be determined in terms of the first order differential matrix in the normalized domain $\xi\eta\varsigma$ ($|\xi| \le 1$; $|\eta| \le 1$; $|\varsigma| \le 1$) with nodal values in the equation above. In addition, the different order of differentials with respect to the Cartesian coordinates (xyz) can be written as

$$U_{xyz}^{(mnl)}(x_p, y_p, z_p) = \frac{\partial^{m+n+l} u}{\partial x^m \partial y^n \partial z^l}(x_p, y_p, z_p) \tag{3.36}$$

and the nodal values of the above partial differential are obtained in the matrix form by

$$\mathbf{U}_{xyz}^{(mnl)} = \mathbf{D}_x^m \mathbf{D}_y^n \mathbf{D}_z^l \mathbf{u}. \tag{3.37}$$

3.4 Examples of the Finite Block Method

The quality of Meshfree Method firstly relies on the error of the interpolation method, and for the FBM, it is the Lagrangian Interpolation Method. In this section, the FBM with the Lagrangian Interpolation Method is investigated for the analysis of a two-dimensional plane. The field function $u(x, y)$ for every interpolation point (x, y) can be interpolated by the nodes defined in the normalized domain and transferred via the mapping technique. The average errors of function values over the entire domain are defined as follows

$$e = \frac{1}{M} \sum_{i=1}^{M} \left| \frac{u_i - u_i^*}{u_i^*} \right| \tag{3.38}$$

where M is the total number of the entire domain, e is the average error, u_i^* is the approximated values of function. For the accuracy and convergence study of the FBM, the continuous equation for a non-polynomial surface is observed as

$$u^* = e^{xy} + \cos(xy), \quad -1 \le x \le 1, -1 \le y \le 1 \tag{3.39}$$

The governing equation is considered as

$$\frac{\partial^2 u}{\partial x^2} + \frac{\partial^2 u}{\partial y^2} = b \tag{3.40}$$

where b is the term of the body force. Substituting Eq. (3.39) into Eq. (3.40) gives

$$b = (x^2 + y^2)(e^{xy} - \cos(xy)). \tag{3.41}$$

And the boundary conditions are as

$$\begin{aligned} &u = e^{xy} + \cos(xy), \quad x = -1, y = -1 \\ &\frac{\partial u}{\partial x} = ye^{xy} - y\sin(xy), \qquad x = 1 \\ &\frac{\partial u}{\partial y} = xe^{xy} - x\sin(xy). \qquad y = 1 \end{aligned} \tag{3.42}$$

Appling the FBM, Eq. (3.40) can be transferred into a series of algebraic functions, in a matrix form, as follows:

$$\mathbf{D}_x\mathbf{D}_x\mathbf{u}^* + \mathbf{D}_y\mathbf{D}_y\mathbf{u}^* = \mathbf{b}(x, y) \tag{3.43}$$

in which $\mathbf{D}_x, \mathbf{D}_y$ are the first order differential matrix in 2D problems, $\mathbf{u}^* = [u_1^*, u_2^*, u_3^*, ...u_M^*]^T$ is the approximated value of each interpolation node.

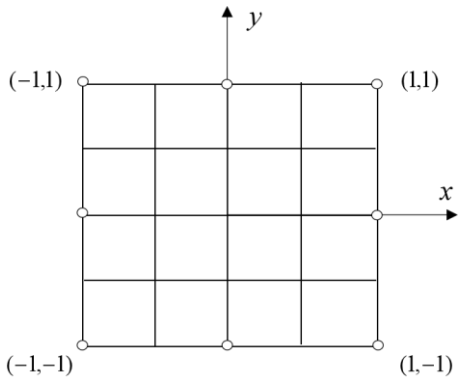

Figure 3.6 Block of a square plate and their mapping seeds with 5 nodes selected.

1) Accuracy studies

The interpolation errors of the FBM is shown in Figure 3.7 and Figure 3.8. The total number of nodes selected for the calculation is M=25, only 5 nodes are picked for the error test. From the figures one can obtain that the accuracy in the fitted function itself is higher than that in the derivatives. And the higher the derivatives, the lower the accuracy. However, it can be observed that the error for both results are under 0.1%, which is acceptable for numerical analysis.

2) Convergence studies

In the convergence study, regularly and evenly distributed 25, 49, 81, and 121, nodes are used. In addition, the Chebyshev node distributions are also applied for the comparison. The relative errors defined in Eq. (3.38) are shown in Table 3.1 (regular node distribution) and Table 3.2 (irregular node distribution), where u_i and u_i^* indicate the numerical and analytical solutions on each node respectively for different order of derivatives. Good agreement has been made by comparison of the analytical result, thus the convergence and degree of the accuracy can be confirmed. As shown in Table 3.1 and Table 3.2, in the case of

$N = 7$, the error for the first order derivative is less than 0.1%. Furthermore, there is slightly difference between the solution of regular node distribution and irregular node distribution when N=5. Therefore, in most of the cases, any node distribution would be acceptable for the simulation.

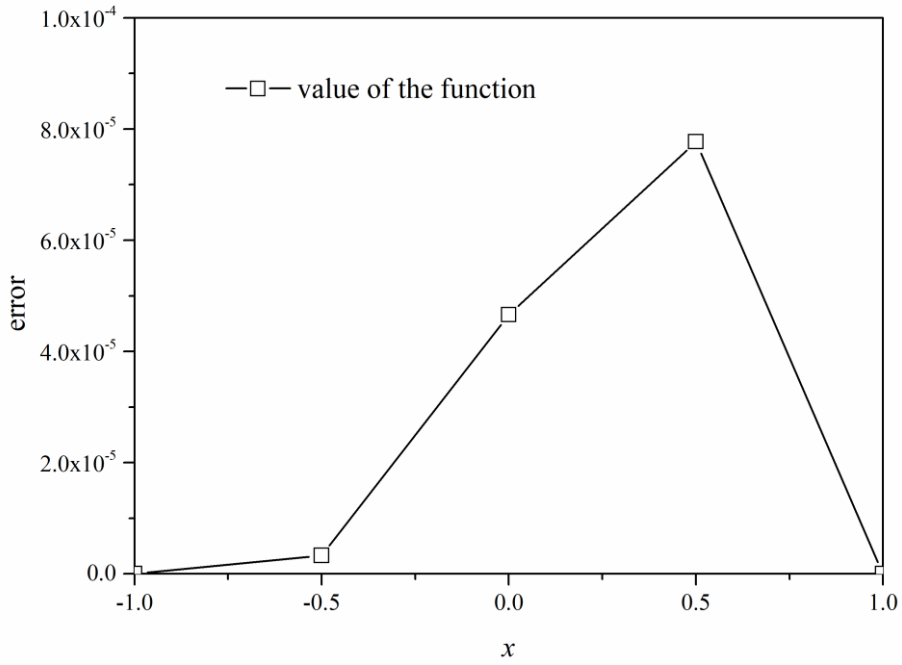

Figure 3.7 The interpolation errors for the value of the function. The nodes selected are $(0,-1),(0,-0.5),(0,0),(0,0.5),(0,1)$.

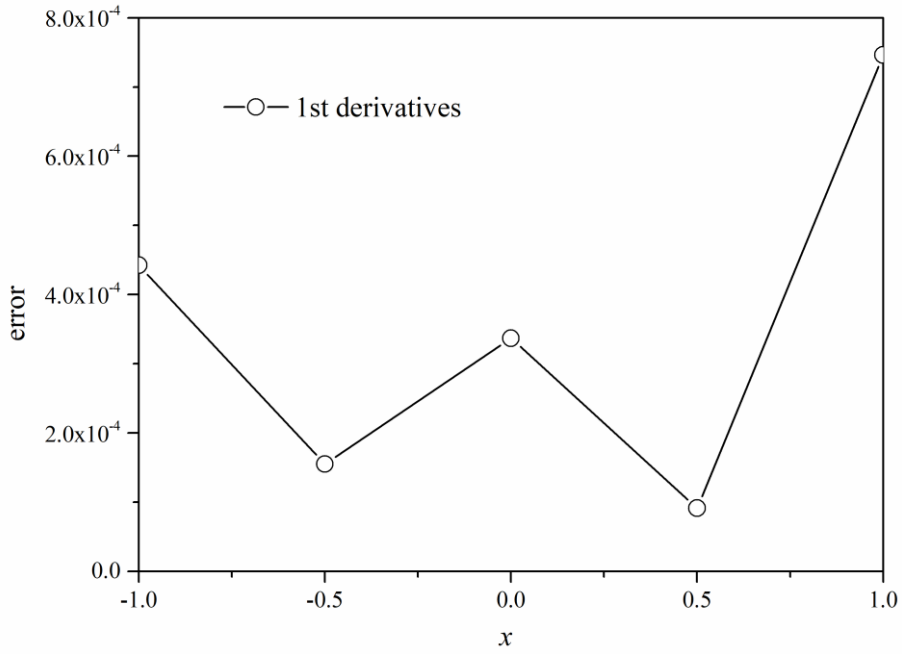

Figure 3.8 The interpolation errors of the 1st derivatives of the function. The nodes selected are $(0,-1),(0,-0.5),(0,0),(0,0.5),(0,1)$.

Table 3.1 Average errors e for regular node distribution.

N	u	$\partial u/\partial x$	$\partial^2 u/\partial x^2$	$\partial^2 u/\partial x\partial y$
5	6.6031×10^{-6}	2.900×10^{-3}	2.020×10^{-2}	2.240×10^{-2}
7	1.7357×10^{-7}	2.3235×10^{-5}	2.8994×10^{-4}	2.3998×10^{-4}
9	1.4245×10^{-9}	1.2195×10^{-7}	2.2726×10^{-6}	1.4786×10^{-6}
11	7.6481×10^{-12}	4.5768×10^{-10}	1.1428×10^{-8}	6.3037×10^{-9}

Table 3.2 Average errors e for Chebyshev node distribution.

N	u	$\partial u/\partial x$	$\partial^2 u/\partial x^2$	$\partial^2 u/\partial x\partial y$
5	0.8924×10^{-6}	0.2596×10^{-3}	0.5326×10^{-2}	0.8856×10^{-2}
7	0.1896×10^{-7}	0.1453×10^{-4}	0.4587×10^{-4}	0.1546×10^{-4}
9	0.2567×10^{-9}	0.4689×10^{-7}	0.5698×10^{-6}	0.3654×10^{-6}
11	0.1537×10^{-12}	0.2365×10^{-10}	0.5486×10^{-8}	0.2654×10^{-9}

3.5 Conclusion

The Finite Block Method is a type of Meshless method, based on a first order derivative matrix derived from the Lagrange Interpolation Method. This coefficient matrix can be obtained from a normalized system with 8 seeds for 2D and 20 seeds for 3D problems. Mapping Technology is applied in FBM to transfer the normalized domain to real domain by seeds selected. The basic functions and strategy of Finite Block Method was presented in this chapter with both 2D and 3D cases. However, only a test function in 2D is applied, in the end, to verify the convergence and accuracy of the FBM when compare with the analytical solutions. The essential features of the FBM in this chapter can be summarized as:

1) A complex physical domain can be divided into several sub-domains. Each domain can be interpolated by a normalized block with the coefficient differential matrix;

2) The different orders of derivatives for the collocation points can be attained by a first order differential matrix derived from the Lagrange Interpolation Method in normalized domain straightforward;
3) By the comparison with analytical solutions, the convergence and accuracy of the FBM can be approved.

Chapter 4

Finite Block Method for Functionally Graded Materials: Statics

4.1 Introduction

In recent years, many research has been focused on the development of Functionally Graded Materials, which shows promising applications for cases requiring specific material properties such as ceramic/metal materials. The application of such an FGM to a system means this system can benefit from both ceramic and metals properties, e.g., high heat and corrosion protection by the ceramics, and high stiffness and toughness of metals. Due to its controllable property, this type of materials are very attractive for demanding applications like electronic devices, corrosion-resistance, thermal barrier coatings and biomaterials [63, 64]. This urgent demand has resulted in the development of different types of FGMs, including chemical composition gradient FGMs [65, 66], the porosity gradient FGMs [67, 68] and the microstructural gradient FGMs. In order to take full advantage of this new material, fundamental studies on fracture mechanics are required in conjunction with the design and manufacturing of the materials.

Fracture mechanics of FGMs was first presented by Erdogan in 1995 [5]. In his remarkable work, FGMs are as an interface of generally incompatible materials and

would significantly enhance the bonding strength compared with the traditional composite materials. Besides the stress singularity at the interface boundary, the bonded material can be eliminated by the application of FGMs. In 1996, Jin and Batra [69] described the crack-tip field by the use of Airy stress function and presented the stress intensity factor of an edge-crack strip of FGM. Also, both the domain-related method such as FEM and the boundary-related method like BEM can be applied to the analysis of FGMs.

In 1987, Eischen [70] considered the analysis of non-homogeneous materials based on its Young's modulus vary generally and continuously along the geometry by FEM. The stress and displacement distribution around the crack tip was attained by the expansion of Williams series. In 2000, Anlas and Santare [71] proposed their work on uncracked and cracked plate under uniform load and uniform displacement by FEM. The stress intensity factor was obtained for an edge-crack plate with the energy release rate and the J-integral method. Compare to the analytical result, the different sizes of the mesh were evaluated. Additionally, Li [72] tested experimentally the relationship between the stress and crack length of a propagating crack in an FGM created by controllable ultraviolet (UV) irradiation of a polymer. This relationship was then utilized as the boundary conditions at each increment of crack propagation by FEM. The fracture toughness of FGMs was assessed numerically in the end. In [73], Marur analyzed the stress singularity at the crack tip parametrically by FEM. The crack opening displacement (COD) of FGMs was compared with the isotropic materials and bimaterials as well. In 2002, Kim and Paulino [8] evaluated the mix-mode stress intensity factor of FGMs for static analysis by FEM. Three different approaches for stress intensity factor have been investigated and compared in this paper, including the

J-integral, Modified Crack Closure (MCC) integral method and the Displacement Correlation Technique (DCT). In addition, there are many more advanced finite element methods including the graded FEM [74], the extended FEM [6] and the enriched FEM [75, 76].

In 1993, Sollero and Aliabadi [77] presented the Boundary Element Method (BEM) on anisotropic materials. The bulk of this work focuses on the mixed-mode stress intensity factor on a composite laminate. In 2003, the Boundary Element Method (BEM) combined with the Generalized Kelvin Solution (GKS) was applied to investigate the crack on FGMs whose top and bottom boundaries were conjoint with different isotropic materials by Yue and Xiao [78]. An eight-node traction-singular boundary element was used for the stress singularity around the crack tip together with the multi-region method to assess the performance of the crack. Moreover, the evaluation of an elliptical crack was also presented in this paper. The effect of the elastic modulus and thickness of the FGMs are discussed. In 2003, Zhang and Savaidis [79] proposed the Boundary Integral Equation Method (BIEM) for transient dynamic analysis of a crack on an infinite plate of FGMs. The numerical results in their work showed that the material gradients have a substantial effect on the Dynamic SIFs. Similarly in 2005, Zhang and Sladek [80] investigated a crack in an FGM subjected to anti-plane load by the BIEM method. The influence of the material gradients to the SIFs was also confirmed. Furthermore, in 2008, Gao and Zhang [81] introduced the fracture analysis of a FGM rectangular plate with an edge-crack and subjected to tensile load. The BEM was applied to nonhomogeneous, isotropic and linear elastic FGMs for the fundamental solutions of crack problems. The elastic modulus was assumed to exponentially vary along the geometry in this case.

The application of FEM and the BEM on Functionally Graded Materials for both static and dynamic analysis has been discussed in the paragraphs above, and the effectiveness and convenience of these numerical methods can be confirmed. However, the development of new and advance methods is still a key topic in fracture mechanics of FGMs because of the difficulty in handling complex domain and the extra programming effort caused by fine mesh.

Recently, many Meshless Methods are very attractive due to their higher flexibility and lower program codding for numerical technology. In 2005, Sladek [82] developed a new numerical method to calculate the dynamic SIFs of an FGMs plate with an edge-crack. In this paper, the Moving Least Square (MLS) approach and Laplace Transform were applied to deal with the spatial dependent variables and time dependent variables respectively. The comparison of spatial variable mass density and uniform mass density was investigated. In addition, the method named Meshless LBIEM was applied to crack problems subjected to transient dynamic anti-plane loading in FGMs by Sladek in [83]. The advantage of this method would be the physical domain can be divided into several small sub-domains, which can be represented by a series of LBIEs. In contrast to the traditional FEM or BEM for dynamic analysis, the mesh regenerated caused by the time increment is not necessary in this method. Moreover, in 2006, Sladek [84] proposed a Meshless method based on the local Petrov-Galerkin approach for crack analysis under both thermal and impact loads in orthotropic FGMs. A path independent integral was adopted to assess the stress intensity factors and *T*-stresses around the crack tip for a central crack of a finite plate. In 2017, Dai [85] presented a complex variable Meshless Local Petrov-Galerkin (CVMLPG) method for dynamic analysis on FGMs. Rather than the traditional MLS, this method has the advantage of less number of

unknown coefficients when constructing the shape function, which means higher efficiency and accuracy. In 2014, the Finite Block Method was applied to solve the static elastic problems on FGMs in a strong form by Wen [9]. The next year, Wen [58] developed the Finite Block Method in conjunction with Local Petrov-Galerkin method, namely Finite Block Petrov-Galerkin (FBPG) method to solve the problems of transient heat conduction.

In this chapter, the strategy of the FBM for static analysis in FGMs is presented. The stress intensity factors can be calculated by the Crack Opening Displacement method. Several numerical examples are presented and obtained results are compared with published papers to confirm the accuracy and convergence of this method.

4.2 Formulation of FBM for Anisotropic Functional Graded Materials

Assumed that the material properties are dependent on the spatial coordinates in a non-homogeneous material. The relationship between stress and strain in anisotropic materials is given by

$$\begin{bmatrix} \varepsilon_x \\ \varepsilon_y \\ 2\gamma_{xy} \end{bmatrix} = \begin{bmatrix} \beta_{11} & \beta_{12} & \beta_{16} \\ \beta_{12} & \beta_{22} & \beta_{26} \\ \beta_{16} & \beta_{26} & \beta_{66} \end{bmatrix} \begin{bmatrix} \sigma_x \\ \sigma_y \\ \tau_{xy} \end{bmatrix}. \tag{4.1}$$

where β_{ij} are the elastic compliance of the FGMs. The compliance coefficients can be written in terms of the engineering constants as

$$\begin{aligned} &\beta_{11} = 1/E_1, \beta_{22} = 1/E_2, \beta_{12} = -\nu_{12}/E_1 = -\nu_{21}/E_2, \\ &\beta_{16} = \eta_{12,1}/E_1 = \eta_{1,12}G_{12}, \beta_{26} = \eta_{12,2}/E_2 = \eta_{2,12}G_{12}, \beta_{66} = 1/G_{12}, \end{aligned} \tag{4.2}$$

where E_1 and E_2 are the Young's modulus along x and y axis respectively, $\nu_{12} = \nu_{21}$ are the Poisson's ratios, G_{12} is the shear modulus, $\eta_{jk,l}, \eta_{l,jk}$ are the mutual coefficients of first and second kind.

The inverse form of the relationship in Eq. (4.1) yields

$$\begin{bmatrix} \sigma_x \\ \sigma_y \\ \tau_{xy} \end{bmatrix} = \begin{bmatrix} Q_{11} & Q_{12} & Q_{16} \\ Q_{12} & Q_{22} & Q_{26} \\ Q_{16} & Q_{26} & Q_{66} \end{bmatrix} \begin{bmatrix} \varepsilon_x \\ \varepsilon_y \\ 2\gamma_{xy} \end{bmatrix}. \tag{4.3}$$

For plane stress orthotropic elasticity, the material mechanical constants give

$$Q_{11} = \frac{E_1}{1-\nu_{12}\nu_{21}},\ Q_{12} = \frac{\nu_{12}E_1}{1-\nu_{12}\nu_{21}},\ Q_{22} = \frac{E_2}{1-\nu_{12}\nu_{21}},\ Q_{16} = Q_{26} = 0,\ Q_{66} = G_{12}. \tag{4.4}$$

Consider 2D elasticity of domain Ω with boundary Γ in Functionally Graded Materials. The equilibrium equations for a 2D static elastic analysis in terms of plane stress are as follows:

$$\begin{aligned} &\frac{\partial \sigma_x}{\partial x} + \frac{\partial \tau_{xy}}{\partial y} = b_x, \\ &\frac{\partial \tau_{xy}}{\partial x} + \frac{\partial \sigma_y}{\partial y} = b_y, \end{aligned} \qquad (x, y) \in \Omega \tag{4.5}$$

and the relationship between stress and strain in orthotropic and continuously no-homogeneous media are

$$\begin{aligned} \sigma_x &= Q_{11}\frac{\partial u}{\partial x} + Q_{12}\frac{\partial v}{\partial y}, \\ \sigma_y &= Q_{12}\frac{\partial u}{\partial x} + Q_{22}\frac{\partial v}{\partial y}, \\ \tau_{xy} &= Q_{66}\left(\frac{\partial u}{\partial y} + \frac{\partial v}{\partial x}\right), \end{aligned} \tag{4.6}$$

where u, v are the displacement along x, y coordinates, σ_x, σ_y are the stresses along x, y coordinates, τ_{xy} is the shear stress, b_x, b_y are the body force in the x, y coordinates, and the boundary conditions are given as

$$u(x,y) = \bar{u}(x,y), \quad v(x,y) = \bar{v}(x,y) \qquad (x,y) \in \Gamma_u \tag{4.7a}$$

for displacement on Γ_u, and

$$\sigma_x n_x + \tau_{xy} n_y = \bar{t}_x, \quad \tau_{xy} n_x + \sigma_y n_y = \bar{t}_y \qquad (x,y) \in \Gamma_t \tag{4.7b}$$

for the traction on Γ_t, $n(n_x, n_y)$ are the unit vector normal outward to the boundaries.

Applying the mapping technique and differential matrices obtained in Eq. (3.19) and Eq. (3.20) and substituting Eq. (4.6) into Eq. (4.5) will result in a matrix form as

$$\left(\mathbf{D}_x \mathbf{Q}_{11} \mathbf{D}_x + \mathbf{D}_y \mathbf{Q}_{66} \mathbf{D}_y\right)\mathbf{u} + \left(\mathbf{D}_x \mathbf{Q}_{12} \mathbf{D}_y + \mathbf{D}_y \mathbf{Q}_{66} \mathbf{D}_x\right)\mathbf{v} = \mathbf{b}_x, \tag{4.8}$$

$$\left(\mathbf{D}_y \mathbf{Q}_{12} \mathbf{D}_x + \mathbf{D}_x \mathbf{Q}_{66} \mathbf{D}_y\right)\mathbf{u} + \left(\mathbf{D}_x \mathbf{Q}_{66} \mathbf{D}_x + \mathbf{D}_y \mathbf{Q}_{22} \mathbf{D}_y\right)\mathbf{v} = \mathbf{b}_y, \tag{4.9}$$

where $\mathbf{u} = [u_1, u_2, ..., u_M]^T$, $\mathbf{v} = [v_1, v_2, ..., v_M]^T$, $\mathbf{b} = [b_1, b_2, ..., b_M]^T$ are nodal value vectors and

$$\mathbf{Q}_{ij} = \begin{pmatrix} Q_{ij}^{(1)} & 0 & ... & 0 \\ 0 & Q_{ij}^{(2)} & ... & 0 \\ ... & ... & ... & ... \\ 0 & 0 & ... & Q_{ij}^{(M)} \end{pmatrix}, \tag{4.10}$$

in which $Q_{ij}^{(p)}$ indicates the coefficient at the collocation point. Boundary conditions become

$$\begin{aligned} &u_i = \bar{u}_i, v_i = \bar{v}_i, && (x_i, y_i) \in \Gamma_u \\ &t_{xi} = \bar{t}_{xi}, t_{yi} = \bar{t}_{yi}, && (x_i, y_i) \in \Gamma_t \end{aligned} \tag{4.11}$$

It is no doubt that there are $2M$ linear algebraic equations, and therefore, all nodal values of displacement should be determined for the two-dimensional variable material coefficients. In the case of two and more blocks, the connection conditions should be introduced as

$$\begin{aligned} &u^I(x,y) = u^{II}(x,y), \quad v^I(x,y) = v^{II}(x,y), \\ &t_x^I(x,y) + t_x^{II}(x,y) = 0, \quad t_y^I(x,y) + t_y^{II}(x,y) = 0. \end{aligned} \qquad (x,y) \in \Gamma_{\text{int}} \tag{4.12}$$

For example, in the case of two blocks, the number of total nodes are $4M$ and there are same number of algebraic equations from equilibrium equation, boundary condition and connection condition.

4.3 Stress Intensity Factors with Anisotropic FGM

In 1987, Eischen [70] studied that the singular stress at the crack-tip and the displacement distributions have some form of both non-homogeneous and homogeneous linear elastic materials. Although the structure of the asymptotic crack-tip fields is not influenced by the material gradient parameters in anisotropic FGMs, the stress intensity factors are dependent on the material gradation. Therefore, the simplest and most direct formulations to determine the stress intensity factors are, from Crack Opening Displacement,

$$\begin{aligned} K_{\text{I}} &= \frac{\sqrt{\pi}}{2(\alpha_3\alpha_2 - \alpha_1\alpha_4)\sqrt{2r}}(\alpha_2\Delta u_2 - \alpha_4\Delta u_1), \\ K_{\text{II}} &= \frac{\sqrt{\pi}}{2(\alpha_3\alpha_2 - \alpha_1\alpha_4)\sqrt{2r}}(\alpha_3\Delta u_1 - \alpha_1\Delta u_2), \end{aligned} \tag{4.13}$$

where $\Delta u_i = u_i^+ - u_i^-$, r is the distance of the evaluation point to the crack tip. The four coefficients $\alpha_1, \alpha_2, \alpha_3, \alpha_4$ in Eq. (4.13) are defined as

$$\alpha_1 = \mathrm{Im}\left(\frac{\mu_2 p_1 - \mu_1 P_2}{\mu_1 - \mu_2}\right),\ \alpha_2 = \mathrm{Im}\left(\frac{p_1 - p_2}{\mu_1 - \mu_2}\right),$$
$$\alpha_3 = \mathrm{Im}\left(\frac{\mu_2 q_1 - \mu_1 q_2}{\mu_1 - \mu_2}\right),\ \alpha_4 = \mathrm{Im}\left(\frac{q_1 - q_2}{\mu_1 - \mu_2}\right), \tag{4.14}$$

$$p_k = \beta_{11}\mu_k^2 + \beta_{12} - \beta_{16}\mu_k,\ \ q_k = \beta_{12}\mu_k + \beta_{22}/\mu_k - \beta_{26} \tag{4.15}$$

in which μ_k are the roots of the following characteristic equation

$$\beta_{11}\mu^4 - 2\beta_{16}\mu^3 + (2\beta_{12} + \beta_{66})\mu^2 - 2\beta_{26}\mu + \beta_{22} = 0, \tag{4.16}$$

where all material parameters β_{ij} are specified at the crack tip.

For orthotropic FGMs, the coefficients α_1 and α_4 are equal to zero, and stress intensity factors can be simplified as

$$K_{\mathrm{I}} = \frac{\sqrt{\pi}\Delta u_2}{2\alpha_3\sqrt{2r}} \quad \text{and} \quad K_{\mathrm{II}} = \frac{\sqrt{\pi}\Delta u_1}{2\alpha_2\sqrt{2r}}. \tag{4.17}$$

and for isotropic FGM, they become

$$K_{\mathrm{I}} = \frac{\sqrt{\pi}\Delta u_2}{4E_{\mathrm{tip}}\sqrt{2r}} \quad \text{and} \quad K_{\mathrm{II}} = \frac{\sqrt{\pi}\Delta u_1}{4E_{\mathrm{tip}}\sqrt{2r}}. \tag{4.18}$$

4.4 Numerical Examples

A. Example 4.4.1 a square plate under uniform tension

Consider a square plate of FGM shown in Figure 4.1. The parameters of this model are shown as $w = h = 1, E_1 = E_2 = \exp(\alpha x + \beta y), \sigma_0 = 1, \upsilon_{12} = \upsilon_{21} = 0.3, \alpha = 0, \beta = 0.25,$ the boundary conditions are illustrated in Figure 4.1. Uniform tensile load is applied at the top of the square plate and the bottom of the plate is fixed.

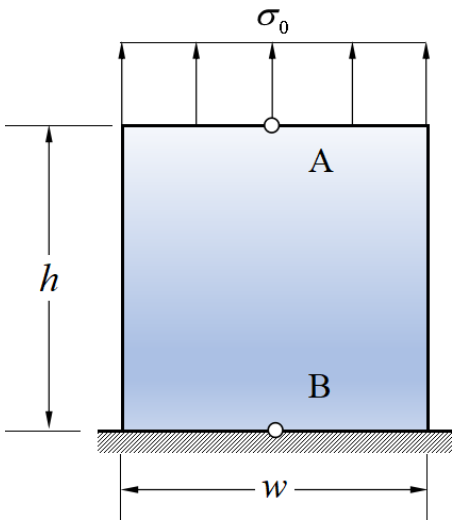

Figure 4.1 A square plate under uniform tensile load on the top.

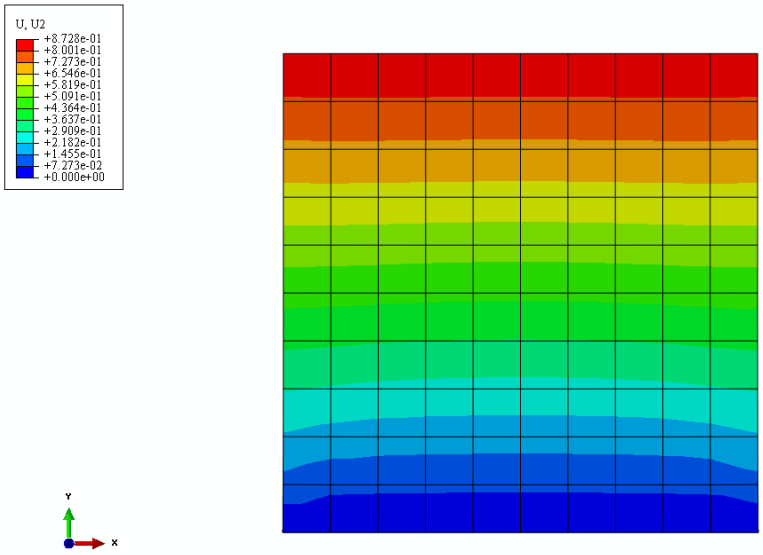

Figure 4.2 The displacement for a square in ABAQUS with 100 elements.

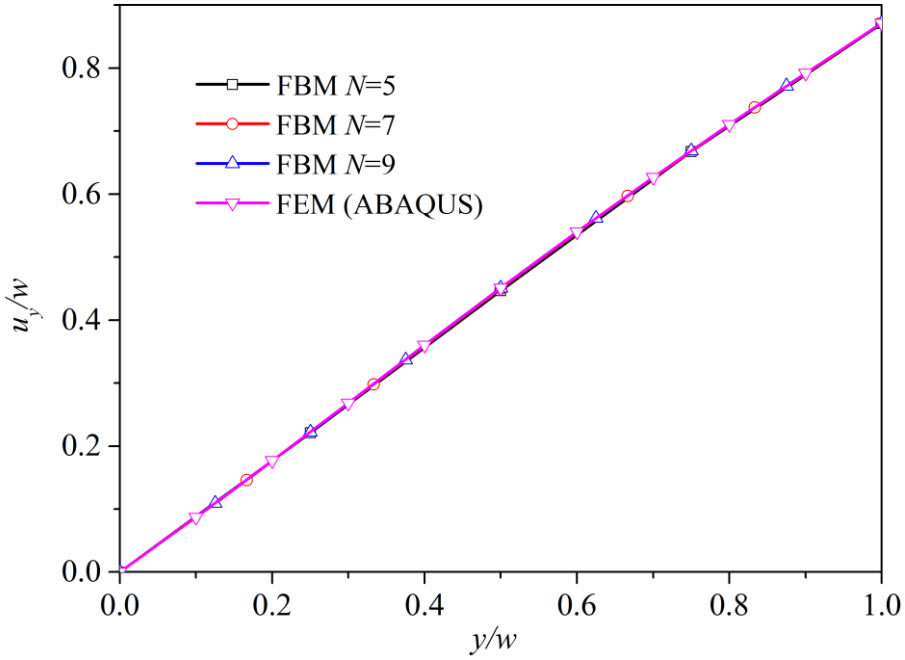

Figure 4.3 The normalized displacement under uniform tensile load.

The displacement for the plate under static tensile force is illuminated in Figure 4.2 by ABAQUS with 100 elements. A comparison of the result for the displacement along the central line of the model (AB in Figure 4.1) by the Finite Block Method and FEM (ABAQUS) is plotted in Figure 4.3, when the number of nodes $N = 5,7,9$ respectively for FBM. Good agreement has been made as shown in Figure 4.3 when N=5.

B. Example 4.4.2 A square plate with a hole in the center under uniform tensile load

Consider a quarter of a square plate with a circular hole as shown in Figure 4.4(a). In order to evaluate the degree of accuracy, the parameters of the material are shown as $a = 2R = 2$, $E_1 = E_2 = \exp(\alpha x + \beta y)$, $\sigma_0 = 1$, $\nu_{12} = \nu_{21} = 0.3$, $\alpha = 0$, $\beta = 0.25$. In this case, two blocks are employed for the analysis of static elasticity for FGMs. The collocation points and 13 mapping seeds for two blocks are shown in Figure 4.4(b). The result of the normalized displacement along the interface of 2 the blocks is plotted against the x axis in Figure 4.6.

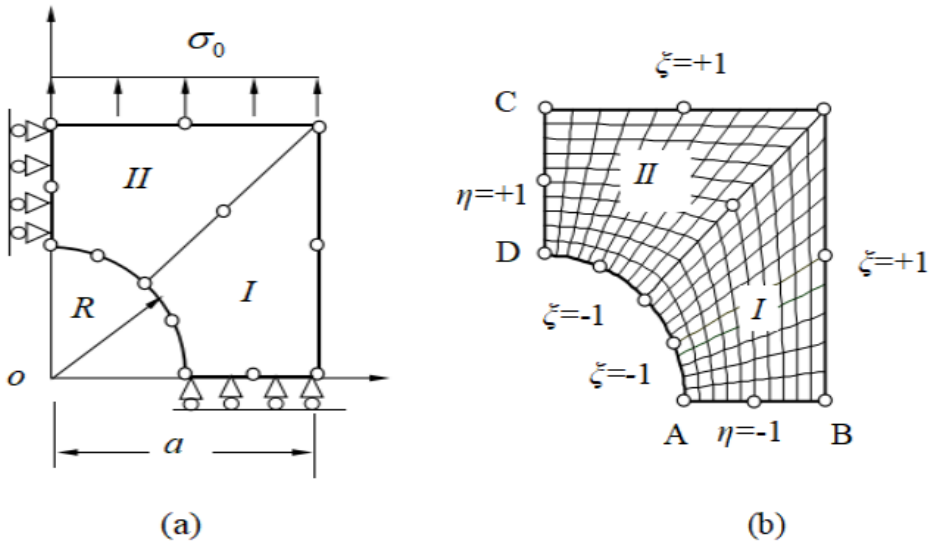

Figure 4.4 Blocks of a quarter square plate and their mapping seeds (a) geometry; (b) distribution of node and two blocks.

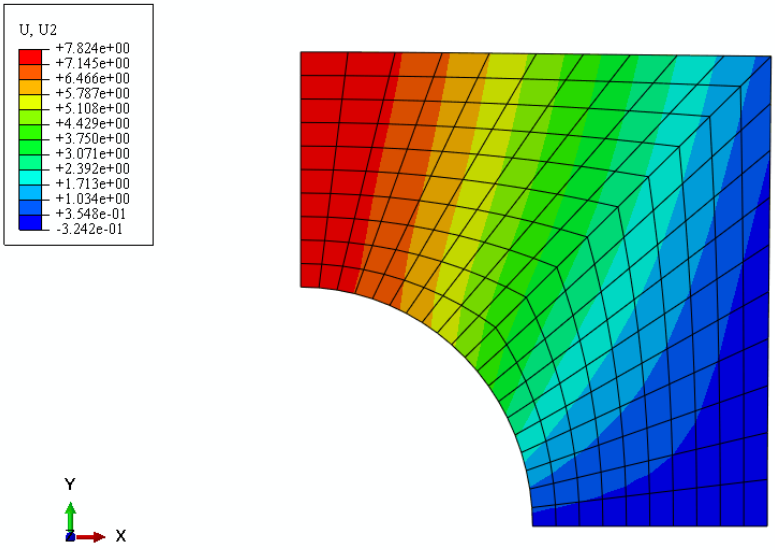

Figure 4.5 The displacement for a plate with central hole in ABAQUS with 200 elements.

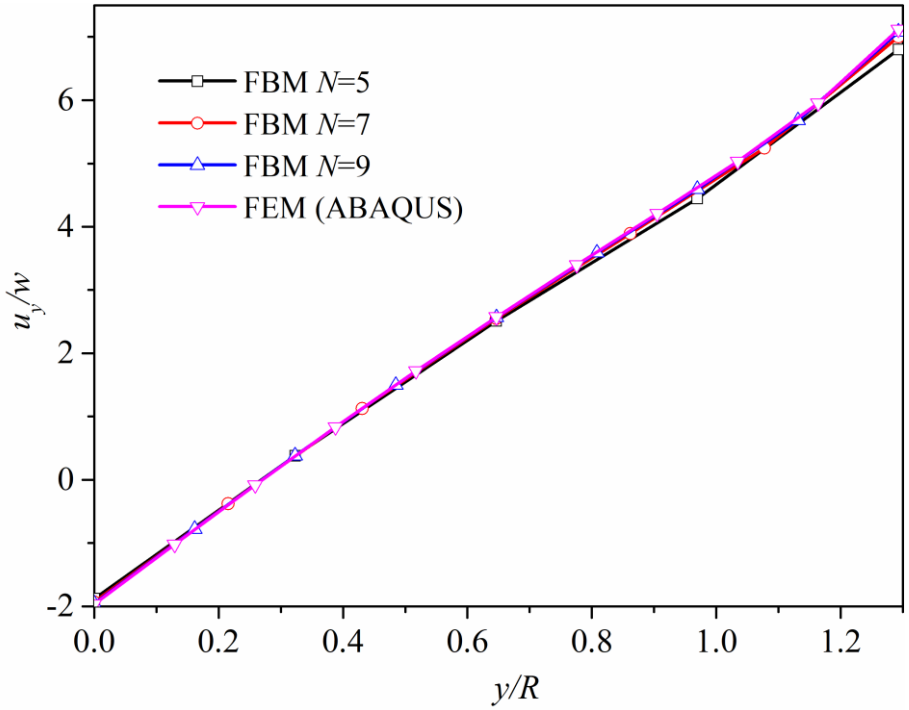

Figure 4.6 The displacement of the connected line for a quarter of the square plate in FGMs.

The displacement for the plate with a central hole under static tensile force (only a quarter of plate is calculated due to the symmetric domain) is illuminated in Figure 4.5 by ABAQUS with 200 elements. A comparison between the result of the Finite Block Method and FEM (ABAQUS) is plotted in Figure 4.6, the number of nodes is chosen as $N = 5,7,9$ respectively for the Finite Block Method. Good agreement has been made as shown in Figure 4.6 when $N \geq 5$. However, there is a small error when it is close to the boundaries for N=5.

C. Example 4.4.3 A rectangular plate with crack in the center under uniform tensile load

Consider a rectangular plate with a crack located in the centre, the property of the material is defined as $E_1 = E_2 = \exp(\alpha x + \beta y)$, $\nu_{12} = \nu_{21} = 0.3$, $w = 2a = 2$ and $h = 1$. The boundary conditions are shown in Figure 4.7. In order to reduce the programming effort, only a quarter of plate is analysed due to the symmetry.

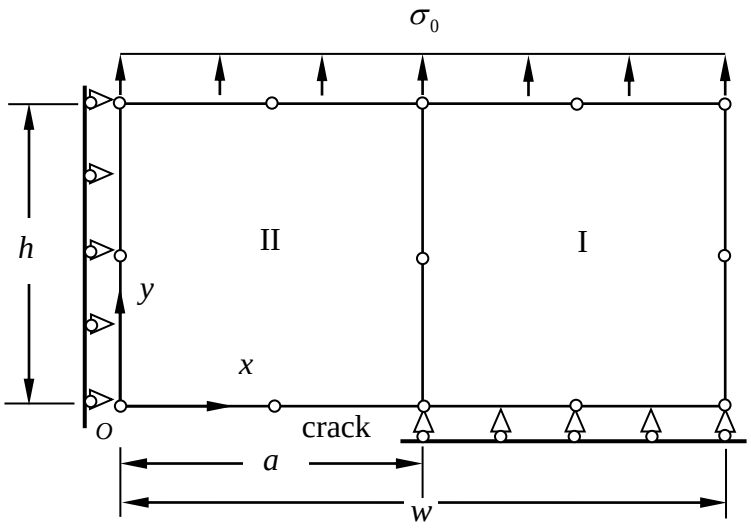

Figure 4.7 A quarter of the plate with a crack in the middle.

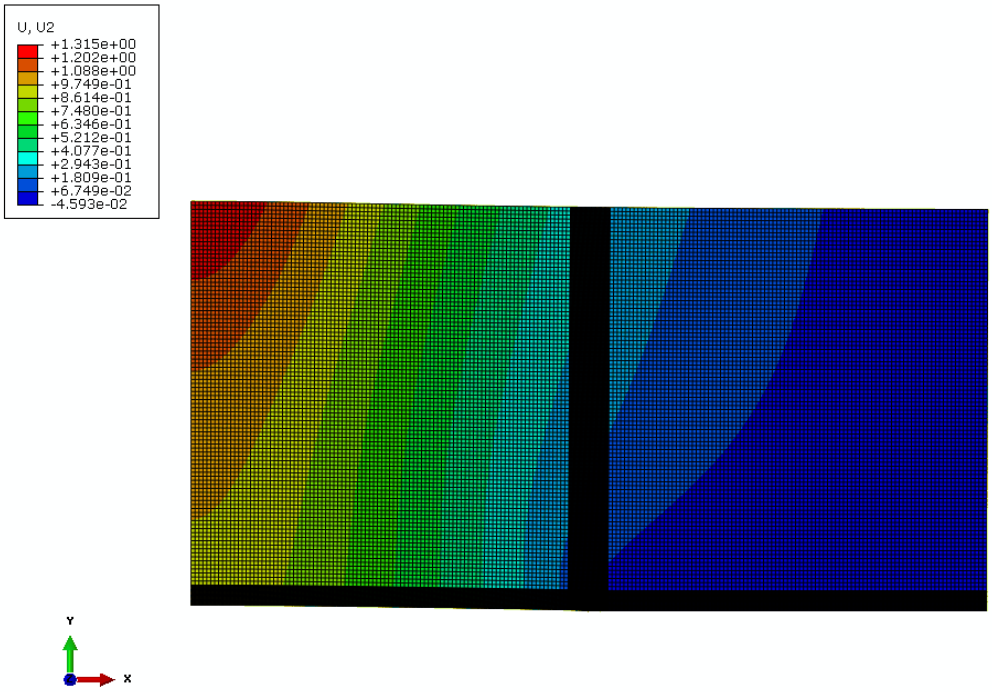

Figure 4.8 The displacement for the central crack in ABAQUS with fine mesh around the crack tip.

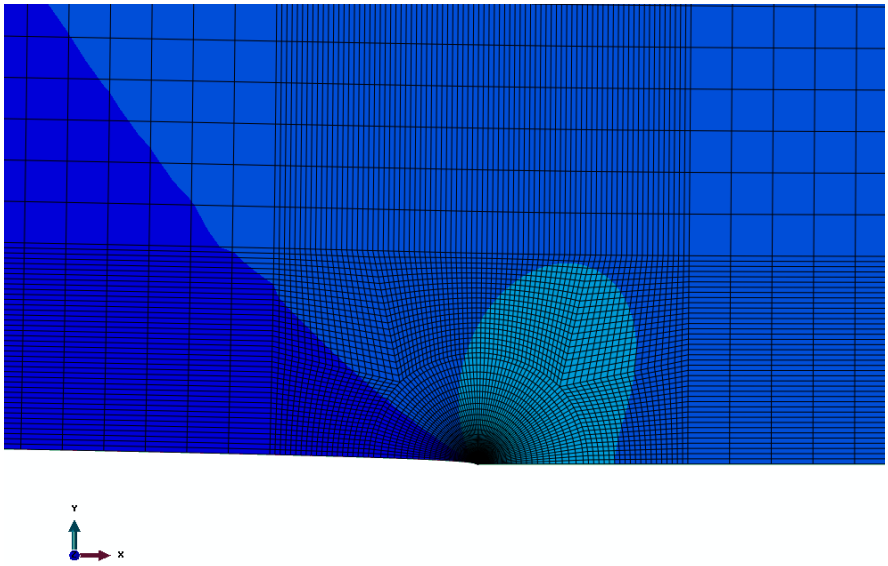

Figure 4.9 Stress distribution near the crack tip with fine mesh.

Table 4.1 Normalized stress intensity factors for different α and β.

α \ β	0		0.2		0.5		1		2	
	FBM	FEM	FBM	FEM	FBM	FEM	FBM	FEM	FBM	FEM
0	1.97	1.98	1.89	1.89	1.79	1.78	1.62	1.60	1.36	1.31
0.2	1.61	1.62	1.55	1.55	1.44	1.45	1.36	1.31	1.03	1.07
0.5	1.18	1.89	1.16	1.14	1.06	1.07	0.95	0.97	0.78	0.79
1	0.72	0.70	0.69	0.68	0.62	0.64	0.56	0.57	0.46	0.47
2	0.26	0.24	0.26	0.23	0.22	0.21	0.19	0.19	0.15	0.16

The normalized stress intensity factor for FGMs is obtained by Eq. (4.18). The number of nodes is $N_1 = N_2 = 11$ and the total number of nodes for two blocks is $M = N_1 \times N_2 = 121$. The result of the displacement for the central crack problems under tensile load by ABAQUS is illuminated in Figure 4.8, and a fine mesh near the crack tip can be observed in Figure 4.9. Instead of the quadratic elements, the triangle elements are adopted for the stress distribution around the crack tip in Figure 4.9. Table 4.1 shows the results of the normalized stress intensity factors $K_1 / \sigma_0 \sqrt{\pi a}$ for different parameters α, β, where the distance $r / a = 0.09549$. It is noticeable that as α and β increase, the values of the normalized stress intensity factors decrease. The reason is the normalized stress intensity factor is inverse proportional to the Young's modulus at the crack tip which can be identified in Eq. (4.18). The results by FEM (ABAQUS) are also given in this table for comparison. The average error related is less than 1% as shown in the table.

D. Example 4.4.4 A plate with an edge crack

An orthotropic FGM plate with an edge crack of length a is considered under tensile uniform load on the top of it. The dimensions and parameters are selected as $a=1, h=2w$, $E_1 = E_1^0 f(x_1), E_2 = E_2^0 f(x_1), G_{12} = G_{12}^0 f(x_1)$, where $f(x_1) = \exp(\alpha x_1 / w)$ and α is dimensionless constant and E_1^0, E_2^0 and G_{12}^0 are elastic modulus at the origin, $\alpha = \ln(p)$, in which E_1^0 and E_1^w are the Young's modulus of the left-hand and right-hand boundaries respectively. Obviously, we assume that the ratios satisfy $E_1^w / E_1^0 = E_2^w / E_2^0 = G_{12}^w / G_{12}^0$. The properties of orthotropic material, E-glass-epoxy, are selected as: $E_1^0 = 45.44$ GPa, $E_2^0 = 12.42$ GPa, $\nu_{12} = 0.227$ and $G_{12}^0 = 5.5$ GPa were adopted by Wen et al [86]. The results by FEM (ABAQUS) are shown in Figure 4.10-4.11. Besides, the normalized displacements along the crack length with varies material properties are plotted in Figure 4.12-4.16 for different geometries. The normalized stress intensity factors between the FBM (the first row) and FEM (the second row) are illustrated in Table 4.2. Good agreements by FBM and FEM are observed in this example.

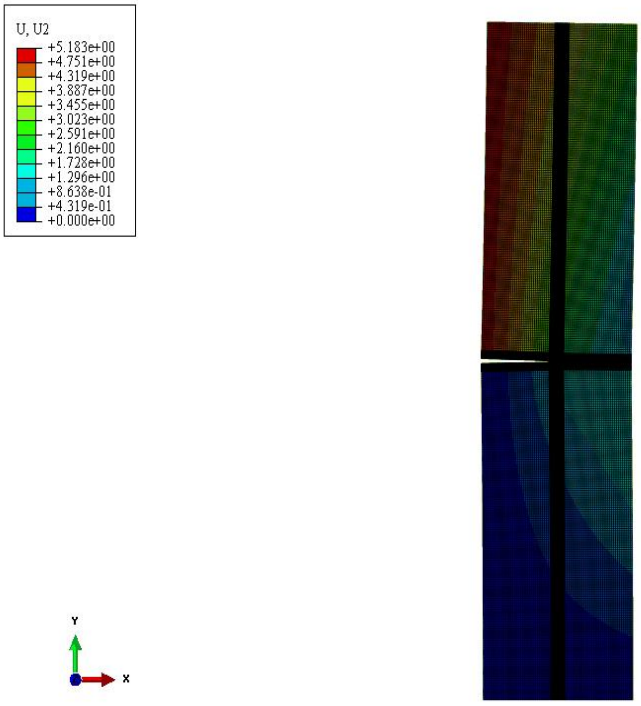

Figure 4.10 The displacement for an edge crack in ABAQUS with fine mesh around the crack tip.

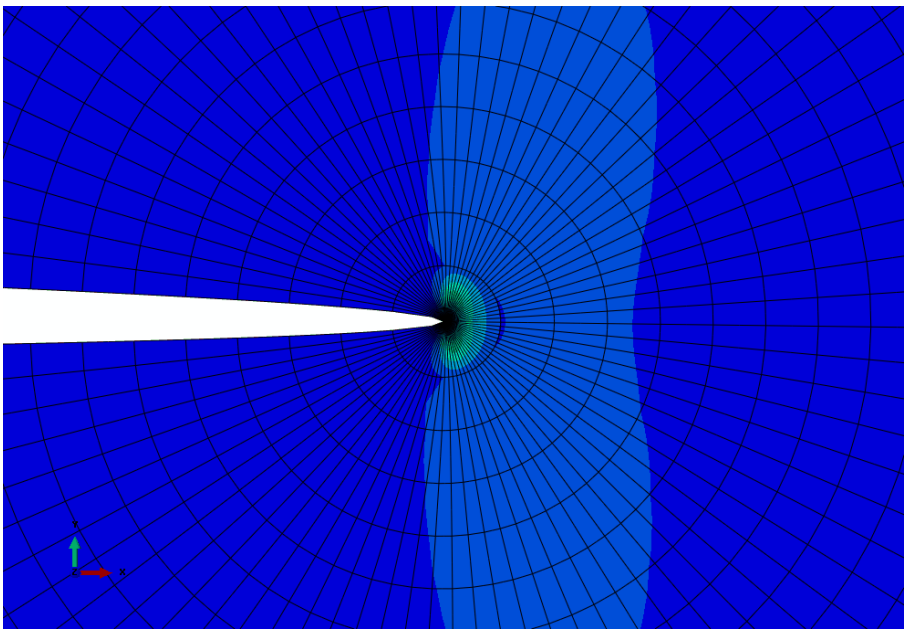

Figure 4.11 Stress distribution near the crack tip with fine mesh.

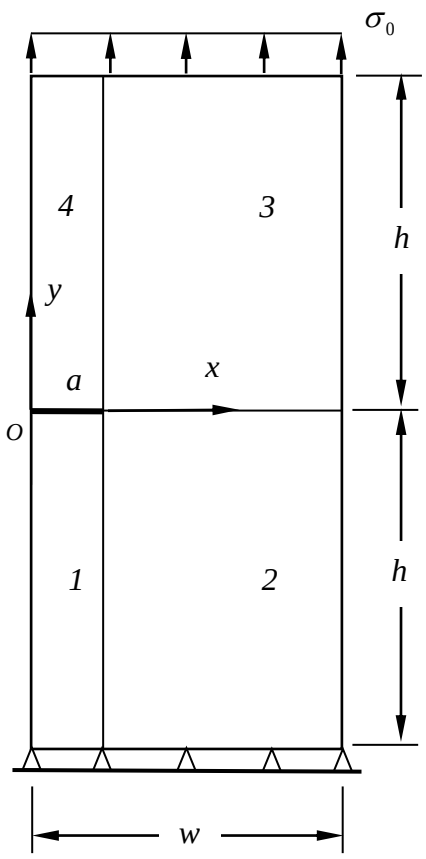

Figure 4.12 A plate with edge crack under tensile loads.

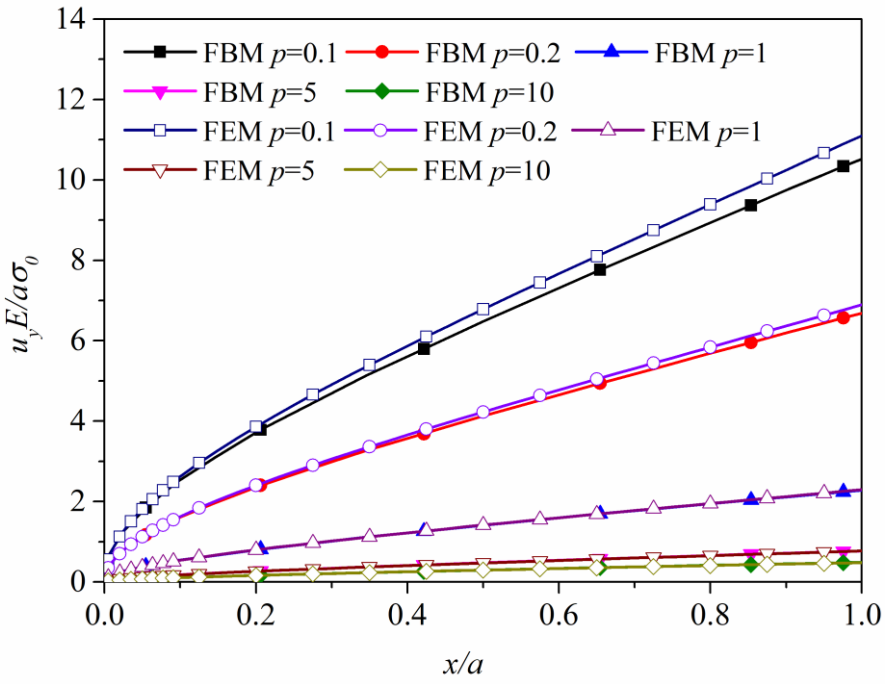

Figure 4.13 Normal crack displacement along the crack length $a/w = 0.6$.

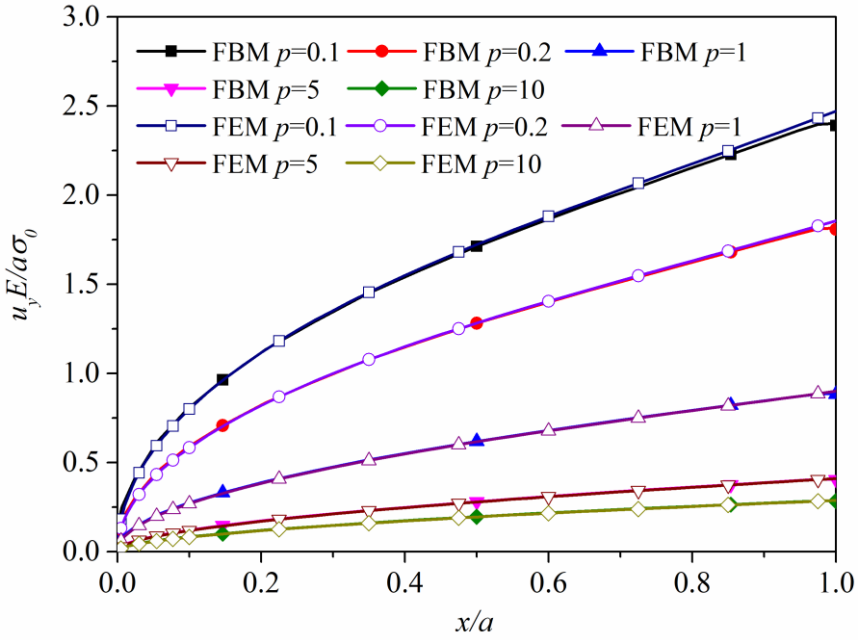

Figure 4.14 Normal crack displacement along the crack length $a/w=0.4$.

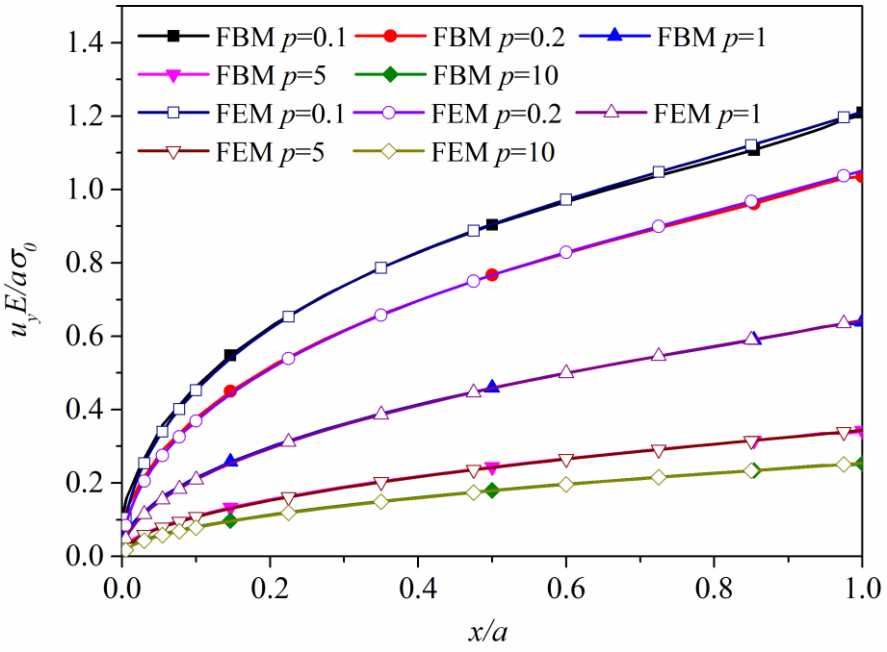

Figure 4.15 Normal crack displacement along the crack length $a/w=0.3$.

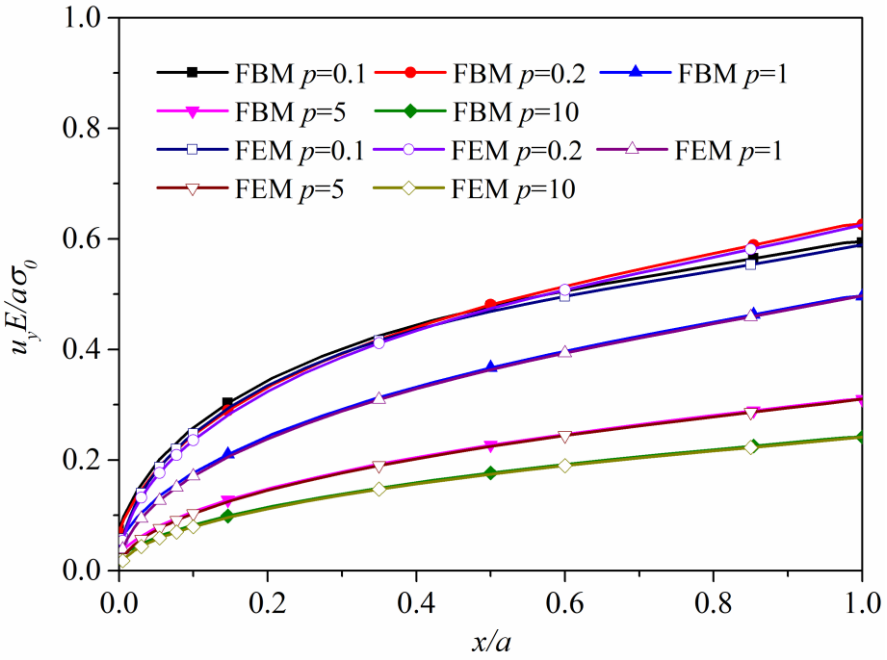

Figure 4.16 Normal crack displacement along the crack length $a/w=0.2$.

Table 4.2 Stress intensity factors for E-glass-epoxy $K_I/\sigma_0\sqrt{\pi a}$.

a/w	$p=0.1$	$p=0.2$	$p=1$	$p=5$	$p=10$
0.2	1.2788	1.3924	1.3840	1.1540	1.0241
	1.2460	1.3524	1.3386	1.1111	0.9838
0.3	1.8165	1.8245	1.6804	1.3997	1.2592
	1.7965	1.7919	1.6344	1.3532	1.2142
0.4	2.5156	2.4305	2.1473	1.7973	1.6392
	2.4790	2.3862	2.0989	1.7535	1.5966
0.6	4.9710	4.7786	4.2333	3.6685	3.4319
	5.1136	4.8199	4.1796	3.5942	3.3566

In this case, the normalized stress intensity factor for various material constants on an orthotropic FGM with edge crack is determined. The results by FEM (ABAQUS) is illuminated in Figure 4.10 for displacement and in Figure 4.11 for stress (near the crack tip). In addition, the fine mesh near the crack tip is observed in Figure 4.11.

The normalized displacement along the crack length for the orthotropic FGMs with various Young's modulus is plotted in Figure 4.12-4.16 with different geometries by both FBM and FEM. Obviously, as the distance to the crack tip increases, the value of the normalized displacement in *y* coordinate is getting larger. However, the derivative of the displacement is decrease, that is because of the stress in *y* direction decrease as the distance to the crack tip is raised. When it comes to the boundary of the physical domain in this case, the stress σ_y become zero. Moreover, as the parameter *p* arises, the Young's modulus increases, result in the normalized stress intensity factor decreasing, which is similar to the example above. In Table 4.2, compare to different geometries we can notice that the ratio of crack length and the width has an effect to the normalized stress intensity factors.

E. Example 4.4.5 A plate with slant edge crack

An isotropic FGM plate of width *w* and height *h* with slant edge crack of length *a* is shown in Figure 4.17 subjected to tensile load on the top with the fixed bottom. The applied force is given as $\sigma_y = \bar{\varepsilon} E_0 \sigma_0 e^{\alpha(x - w/2)}$ and the Young's modulus is defined as $E = E_0 e^{\alpha(x-w/2)}$, where $\bar{\varepsilon}$ is specified strain, E_0 is the Young's modulus at the middle of plate and constant $\alpha = 0.4\sqrt{2}/a$, which is the same as that adopted by Eischen [70]. The Poisson's ratio is chosen as 0.3. The geometry of slant cracked plate is given by

$a/w = 0.4\sqrt{2}$, $h/w = 2$. The normalized SIFs $K_I / \bar{\varepsilon} E_0 \sqrt{\pi a}$ and $K_{II} / \bar{\varepsilon} \quad E_0 \sqrt{\pi a}$ are obtained by both COD and *J*-integral techniques. The radius of integration contour $R/a = 0.2$ in normalized domain and standard integral method for both contour integral and domain integral is applied. Four blocks are used in this modelling shown in Figure 4.17. Table 4.3 shows the comparison of the normalized SIFs with those obtained by Eischen [70] and Kim and Paulino [8]. These results illustrate that the reasonably good agreement with other methods is achieved.

4.5 Evaluation of T-Stress by FBM

4.5.1 Introduction

Fracture performance for both homogeneous and nonhomogeneous materials involving cracks mainly rely on the stress distribution around the crack tip. Numerous researchers [87, 88] have studied the influence of Stress Intensity Factors previously which present the singular stress field at the crack tip. Nevertheless, there is experimental evidence that a stress component parallel to the crack plane may affect fracture mechanics properties, including the direction of crack propagation. Therefore, in the assessment of fracture mechanics, it is necessary to systematically investigate the influence of this constant stress called the *T*-stress.

In 1957, Williams [89] presented a series of formulations to describe the stress distribution around the crack tip. Several researchers [90, 91] discovered that a constant stress component (first higher-order in the expansion of Williams series), which acting parallel to the crack plane, would affect the crack path direction. In 1997, Fett [92] introduced a green's function to determine the two coefficients in the Williams stress

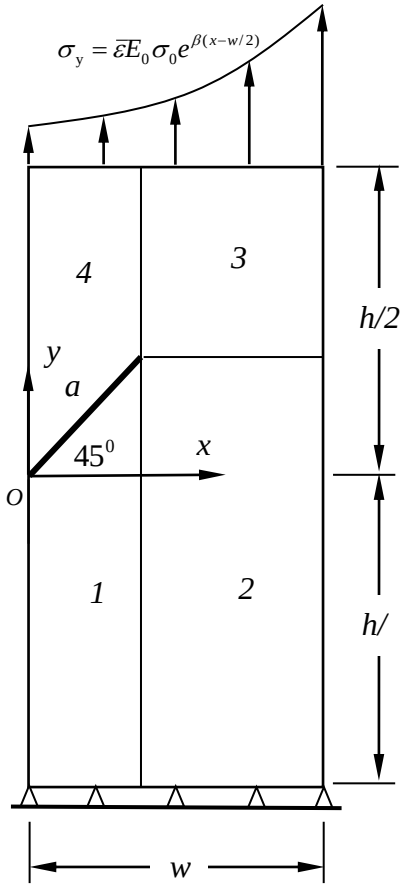

Figure 4.17 Geometry of a slanted edge crack in a plate.

Table 4.3 Normalized SIFs for FGM slant cracked plate.

a	$K_I / \bar{\varepsilon} E_0 \sqrt{\pi a}$				$K_{II} / \bar{\varepsilon} E_0 \sqrt{\pi a}$			
	COD	*J*-int	Kim	Eishen	COD	*J*-int	Kim	Eishen
0.00	1.5014	1.4476	1.451	1.438	0.6201	0.5978	0.604	0.605
0.10	1.4434	1.3923	1.396	NA	0.5949	0.5737	0.579	NA
0.25	1.3613	1.3139	1.316	NA	0.5594	0.5398	0.544	NA
0.50	1.2364	1.1945	1.196	NA	0.5056	0.4882	0.491	NA
0.75	1.1250	1.0877	1.089	NA	0.4579	0.4424	0.443	NA
1.00	1.0254	0.9921	0.993	0.984	0.4155	0.4017	0.402	0.395

function for the basis of tensile and bending loading cases with the Boundary Collocation Method. The next year, Fett [93] applied this method to rectangular plates and circular disks for the evaluation of *T*-stresses subjected to any traction distribution at the boundaries. In addition, various length-to-width ratios for rectangular plates with an edge crack were discussed. Besides, the SIFs and *T*-stress for a double-edge-cracked circular disks were presented by Fett[94] with mixed boundary conditions in 2002.

By the application of the path independent M-integral, Sladek [95] computed the *T*-stress for interface cracks between two dissimilar elastic materials by the sub-region Boundary Element Method. Also, in 1997, Sladek [96] improved the M-integral for a dynamic *T*-stress in a two dimension region with a stationary crack. The results for a single crack in a finite plate and two cracks in an infinite sheet were obtained by the boundary element method. Moreover, in 2016, Sladek [97] proposed a quarter-point crack tip element to calculate the *T*-stress for the fracture analysis of orthotropic FGMs subjected to thermal and impact mechanical load by the FEM method. By the simplification of a formula derived from the variation of the displacement in this particular element ahead of the crack, this approach was of the advantage in determining the *T*-stress without an additional contour-domain.

In this section, the Finite Block Method is applied with the combination of the Williams' series which describe the stress and displacement fields at a circular core around the crack tip to evaluate the SIFs and *T*-stress. A circular disk with one edge crack is presented with the proper boundary conditions and connection conditions at the interface between the blocks and the singular core around the crack tip. For the accuracy of the FBM method, the results given by Fett [98] are considered as benchmark.

4.5.2 Williams Series of Stress Function

In order to obtain dimensionless coefficients, it is of advantage to normalize the crack-tip distance on the characteristic length w. For a cracked body, the general solutions in a series representation for Airy stress function given by Williams [89] for symmetric type

$$\begin{aligned}\Phi &= \sigma_0 w^2 \sum_{n=1}^{\infty} (r/w)^{n+1/2} A_n \left[\cos(n+\frac{1}{2})\theta - \frac{n+1/2}{n-3/2}\cos(n-\frac{3}{2})\theta \right] \\ &+ \sigma_0 w^2 \sum_{n=1}^{\infty} (r/w)^{n+1} B_n \left[\cos(n+1)\theta - \cos(n-1)\theta\right], \quad r \le r_0, 0 \le \theta \le \pi,\end{aligned} \tag{4.19}$$

where σ_0 is the characteristic stress such as a uniformly distributed load on the boundary, r_0 is radius of the circular core centered at crack tip ($r_0 / w << 1$) and A_n, B_n are dimensionless coefficients. The components of stress in the circular core are given by

$$\begin{aligned}\sigma_\theta^c &= \sigma_0 \sum_{n=1}^{\infty} (r/w)^{n-3/2} (n+1/2)(n-1/2) A_n \left[\cos(n+\frac{1}{2})\theta - \frac{n+1/2}{n-3/2}\cos(n-\frac{3}{2})\theta \right] \\ &+ \sigma_0 \sum_{n=1}^{\infty} (r/w)^{n-1} (n+1) n B_n \left[\cos(n+1)\theta - \cos(n-1)\theta\right], \\ \sigma_r^c &= \sigma_0 \sum_{n=1}^{\infty} (r/w)^{n-3/2} (n+1/2) A_n \left[\frac{n^2 - 4n + 7/4}{n-3/2}\cos(n-3/2)\theta - (n-1/2)\cos(n+1/2)\theta \right] \\ &+ \sigma_0 \sum_{n=1}^{\infty} (r/w)^{n-1} B_n \left[(n-3)\cos(n-1)\theta - (n+1)\cos(n+1)\theta\right], \quad r \le r_0 \\ \tau_{r\theta}^c &= \sigma_0 \sum_{n=1}^{\infty} (r/w)^{n-3/2} (n+1/2)(n-1/2) A_n \left[\sin(n+1/2)\theta - \sin(n-3/2)\theta\right] \\ &+ \sigma_0 \sum_{n=1}^{\infty} (r/w)^{n-1} n B_n \left[(n+1)\sin(n+1)\theta - (n-1)\sin(n-1)\theta\right]\end{aligned} \tag{4.20}$$

and the displacement field are given below

$$u_r^c = \frac{(1+\nu)\sigma_0 w}{E}\sum_{n=1}^{\infty}(r/w)^{n-1/2}\frac{2n+1}{2n-3}A_n\left[(n+4\nu-7/2)\cos(n-\frac{3}{2})\theta-(n-3/2)\cos(n+\frac{1}{2})\theta\right]$$
$$+\frac{(1+\nu)\sigma_0 w}{E}\sum_{n=1}^{\infty}(r/w)^{n}B_n\left[(n+4\nu-3)\cos(n-1)\theta-(n+1)\cos(n+1)\theta\right]+U_0\cos\theta,$$
$$u_\theta^c = \frac{(1+\nu)\sigma_0 w}{E}\sum_{n=1}^{\infty}(r/w)^{n-1/2}\frac{2n+1}{2n-3}A_n\left[(n-3/2)\sin(n+\frac{1}{2})\theta-(n-4\nu+5/2)\sin(n-\frac{3}{2})\theta\right]$$
$$+\frac{(1+\nu)\sigma_0 w}{E}\sum_{n=1}^{\infty}(r/w)^{n}B_n\left[(n+1)\sin(n+1)\theta-(n-4\nu+3)\sin(n-1)\theta\right]-U_0\sin\theta \tag{4.21}$$

where U_0 is the horizontal displacement at crack tip ($r=0$). In terms of the coefficients A_n and B_n, the stress intensity factor and *T*-stress are obtained by

$$K_I = \sigma_0\sqrt{18\pi a}A_1 \quad \text{and} \quad T=-4\sigma_0 B_1. \tag{4.22}$$

For a simple case, one block is sufficient in the numerical procedure shown in Figure 4.19(a). In the Williams series of stress and displacement in Eq. (4.20) and Eq. (4.21), a finite term with truncation number $\bar{n}$ is considered. On the interface between the block and circular core $(r=r_0, 0\le\theta\le\pi)$, suppose that there are *N* collocation points and four connection equations

$$u_r(r_0,\theta)=u_r^c(r_0,\theta),\ u_\theta(r_0,\theta)=u_\theta^c(r_0,\theta),$$
$$\sigma_r(r_0,\theta)=\sigma_r^c(r_0,\theta),\ \tau_{r\theta}(r_0,\theta)=\tau_{r\theta}^c(r_0,\theta),\ \theta=\theta_i,\ i=1,2,...N \tag{4.23}$$

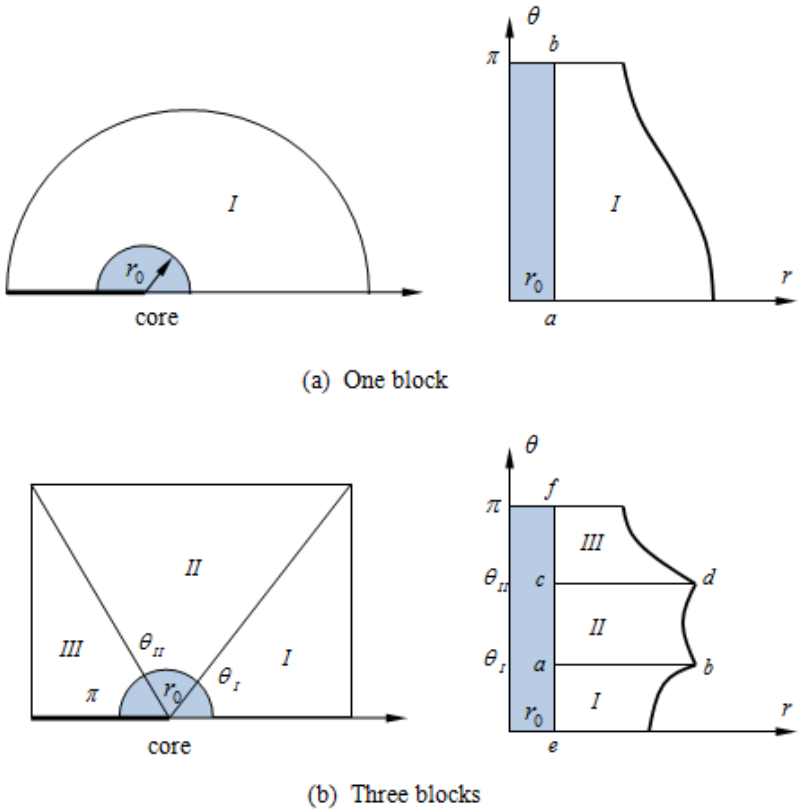

Figure 4.18 Finite blocks and circular core centered at crack tip of radius r_0 in polar coordinate.

If the number of truncation terms is chosen as $\bar{n} = N$, we have $2T + 2\bar{n}$ linear algebraic equations in total to determine displacements $(u_{ri}, u_{\theta i})$, $i = 1,2,...,T$, and coefficients $(A_n, B_n), n = 1,2,...,\bar{n}$. However, in the Williams series, the last term of truncation $B_{\bar{n}}$ should be removed if the horizontal motion at the crack tip U_0 is considered. Therefore, the unknowns in the Williams series are (A_n, B_n), $n = 1,2,...,\bar{n}-1$, $A_{\bar{n}}$ and U_0. In the case with more than one block as shown in Figure 4.18(b), there are interface with connection conditions. Therefore, the number of connection equations at the collocation points on the interface between the blocks and circular core is $N_{\mathrm{I}} + N_{\mathrm{II}} + N_{\mathrm{III}} - 2$. Then the number of truncation is chosen as

$\bar{n} = N_I + N_{II} + N_{III} - 2$ in order to determine the same number of coefficients in the Williams series.

4.5.3 Numerical Examples

A. An edge-cracked circular disk under uniform traction for one material

Firstly, consider an edge-cracked circular disk loaded by constant normal traction σ_0 along the circumference shown in Figure 4.19. Due to symmetry about horizontal axis, only half of disk is calculated with the boundary conditions

$$\begin{aligned} &\tau_{r\theta} = u_\theta = 0, && \theta = 0,\ 0 < r \le R, \\ &u_r = 0, && \theta = 0,\ r = R. \end{aligned} \tag{4.24a}$$

$$\begin{aligned} &\sigma_r = \sigma_0, \tau_{r\theta} = 0, && 0 \le \theta \le \pi,\ r = R, \\ &\tau_{r\theta} = \sigma_\theta = 0, && \theta = \pi,\ 0 < r \le R. \end{aligned} \tag{4.24b}$$

Suppose that the crack tip is located at the centre of the disk and crack length $a = R$. The number of collocation point along the interface is *N* and then the number of truncation terms should be $\bar{n} = N$ with characteristic length $w(= D = 2R)$. Again, the last term $B_{\bar{n}}$ should be removed in order to consider the motion U_0 at crack tip in Eq. (4.21). The disk is centerred at the crack tip and one block with 8 seeds is enough to for the mapping of the geometry precisely as shown in Figure 4.19 and the number of seed is selected as $M = N$ for convenience. Table 4.4 and Table 4.5 show the numerical results of the stress intensity factor and *T*-stress against the number of seed N when $r_0 / R = 0.2$ and the radius of Williams core zone r_0 / R when $N = 15$. The results given by Fett [98] are considered as benchmark, which are $K_I^0 = 3.1716\sigma_0\sqrt{\pi a}$ and

$T^0 = 1.896\sigma_0$ respectively. It is evident that high accurate solutions can be obtained in the region of $N \geq 9$ and $0.1 \leq r_0 / R \leq 0.3$.

Table 4.4 Normalized stress intensity factor and *T*-stress versus the number of seed.

N	$K_I / \sigma_0 \sqrt{\pi a}$	$\left\|K_I - K_I^0\right\| / K_I^0 (\%)$	T / σ_0	$\left\|T - T^0\right\| / T^0 (\%)$
9	3.1800	0.266	1.9259	1.578
11	3.1751	0.110	1.9042	0.433
13	3.1738	0.071	1.8993	0.171
15	3.1735	0.059	1.8981	0.109

Table 4.5 Normalized stress intensity factor and *T*-stress versus the ratio r_0 / a.

r_0 / a	$K_I / \sigma_0 \sqrt{\pi a}$	$\left\|K_I - K_I^0\right\| / K_I^0 (\%)$	T / σ_0	$\left\|T - T^0\right\| / T^0 (\%)$
0.10	3.1794	0.247	1.9171	1.112
0.15	3.1741	0.079	1.9000	0.213
0.20	3.1735	0.059	1.8981	0.109
0.25	3.1732	0.051	1.8982	0.116
0.30	3.1681	0.078	1.9004	0.233

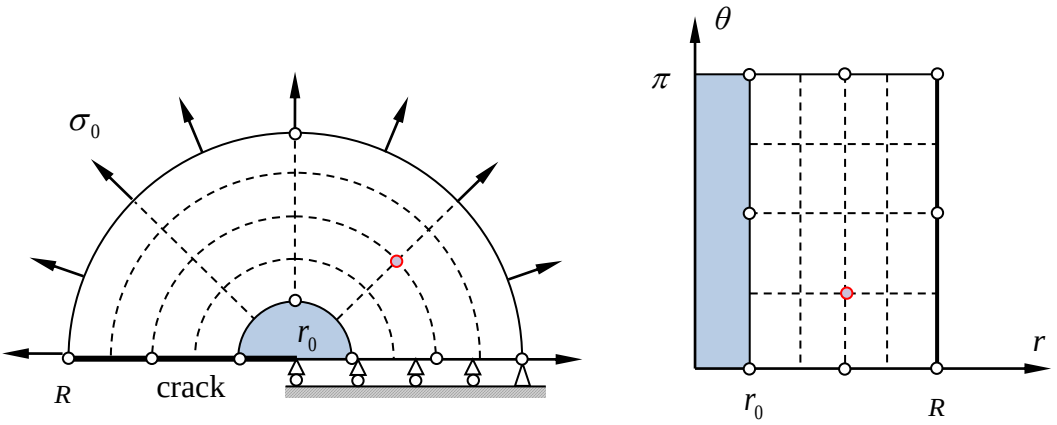

Figure 4.19 Half disk with crack and distribution of collocation points: (a) cracked disk under tensile load; (b) mapping of geometry with 8 seeds and collocation points.

B. An edge-cracked circular disk under uniform traction for two materials

Secondly, consider a cracked circular disk bounded with an outer ring with different material loaded by constant normal traction σ_0 along the circumference shown in Figure 4.20. Comparing with the first example above, one more block is added with one more interface between block I and block II. The number of collocation points in total is $Q = M_I N_I + M_{II} N_{II}$ and the number of truncation terms in Williams series is chosen as $\bar{n} = N_I$ and width of component in Williams series $w = 2R_0$. Continuous of displacements and stresses along the interface of blocks I and II have to be satisfied. Same as the first case, the quadratic block with 8 seeds is employed. In the computation,

the parameters are selected as $r_0 / R_0 = 0.2$, $M_{\mathrm{I}} = M_{\mathrm{II}} = 17$, $N_{\mathrm{I}} = N_{\mathrm{II}} = 9$ and $\nu_{\mathrm{I}} = \nu_{\mathrm{II}} = 0.3$. The numerical results of the stress intensity factor and *T*-stress against the ratio of Young's module E_{II} / E_I and ratio R_1 / R_0 are shown in Figure 4.21 (a) and (b).

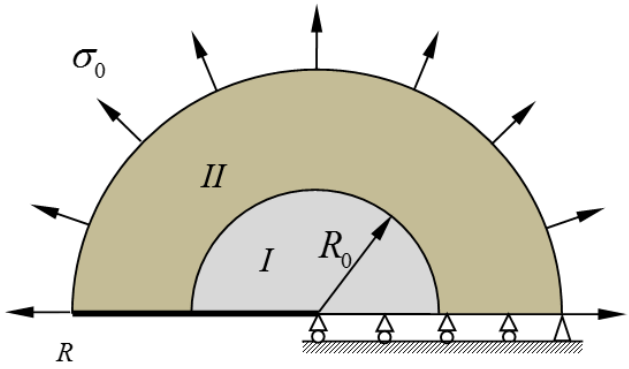

Figure 4.20 Half cracked disk (I) bounded with a ring (II) under tensile load.

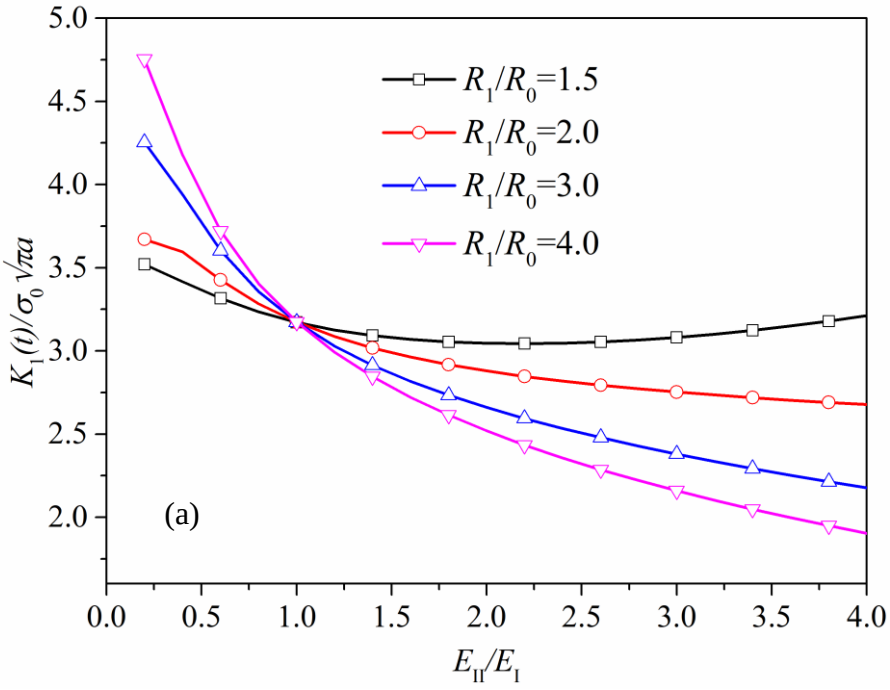

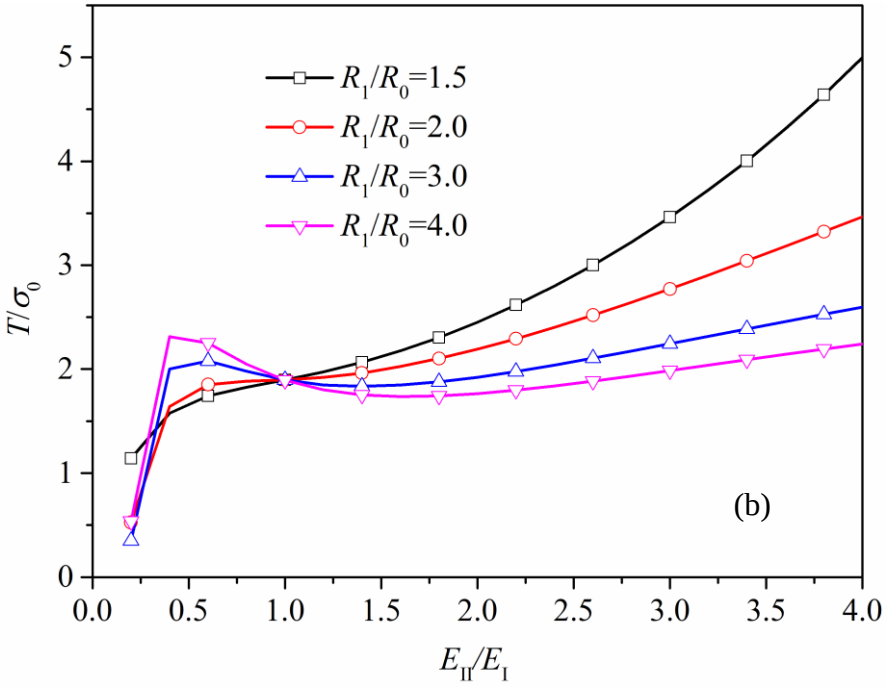

Figure 4.21 (a). Normalized Stress intensity factors, and (b). Normalized *T*-stress for a circular disk with different materials.

The normalized stress intensity factors and *T*-stress are plotted in Figure 4.21 with different ratio R_1/R_0. It is noticeable that as the ratio of E_{II}/E_I goes higher, the normalized stress intensity factors decreases. Additionally, when $E_{II}/E_I<1$, the case of $R_1/R_0=4$ has the largest value while when $E_{II}/E_I>1$, the result of ratio $R_1/R_0=1.5$ is the top of the others. However, as for the result of normalized *T*-stress, it is much more complex as the ratio R_1/R_0 increases.

4.6 Conclusion

In the first part of this chapter, the Finite Block Method is presented for numerical analysis of general linear elastic crack problems for both isotropic and anisotropic

Functionally Graded Materials. The formulation in strong form for static elastic analysis of Functionally Graded Materials is solved by the Finite Block Method. The Stress Intensity Factors are calculated by Crack Opening Displacement for orthotropic FGMs. Several numerical examples are computed for static analysis of crack problems in two dimensions. In order to confirm the accuracy of the Finite Block Method, the results in FEM (ABAQUS) are adopted for comparison. The essential features of the Finite Block Method when applied to crack problems on FGMs can be summarized as:

1) The physical domain is divided into two or more blocks which can be defined by eight seeds for two dimensional problems. The coefficient differential matrix can be derived directly from the Lagrange Interpolation Method by each block.
2) This method considered the governing equations in strong form and is of all advantages of meshless methods. As the order of the partial differentials is evaluated by Lagrange series in the mapping domain, the computational effort is reduced significantly.
3) This method can be extended to any types of partial differential equations, including dynamic problems etc. Besides, this method can be combined with other Meshless Method or Boundary Element Method for practical problems.

Secondly, the FBM was applied to evaluate *T*-stress in conjunction with Williams' stress function for fracture problems. A circular core was presented for the stress and displacement field around the crack tip. For the reason of convenience, the number of node along the boundary of the circular core is chosen to be the same as the number of the truncation in Williams' stress function. By the examples computed above, it is noticeable that the SIFs and *T*-stress can be attained with high accuracy. In addition, this

method can be extended to dynamic analysis of the SIFs and *T*-stress without any difficulties.

Chapter 5

Finite Block Method for Functionally Graded Materials: Dynamics

5.1 Dynamic Analysis of FGM

5.1.1 Introduction

The static analysis of crack problems for Functionally Graded Materials was introduced theoretically in Chapter 4. As for static problems, the displacement, strain and stress are variables related to the spatial coordinate. However, in dynamic problems, an inertial force is considered for the equilibrium equations so that all these variables are time dependent. Therefore, it is of the essence for the accurate analysis on the behaviors of Functionally Graded Materials subjected to dynamic loading due to its advantage of continuously change in material properties through a direction.

In 2002, Wu [99] proposed an extended dynamic *J* integral for the assessment of both stationary and dynamic crack problems on FGMs. In his work, the FEM is adopted in combination with element-free Galerkin method to construct the shape functions and test functions for an edge-cracked panel. The numerical results indicated the efficiency and accuracy of this characteristic factor. In 2006, Song [100] developed the M integral based on the non-equilibrium equations. This was for the analysis of both static and dynamic crack problems in FGMs by taking into account the non-homogeneous

property. In conjunction with FEM, the mode I and mixed mode DSIFs can be obtained directly using the M integral. This can be verified using benchmark problems.

In 2000, an Extended Finite Element Method (XFEM) was introduced for three dimensional crack simulations by Sukuma [101]. A discontinuous formulation was utilized to describe the interior of the crack surface in order to reduce the difficulty in mesh generation around the crack region. By the study of the numerical results, this method was considered to be superior to classic FEM in complex structural components subjected to crack problems. In 2010, Motamedi and Mohammadi [102] extended this XFEM to dynamic analysis of crack problems in orthotropic media. The characteristic parameters to evaluate the fracture mechanics of orthotropic FGMs, namely mixed-mode SIFs can be attained by dynamic J integral.

In 1995, Fedelinski and Aliabadi [103] developed a time domain BEM to compute dynamic fracture problems for isotropic materials. A series of boundary integral equations were constructed by applying the displacement equations and the stress equations to two crack surfaces respectively. Numerical examples, including central crack, slant crack and multi-cracks in a plate were presented to check the accuracy and time consuming of this method. In 2002, the BEM was introduced by Albuquerque and Aliabadi [104] to solve the dynamic crack problems related to orthotropic FGMs. A multi-domain boundary element formulation was applied with the assistance of traction singular quarter point elements which were used for a correct description of displacement and stress distribution around the crack tip for the calculation of the dynamic SIFs. The results indicated that the dynamic SIFs were strongly dependent on the material gradients. Moreover, in 2003 Zhang improved a hyper-singular time-domain traction boundary integral equation method for dynamic crack analysis on

linear elastic FGMs. A convolution quadrature formula is adopted to solve the time-domain traction BIE, while a Galerkin method is used for the spatial related variables.

In 1995, Element-free Galerkin (EFG) Methods were developed for the analysis of both static and dynamic problems based on MLS interpolations by Belytschko [105]. Compare with the FEM, no mesh is generated in this method. For static problems, Element-free Galerkin Method is demonstrated to be a very promising approach with complex structural components. However, there are shortcomings for this method in dynamic analysis including the errors which occur as a result of changes in the dependent variables due to the movement of nodes. In addition, Sladek [106] introduced a contour integral method for transient dynamic analysis in non-homogeneous materials. The local Petrov-Galerkin method was presented for the calculation of physical fields, while the MLS interpolation was adopted for the physical variables in the LBIEs.

In this chapter, the basic concepts for dynamic analysis in FGMs are presented, and also the formula of FGMs by the FBM is proposed. Furthermore, the Laplace transform is utilized to deal with the variables dependent on time. Additionally, the dynamic stress intensity factors are evaluated by crack opening displacement (COD) technique for both isotropic and orthotropic FGMs. Finally, several examples about elastic materials and functional graded materials in 2D problems are given to demonstrate the convergence and accuracy of finite block method in dealing with dynamic problems.

5.1.2 Formula of Dynamic Problems on FGMs by FBM

Assume 2D elasticity of domain Ω with boundary Γ in functionally graded materials. It is assumed that the properties of materials are dependent on the spatial coordinate and all material coefficients vary along the geometry in FGMs. The

equilibrium equations are shown as Eq. (5.1), where the stress and strain relationship are the same as Eq. (4.3).

$$\begin{aligned} &\frac{\partial \sigma_x}{\partial x}+\frac{\partial \tau_{xy}}{\partial y}+b_x=\rho\frac{\partial^2 u_x}{\partial t^2}, \\ &\frac{\partial \tau_{xy}}{\partial x}+\frac{\partial \sigma_y}{\partial y}+b_y=\rho\frac{\partial^2 u_y}{\partial t^2}, \end{aligned} \qquad (x,y)\in\Omega \tag{5.1}$$

where $\sigma_x, \sigma_y, \tau_{xy}$ are stresses in different direction, u_x, u_y are the displacements in x and y axis respectively. Here b_x and b_y are the body forces, ρ indicates the mass density of the media, $\partial^2 u_x/\partial t^2, \partial^2 u_y/\partial t^2$ are accelerations along x and y axis respectively. Eq. (5.1) can be transformed to the Laplace domain with initial conditions as follows

$$\begin{aligned} &\frac{\partial \tilde{\sigma}_x}{\partial x}+\frac{\partial \tilde{\tau}_{xy}}{\partial y}+\tilde{b}_x=\rho(s^2\tilde{u}_x-sV_x-U_x), \\ &\frac{\partial \tilde{\tau}_{xy}}{\partial x}+\frac{\partial \tilde{\sigma}_y}{\partial y}+\tilde{b}_y=\rho(s^2\tilde{u}_y-sV_y-U_y), \end{aligned} \qquad (x,y)\in\Omega \tag{5.2}$$

in which, initial conditions are given as

$$\begin{aligned} &\frac{\partial u_x((x,y),0)}{\partial t}=V_x(x,y) \quad \text{and} \quad u_x((x,y),0)=U_x(x,y), \\ &\frac{\partial u_y((x,y),0)}{\partial t}=V_y(x,y) \quad \text{and} \quad u_y((x,y),0)=U_y(x,y), \end{aligned} \qquad (x,y)\in\Omega \tag{5.3}$$

and the Laplace transformation is defined as

$$\tilde{f}(s)=\int_0^\infty f(t)e^{-st}dt \tag{5.4}$$

where s is Laplace transform parameter. By applying the boundary conditions, one obtains

$$\begin{aligned} &\tilde{u}_x((x,y),s)=\tilde{u}_x^0((x,y),s),\ \tilde{u}_y((x,y),s)=\tilde{u}_y^0((x,y),s), \qquad (x,y)\in\Gamma_u \\ &\tilde{\sigma}_{xx}n_x+\tilde{\tau}_{xy}n_y=\tilde{t}_x^{\,0}((x,y),s),\ \tilde{\tau}_{xy}n_x+\tilde{\sigma}_{yy}n_y=\tilde{t}_y^{\,0}((x,y),s) \qquad (x,y)\in\Gamma_\sigma \end{aligned} \tag{5.5}$$

where $\tilde{u}_\alpha^0$ and $\tilde{t}_\alpha^{\,0}$ indicate the transformed boundary displacements and traction on Γ_u and Γ_σ. By applying the FBM, the equilibrium equation in Eq. (5.2) results in a matrix form as

$$\begin{aligned} &\left(\mathbf{D}_x\mathbf{Q}_{11}\mathbf{D}_x+\mathbf{D}_y\mathbf{Q}_{66}\mathbf{D}_y\right)\tilde{\mathbf{u}}_x+\left(\mathbf{D}_x\mathbf{Q}_{12}\mathbf{D}_y+\mathbf{D}_y\mathbf{Q}_{66}\mathbf{D}_x\right)\tilde{\mathbf{u}}_y+\tilde{\mathbf{b}}_x \\ &=\rho\left(s^2\tilde{\mathbf{u}}_x-s\mathbf{V}_x+\mathbf{U}_x\right), \\ &\left(\mathbf{D}_y\mathbf{Q}_{12}\mathbf{D}_x+\mathbf{D}_x\mathbf{Q}_{66}\mathbf{D}_y\right)\tilde{\mathbf{u}}_x+\left(\mathbf{D}_x\mathbf{Q}_{66}\mathbf{D}_x+\mathbf{D}_y\mathbf{Q}_{22}\mathbf{D}_y\right)\tilde{\mathbf{u}}_y+\tilde{\mathbf{b}}_y \\ &=\rho\left(s^2\tilde{\mathbf{u}}_y-s\mathbf{V}_y+\mathbf{U}_y\right) \end{aligned} \tag{5.6}$$

where $\mathbf{D}_x,\mathbf{D}_y$ are the differential matrix by FBM, $\tilde{\mathbf{u}}_x,\tilde{\mathbf{u}}_y$ are the vectors of nodal displacement in Laplace domain, $\tilde{\mathbf{b}}_x,\tilde{\mathbf{b}}_y$ are the vectors of nodal body force in Laplace domain. Again, there are $2M(=2N_1\times N_2)$ linear algebraic equations in total from Eq. (5.6) and Eq. (5.5) for the boundary conditions of each block. By solving a set of linear algebraic equations, all nodal values of displacements can be determined. In the case of two and more blocks, the connection conditions of displacements and traction on the interface $\Gamma_{\text{int}}^{(I,II)}$ between blocks I and II yield

$$\begin{aligned} &\tilde{\mathbf{u}}_x^I((x,y),s)=\tilde{\mathbf{u}}_x^{II}((x,y),s),\ \tilde{t}_x^{\,I}((x,y),s)+\tilde{t}_x^{\,II}((x,y),s)=0, \\ &\tilde{\mathbf{u}}_y^I((x,y),s)=\tilde{\mathbf{u}}_y^{II}((x,y),s),\ \tilde{t}_y^{\,I}((x,y),s)+\tilde{t}_y^{\,II}((x,y),s)=0 \end{aligned} \qquad (x,y)\in\Gamma_{\text{int}}^{(I,II)} \tag{5.7}$$

In the case of two blocks, the number of node in total is $2M(=2M_I+2M_{II})$, which is the same equation number from the equilibrium equations in the domain Ω, boundary conditions and connection conditions.

Select $(L+1)$ samples in the transformation space $s_l, l = 0,1,...,L$ for transformed values. Then the displacements in the time domain can be obtained by the inversion technique. A simple and accurate inverse method proposed by Durbin [107] is adopted as follows

$$f(t) = \frac{2e^{\eta t}}{T_0}\left[-\frac{1}{2}\tilde{f}(\eta) + \sum_{l=0}^{L} \mathrm{Re}\left\{\tilde{f}\left(\eta + 2\pi i k / T_0\right) e^{2\pi i l / T_0}\right\}\right], \tag{5.8}$$

where $\tilde{f}(s_l)$ denotes the transformed variable in the Laplace domain. The transformation parameter is chosen as $s_l = (\eta + 2\pi ik)/T_0\ (i = \sqrt{-1})$. Therefore, there are two free parameters in s_l, i.e. η and T_0 which depend on the observing period in the time domain. In the following examples, all variables are normalized with unit dimensions for the convenience of the analysis, i.e. $T_0 / t_0 = 20, \eta = 5$, where t_0 is time for a specified elastic wave.

5.1.3 Dynamic Stress Intensity Factor of FGMs

The static problems for stress intensity factor of FGMs have been introduced systematically in chapter 4. For dynamic problems, the mixed mode stress intensity factors are determined in the Laplace transformed domain, as

$$\begin{aligned} \tilde{K}_{\mathrm{I}}(s) &= \frac{\sqrt{\pi}}{2(\alpha_3\alpha_2 - \alpha_1\alpha_4)\sqrt{2r}}(\alpha_2\Delta\tilde{u}_2 - \alpha_4\Delta\tilde{u}_1), \\ \tilde{K}_{\mathrm{II}}(s) &= \frac{\sqrt{\pi}}{2(\alpha_3\alpha_2 - \alpha_1\alpha_4)\sqrt{2r}}(\alpha_3\Delta\tilde{u}_1 - \alpha_1\Delta\tilde{u}_2). \end{aligned} \tag{5.9}$$

5.1.4 Numerical Examples

A. A square plate for dynamic analysis in elastic materials

Consider a square plate of elastic materials shown in Figure 5.1. The length and the height of the plate are equal to 1, young's modulus $E = 1$ is chosen for normalization and

Poisson's ratio $\nu = 0.3$. The Heaviside uniform tensile load is applied to the top of the model, the bottom is fixed for the boundary conditions. The two free parameters in inverse Laplace domain are picked as $T_0 = 10,$ and $\eta = 5$, the number of sample in the Laplace domain is $L = 25$. In this case, the displacement of the middle point (0.5, 0.5) is selected to compare with FEM.

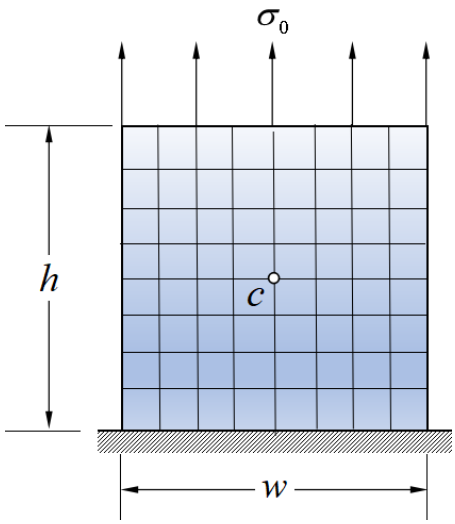

Figure 5.1 A square plate with number of node $N_1 = N_2 = 9$ and their distribution.

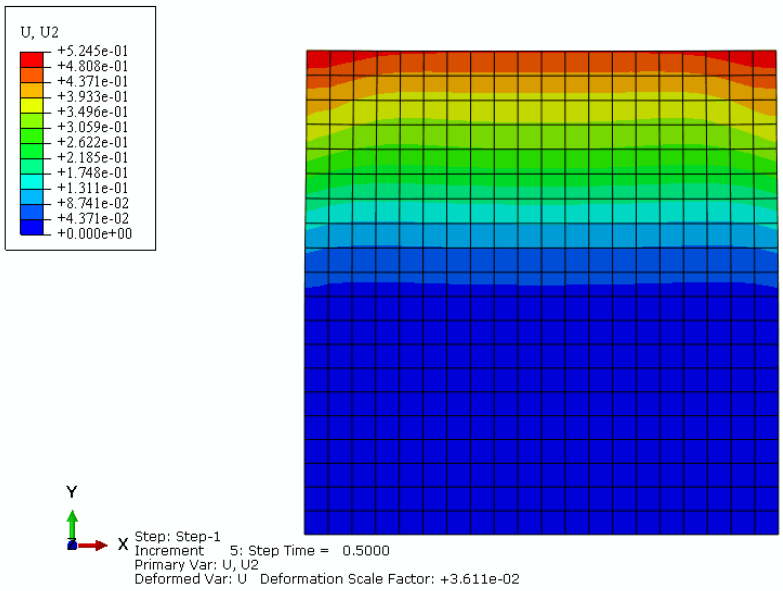
U, U2
+5.245e-01
+4.808e-01
+4.371e-01
+3.933e-01
+3.496e-01
+3.059e-01
+2.622e-01
+2.185e-01
+1.748e-01
+1.311e-01
+8.741e-02
+4.371e-02
+0.000e+00
Y
X
Step: Step-1
Increment 5: Step Time = 0.5000
Primary Var: U, U2
Deformed Var: U Deformation Scale Factor: +3.611e-02

(a)

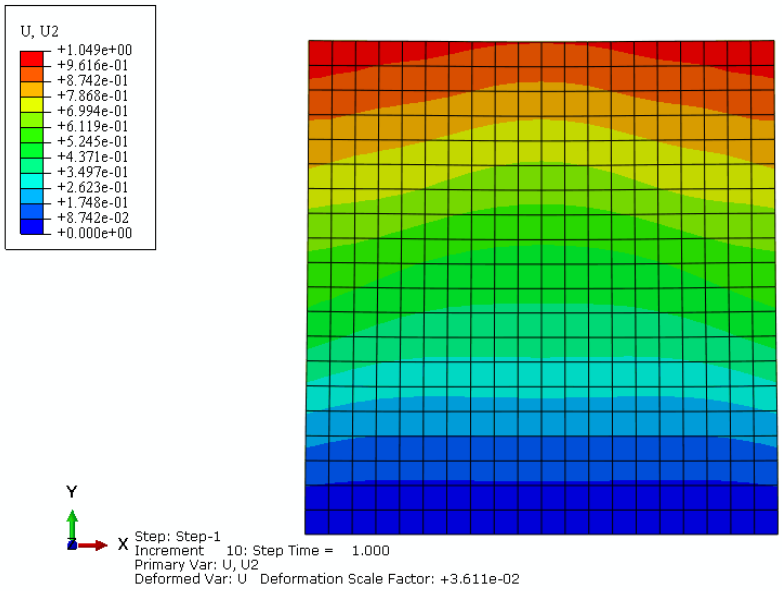
U, U2
+1.049e+00
+9.616e-01
+8.742e-01
+7.868e-01
+6.994e-01
+6.119e-01
+5.245e-01
+4.371e-01
+3.497e-01
+2.623e-01
+1.748e-01
+8.742e-02
+0.000e+00
Y
X
Step: Step-1
Increment 10: Step Time = 1.000
Primary Var: U, U2
Deformed Var: U Deformation Scale Factor: +3.611e-02

(b)

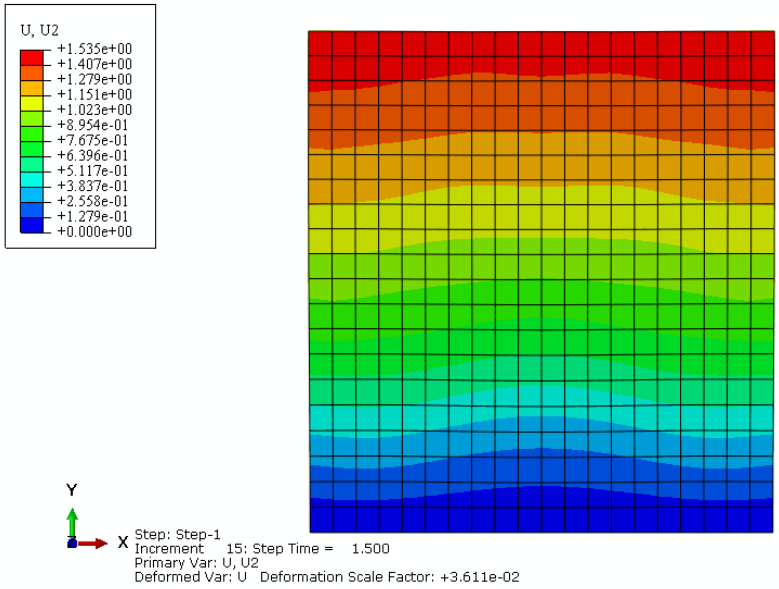

(c)

Figure 5.2 The displacement in ABAQUS with different time (a) $t = 0.5$, (b) $t = 1.0$, (c) $t = 1.5$.

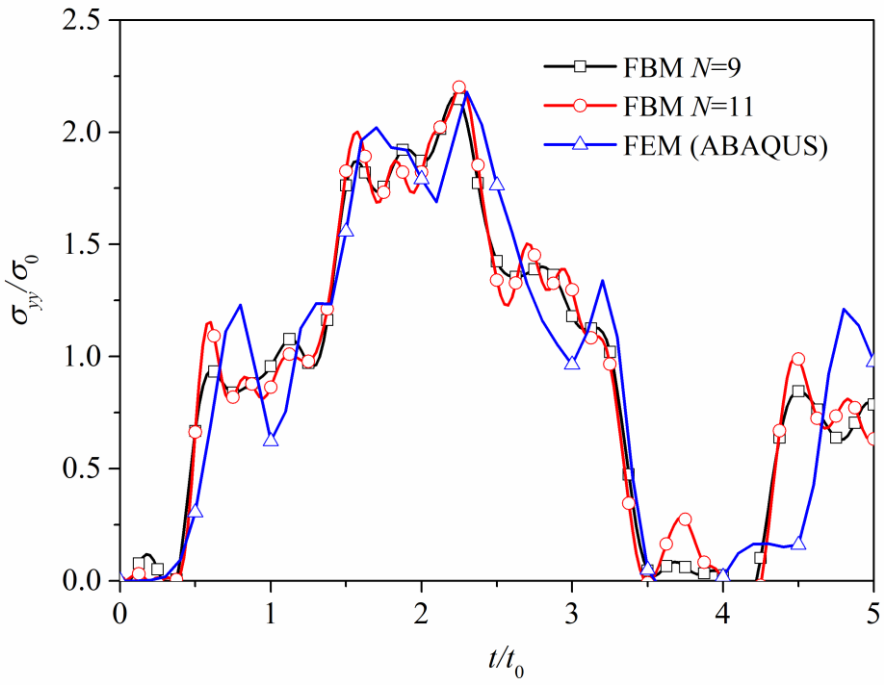

Figure 5.3 The normalized stress of point (c) for elastic materials.

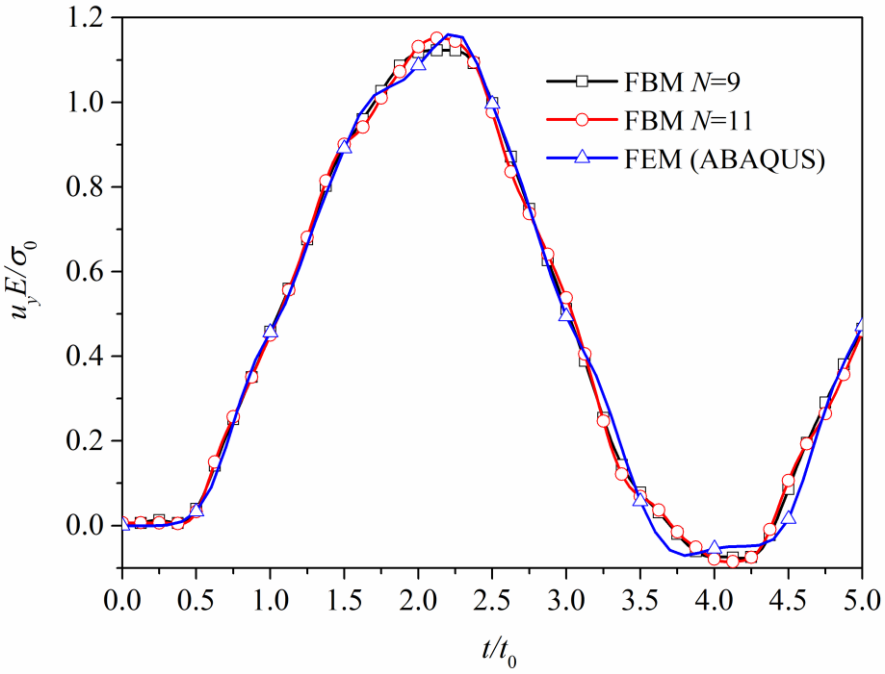

Figure 5.4 The normalized displacement of point (c) for elastic materials.

From the Figure 5.2, it can be observed that the change of displacement of solid materials when the elastic wave propagates. The normalized stress and displacement for the center of the model is plotted in Figure 5.3 and Figure 5.4 by both FBM and FEM. The velocity of the elastic wave $c = \sqrt{E/\rho} = 1$, so that the time for the elastic wave arrive at the target point is 0.5. A comparison of different number of nodes in FBM is presented for the convergence test in dynamic analysis. Moreover, compare with FEM (ABAQUS), the accuracy can be verified with small error occurs.

B. A square plate with a central hole for dynamic analysis in elastic materials

Consider a plate with central hole described in Figure 5.5, the Young's modulus $E = 1$ is chosen for normalization and Poisson's ratio $\nu = 0.3$. The two parameters in inverse Laplace functions are selected as $T_0 = 60$, $\eta = 5$ and the number of sample in the

Laplace domain is $L = 25$. The numerical results of normalized stress $\sigma(x,t)/\sigma_0$ versus the normalized time t/t_0 are plotted in Figure 5.7-5.10. The results are compared with FEM and good agreement can be shown in this case when the number of node $N_1^{\mathrm{I}} = N_1^{\mathrm{II}} = N_2^{\mathrm{I}} = N_2^{\mathrm{II}} = 9$.

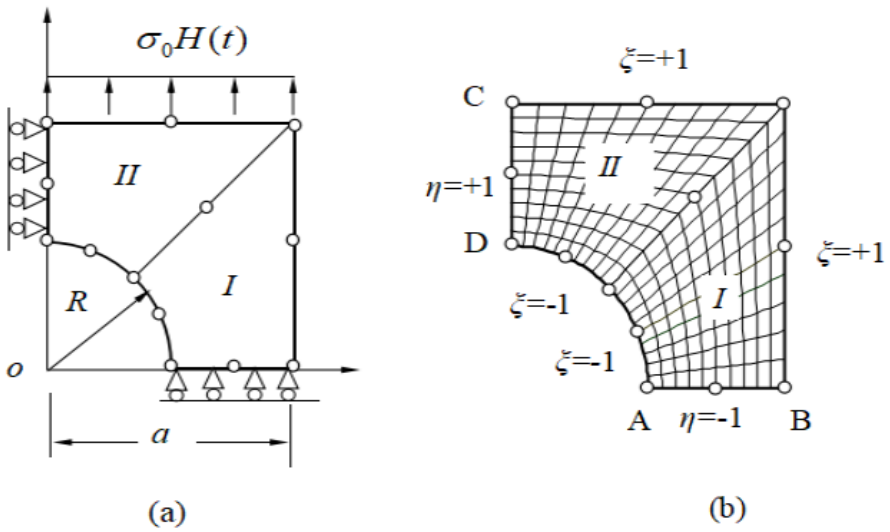

Figure 5.5 Blocks of a quarter square plate and their mapping seeds (a)geometry; (b) distribution of node and two blocks.

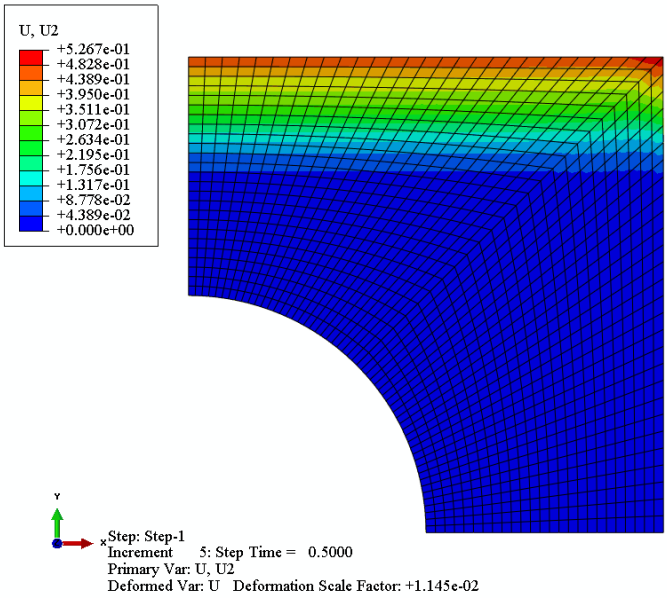

(a)

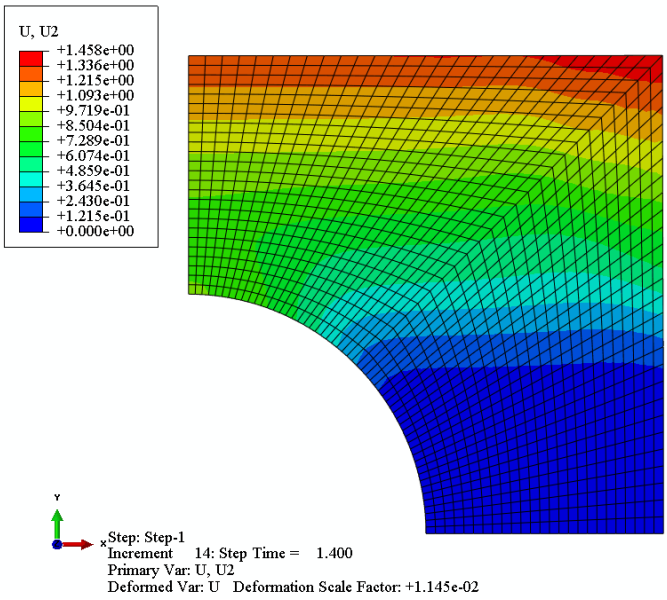

(b)

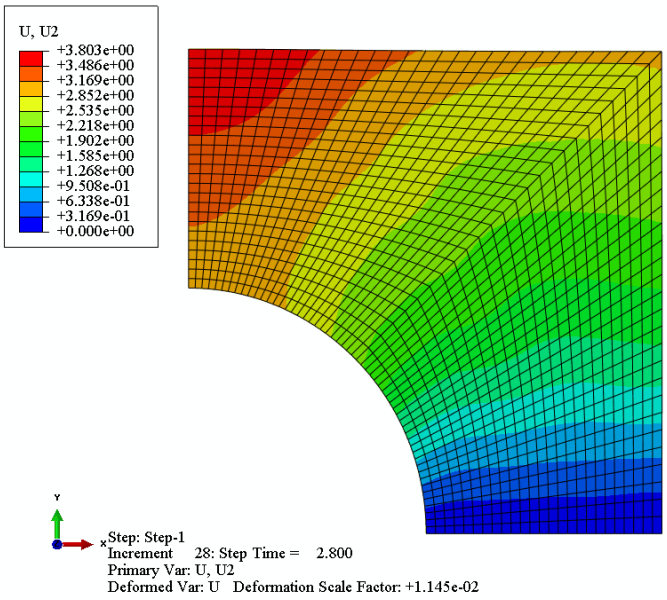

(c)

Figure 5.6 The displacement in ABAQUS with different time (a) $t = 0.5$, (b) $t = 1.4$, (c) $t = 2.8$.

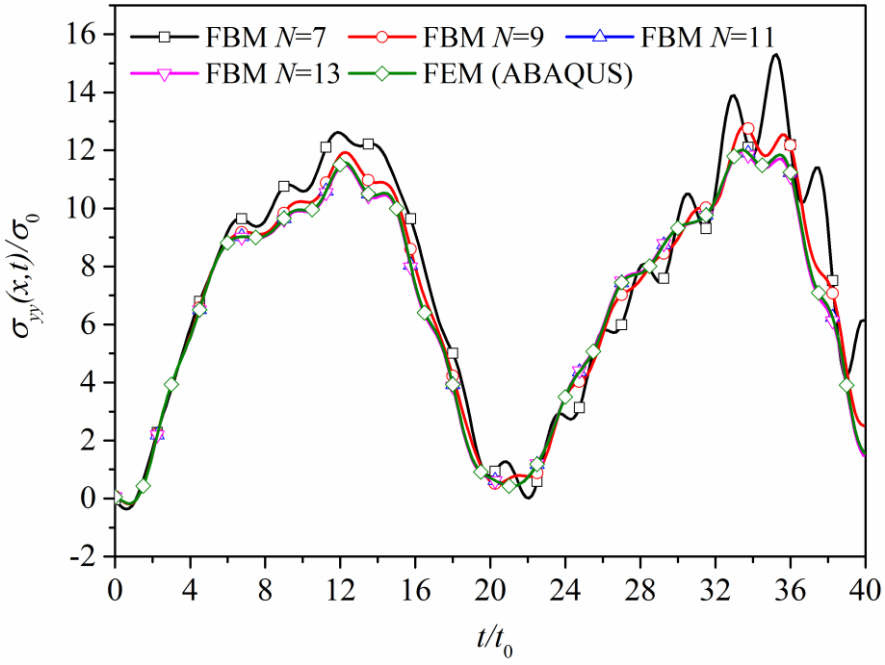

Figure 5.7 The normalized stress of point A for elastic materials.

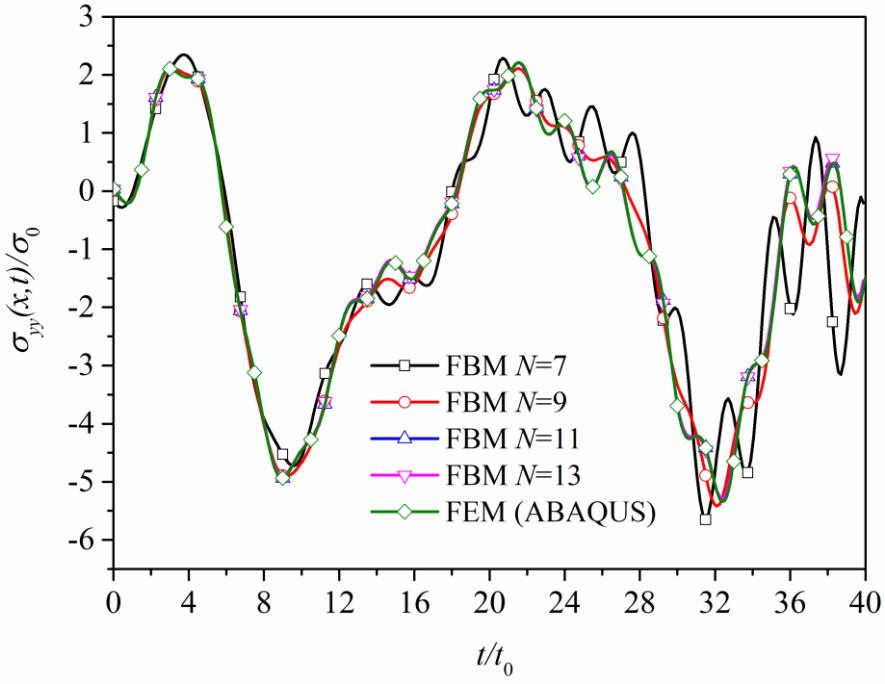

Figure 5.8 The normalized stress of point B for elastic materials.

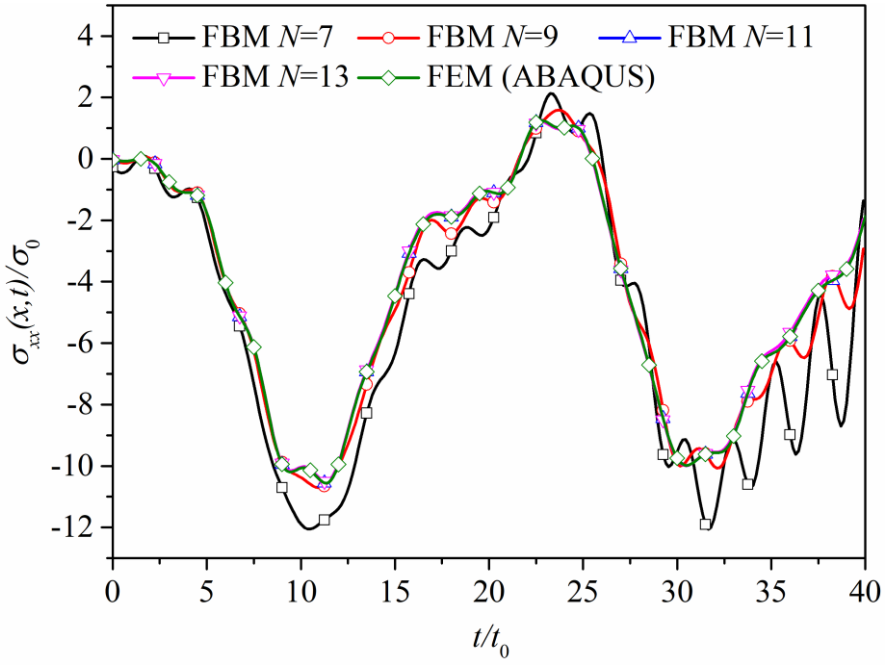

Figure 5.9 The normalized stress of point C for elastic materials.

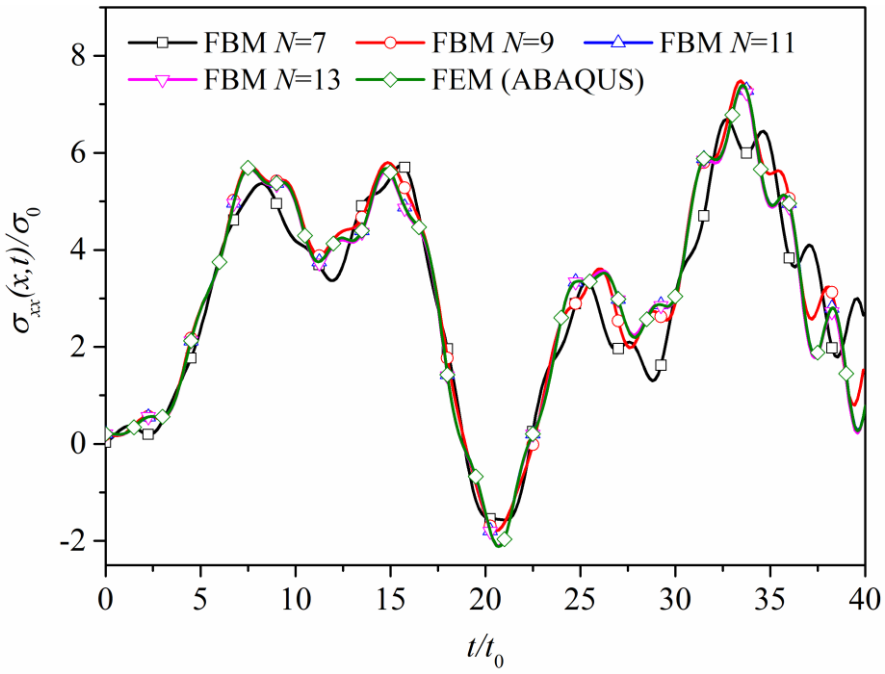

Figure 5.10 The normalized stress of point D for elastic materials.

Figure 5.6 illustrates that the movement of the elastic wave and its effect to the displacement. In addition, the normalized stress of different position in a square with a

central hole is plotted in Figure 5.7-5.10 for both FBM and FEM. Similarly, the velocity of the elastic wave is $c = \sqrt{E/\rho} = 1$. It can be notified that as the number of nodes *N*=7, the result is damping, while as the number of nodes increase, the result is more stable. Besides, compare to the result of FEM (ABAQUS), good agreement has been made for the accuracy test of the FBM on dynamic analysis.

C. A beam under Heaviside load for dynamic analysis in orthotropic FGMs

Firstly, consider a beam of length *l* and height *h* with anisotropic FGMs in horizontal direction subjected to Heaviside load as shown in Figure 5.11. One dimensional problem with isotropic FGM, i.e. $E_1 = E_2 = E_0 e^{\alpha x/l}$, $\alpha = \ln(E_l / E_0)$, is analyzed for comparison of the analytical solutions. In addition, by reason of convenience of calculation, the mass density is considered as $\rho = \rho_0 e^{\alpha x/l}$. In this case, the equilibrium equation becomes

$$E_0 \frac{\partial^2 u}{\partial x^2} + \frac{\beta E_0}{l} \frac{\partial u}{\partial x} = \rho_0 \frac{\partial^2 u}{\partial t^2}, \tag{5.10}$$

where u is displacement along axial direction and t is time. With zero initial boundary condition, the general solution of displacement in the Laplace transform domain is given by

$$u(x,s) = A_1 e^{\lambda_1 x/l} + A_2 e^{\lambda_2 x/l}, \tag{5.11}$$

where A_i are constants to be determined by boundary conditions and

$$\lambda_1 = \frac{-\beta + \sqrt{\beta^2 + 4l^2 s^2/c^2}}{2}, \quad \lambda_2 = \frac{-\beta - \sqrt{\beta^2 + 4l^2 s^2/c^2}}{2}, \tag{5.12}$$

in which $c=\sqrt{E_0/\rho_0}$ (velocity of longitudinal elastic wave) and s is Laplace transform parameter. For Heaviside load acting on the right-hand end, the solution of displacement gives

$$u(x,s)=\frac{\sigma_0 l e^{-\beta}}{sE_0(\lambda_1 e^{\lambda_1}-\lambda_2 e^{\lambda_2})}\left(e^{\lambda_1 x/l}-e^{\lambda_2 x/l}\right). \tag{5.13}$$

Therefore, the solution of stress yields

$$\sigma(x,s)=\frac{\sigma_0 e^{-\beta(l-x)/l}}{s(\lambda_1 e^{\lambda_1}-\lambda_2 e^{\lambda_2})}\left(\lambda_1 e^{\lambda_1 x/l}-\lambda_2 e^{\lambda_2 x/l}\right). \tag{5.14}$$

By using FBM, the geometry parameter is $h/l=0.2$ (the solution is independent of the ratio in the case of zero Poisson ratio), the ratio $E_l/E_0=5$ and one block is applied. In the Durbin's Laplace inversion method, parameters are selected as $\eta=5$, $T_0/t_0=20$ ($t_0=l/c$) and number of samples in the Laplace domain $L=25$. The analytical and numerical results of normalized displacement $u(x,t)/l$ and stress $\sigma(x,t)/\sigma_0$ versus the normalized time t/t_0 are plotted in Figure 5.12 and Figure 5.13. The agreement is shown to be excellent, so that it is hard to see the difference between these two results.

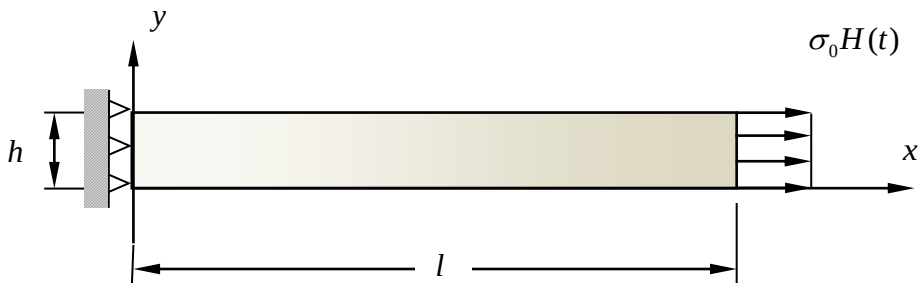

Figure 5.11 A beam under Heaviside load on FGMs.

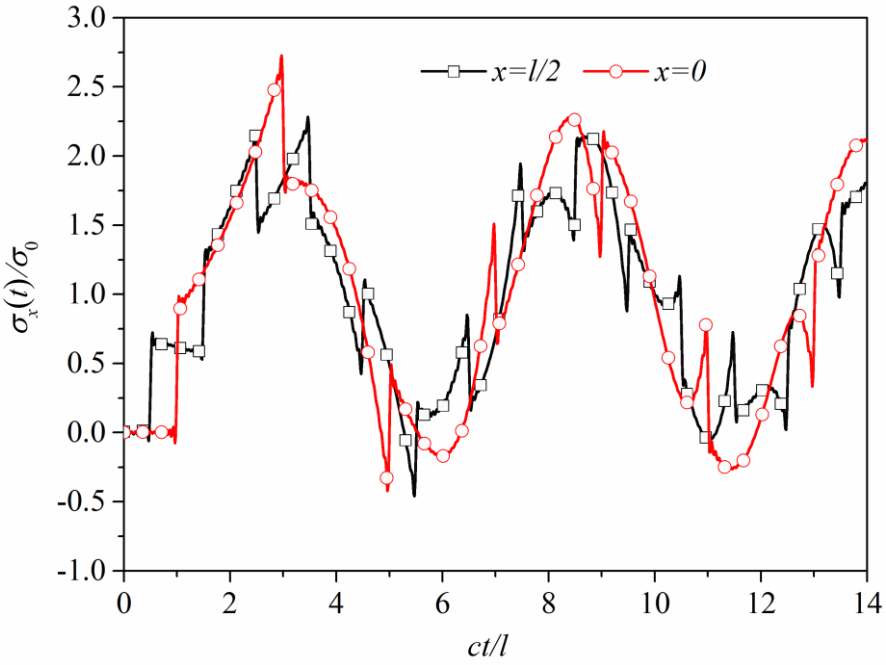

Figure 5.12 Stresses in a FGM bar under dynamic load when the ratio $E_l / E_0 = 5$.

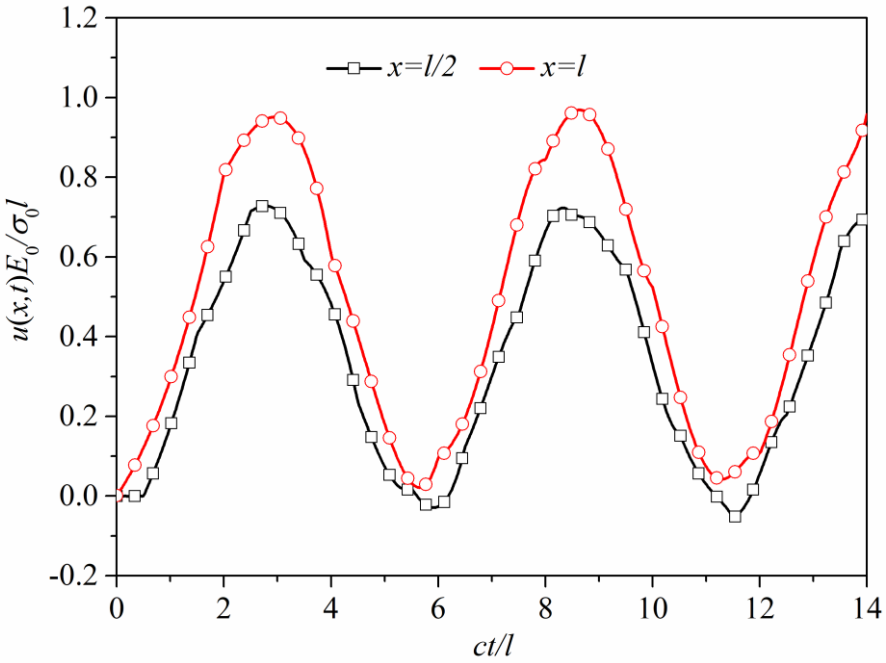

Figure 5.13 Displacements in a FGM bar under dynamic load when the ratio $E_l / E_0 = 5$.

D. A plate under Heaviside load for dynamic analysis in isotropic FGMs

Second, consider an isotropic FGM square plate $(h = l)$ as shown in Figure 5.14. The isotropic material is considered and the elastic modulus have an exponential variation in the x_1 directions as $E_1 = E_2 = E_0 f(x_1)$ and the Poisson ratio $\nu = 0.3$ with assumption of plane stress, where $f(x_1) = \exp(\alpha x_1 / l)$ and $\alpha = \ln(E_l / E_0)$. The ratio E_l / E_0 is selected to be 2. The results of normalized displacement $E_0 u(l, h/2, t)/\sigma_0 l$ and stress $\sigma_{11}(0, h/2, t)/\sigma_0$ versus the normalized time $c_s t / l$ are plotted in Figure 5.15 and Figure 5.16, where $c_s = \sqrt{G_{12}^0 / \rho_0}$, $G_{12}^0 = E_0 / 2(1+\nu)$ is shear modulus and c_s the velocity of elastic shear wave of the isotropic material on the left-hand end. Two free parameters in Durbin's Laplace inversion method are selected as the same as that for one dimensional case.

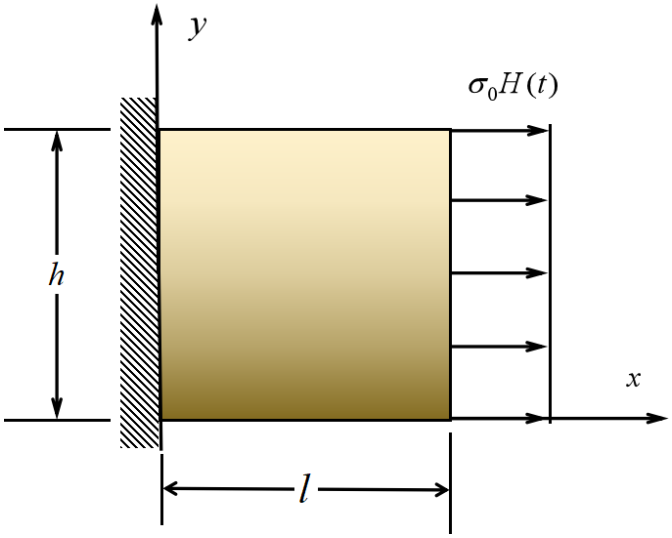

Figure 5.14 A plate under Heaviside load on FGMs.

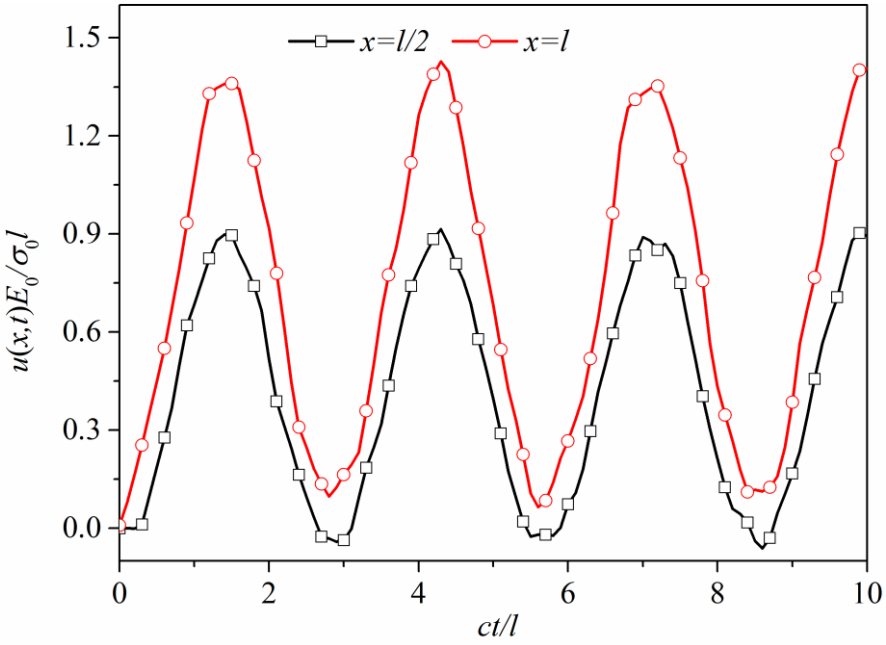

Figure 5.15 Displacements of FGM plate under dynamic load along the middle of plate $y = h/2$ when the ratio $E_l / E_0 = 2$.

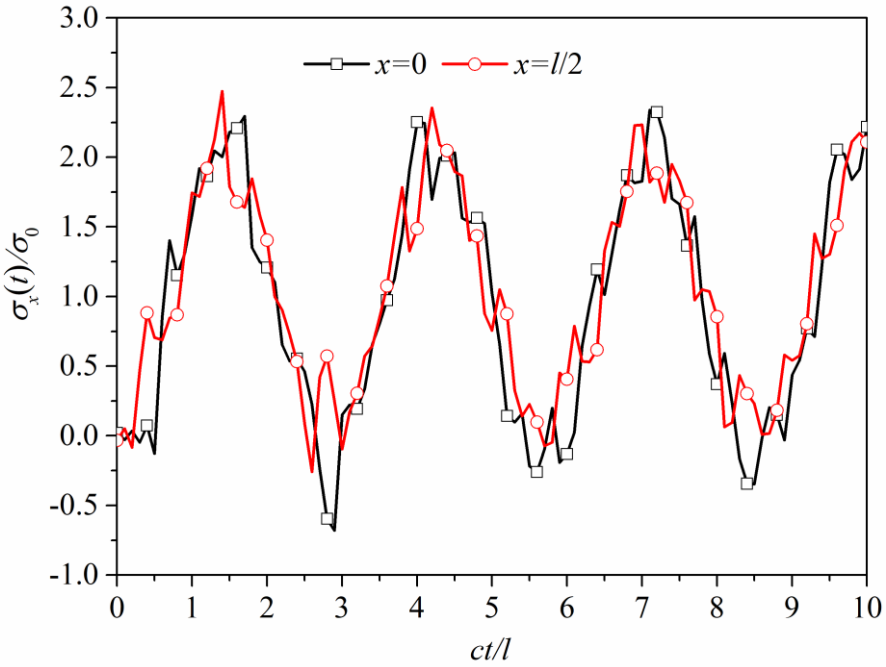

Figure 5.16 Stresses of FGM plate under dynamic load along the middle of plate $y = h/2$ when the ratio $E_l / E_0 = 2$.

E. An edge crack of a plate for dynamic analysis in orthotropic FGMs

An orthotropic FGM plate of $w \times 2h$ containing an edge crack of length a shown in Figure 5.17 is analyzed. Heaviside uniform tensile load $\sigma_0 H(t)$ is applied on the top of the plate and the bottom is fixed. The dimensions is selected $w = 2a$, $h = w$ and the shear modulus is an exponential function of x, i.e. isotropic material is considered and the elastic modulus have an exponential variation in the x direction as i.e. $E_1 = E_1^0 f(x)$, $E_2 = E_2^0 f(x)$, $G_{12} = G_{12}^0 f(x)$ and $\rho = \rho_0$ (constant), where $f(x) = \exp(\alpha x / w)$ and α is dimensionless constant and E_1^0, E_2^0 , G_{12}^0 and ρ_0 are elastic modulus and mass density at origin, $\alpha = \ln(E_1^w / E_1^0)$, in which E_1^0 and E_1^w are the Young's modulus of the left-hand side and right-hand edge respectively. To simplify the numerical investigation, assume that $E_1^w / E_1^0 = E_2^w / E_2^0 = G_{12}^w / G_{12}^0 = \beta$. An orthotropic material, E-glass-epoxy (A), is considered with $E_1^0 = 8.26 G_{12}^0$, $E_2^0 = 2.26 G_{12}^0$, $\nu_{12} = 0.227$, $\nu_{21} = 0.062$ and $G_{12}^0 = 5.5\,\text{GPa}$. Again, four blocks are used in the discretization numerical procedure.

The stress intensity factors are computed from the normal crack displacements near the crack-tip ($r_0 / a = 0.955$). Because the structure of the asymptotic crack-tip fields for non-homogeneous solids under dynamic load is the same as that for homogeneous material, the dynamic stress intensity factors can be evaluated by Eq. (5.9).

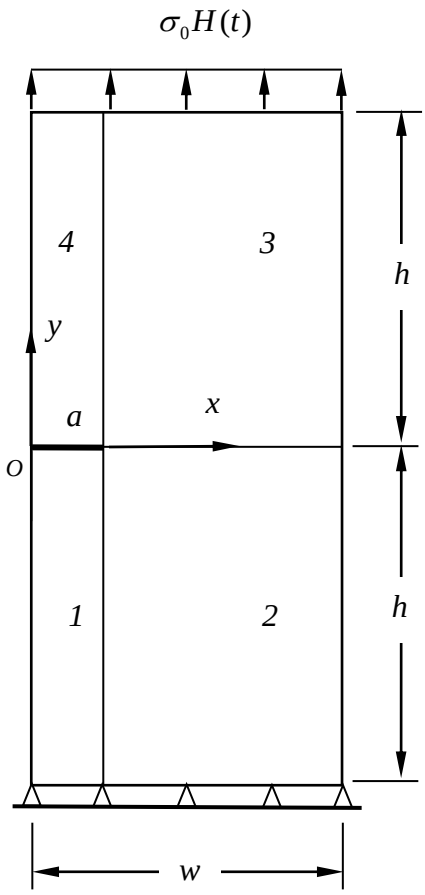

Figure 5.17 The edge crack of a plate for dynamic analysis.

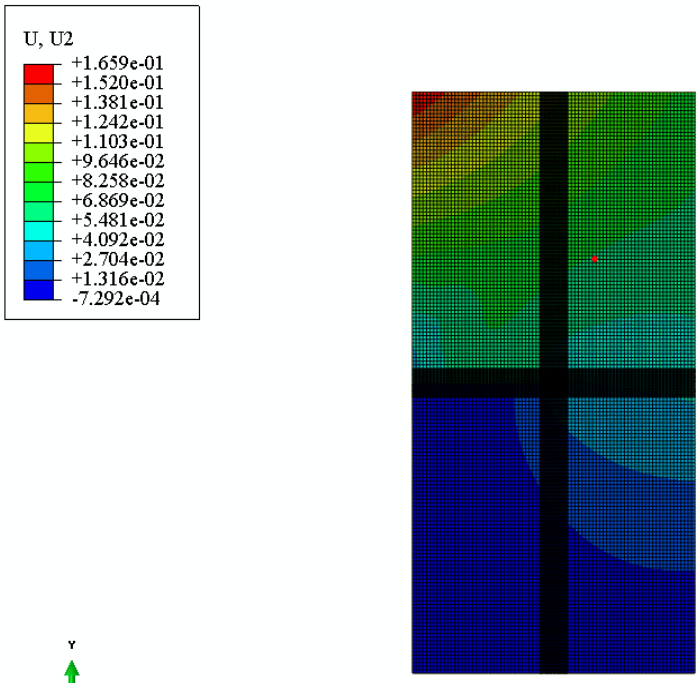
U, U2
+1.659e-01
+1.520e-01
+1.381e-01
+1.242e-01
+1.103e-01
+9.646e-02
+8.258e-02
+6.869e-02
+5.481e-02
+4.092e-02
+2.704e-02
+1.316e-02
-7.292e-04
Y
X
Step: DYNAMICEANALYSIS
Increment 30: Step Time = 0.6000
Primary Var: U, U2
Deformed Var: U Deformation Scale Factor: +5.145e-02

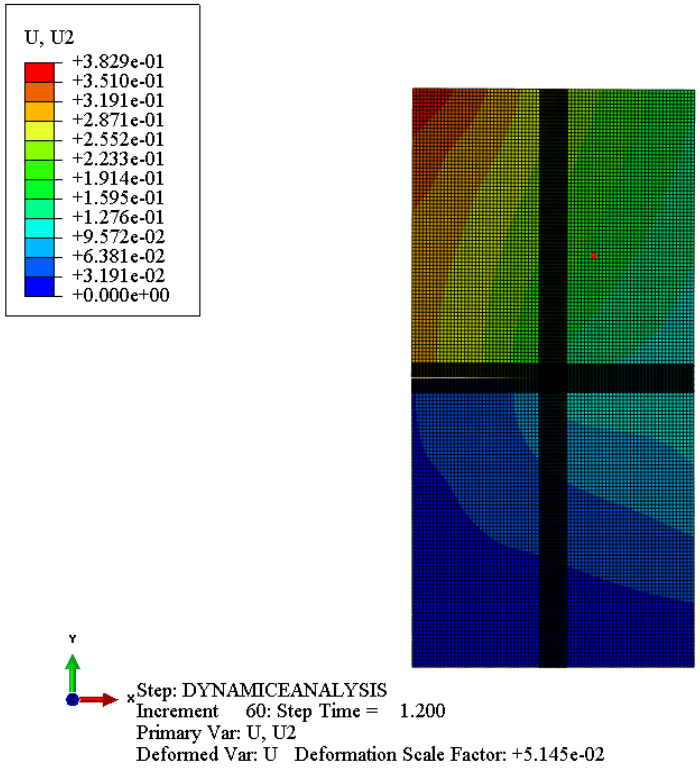
U, U2
+3.829e-01
+3.510e-01
+3.191e-01
+2.871e-01
+2.552e-01
+2.233e-01
+1.914e-01
+1.595e-01
+1.276e-01
+9.572e-02
+6.381e-02
+3.191e-02
+0.000e+00
Y
X
Step: DYNAMICEANALYSIS
Increment 60: Step Time = 1.200
Primary Var: U, U2
Deformed Var: U Deformation Scale Factor: +5.145e-02

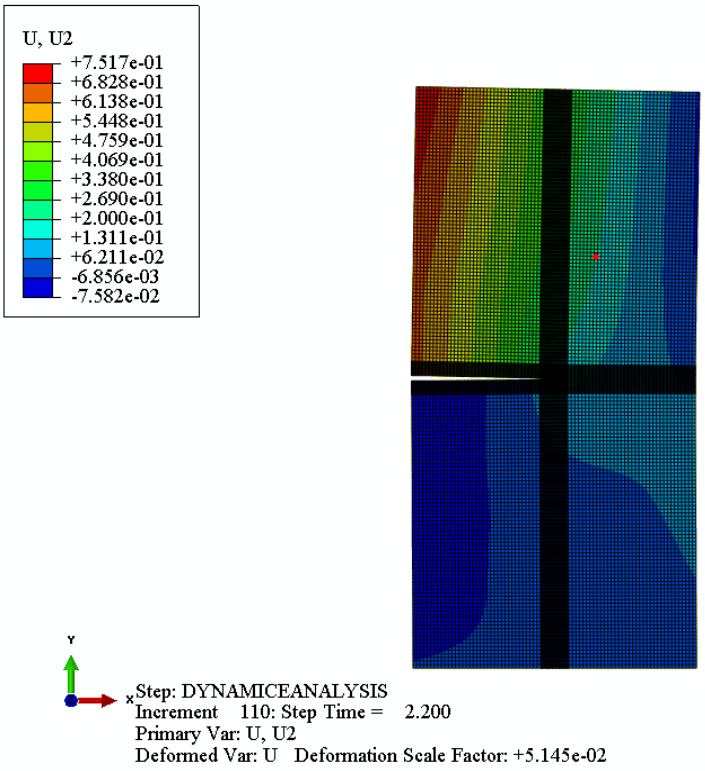

Figure 5.18 The edge crack of a plate in orthotropic materials with different time (a) $t = 0.6$, (b) $t = 1.2$, (c) $t = 2.3$.

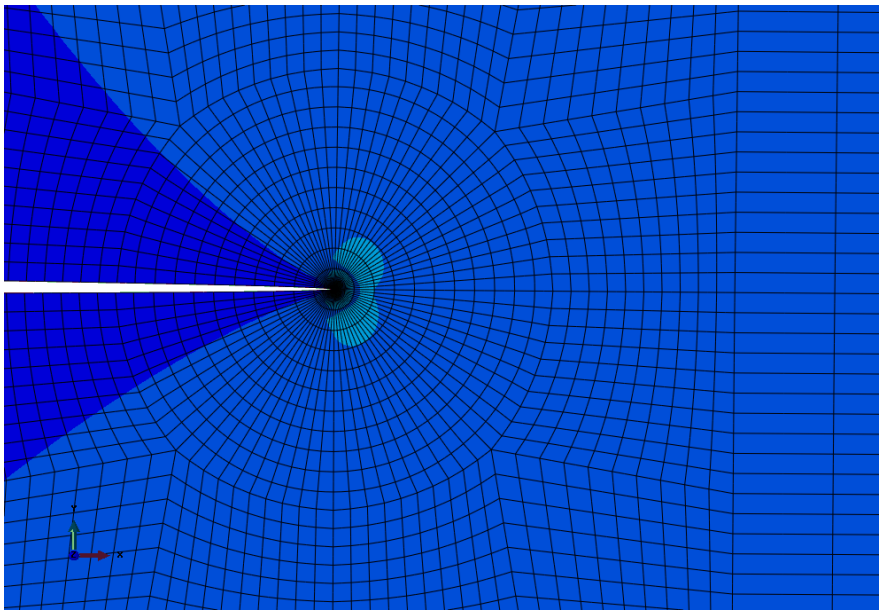

Figure 5.19 The stress distribution near the crack tip with fine mesh.

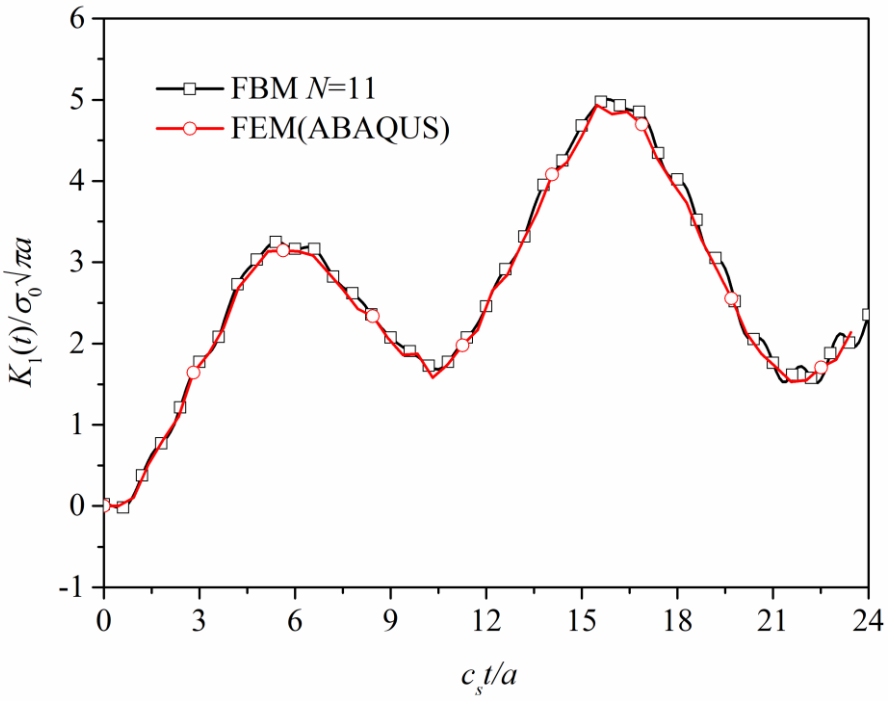

Figure 5.20 The normalized stress intensity factor $K_I(t)/\sigma_0\sqrt{\pi a}$ of edge crack in an orthotropic FGM plate (compared with FEM).

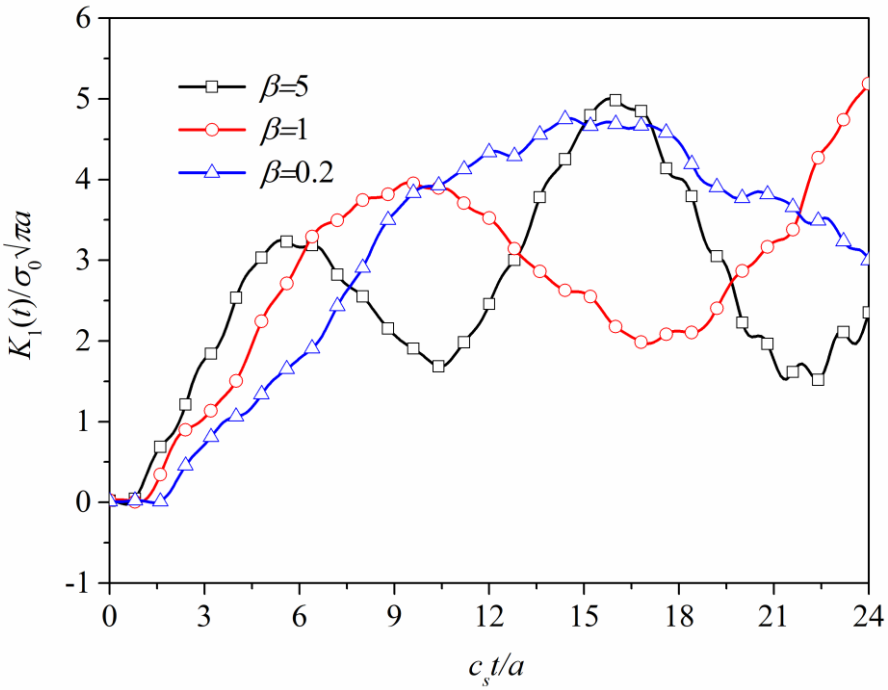

Figure 5.21 The normalized stress intensity factor $K_I(t)/\sigma_0\sqrt{\pi a}$ of edge crack in an orthotropic FGM plate (different ratios).

To compare with results by FEM, we take $\beta = 5$ and the present the time variations of the normalized dynamic stress intensity factors $K_I(t)/\sigma_0\sqrt{\pi a}$ versus the normalized time $c_s t/a$ in Figure 5.20, where $c_s = \sqrt{G_{12}^0/\rho_0}$. Excellent agreement compared with the results obtained by FEM has been achieved. In addition, Figure 5.21 shows the dynamic SIFs for different ratios of β. In the case of $\beta = 5$, the arrival time for the longitudinal waves starting from the top to the crack tip is shorter than that in the case of $\beta = 0.2$. The results for homogeneous composite $\beta = 1$ are also presented in the same figure. With decreasing of the gradient parameter β, the maximum value of the stress intensity factors for the first peak increases. However, for large value of the gradient parameter β, the wave velocity is increasing with uniform mass density as expected. It means that the corresponding peak values of the dynamic stress intensity factors are attained at smaller time instants for higher β-values. In addition, the effect by four edges are huge. In the region $c_s t/a < 24$, there are two peaks for large ratio of β=5. But there is only one peak for small value of β=0.2.

5.2 Dynamic of T-stress

5.2.1 Transient Elastodynamic Plane Strain Fields Around the Crack Tip

In the Laplace transform domain, the asymptotic structure of the transient elastodynamic near-tip fields around a stationary crack is investigated for all three fracture modes by Deng [108]. The transient fields have been derived as the sum of their quasi-static counterparts and the corresponding transient correction terms, in terms of variable-separable expansions. All components of stress in the Cartesian coordinate are obtained, for the symmetric problem, by

$$\tilde{\sigma}_x^c = \sum_{n=1}^{\infty} r^{n/2-1} \frac{n}{4} \left\{ [(4+n)\tilde{A}_n - 2\tilde{B}_n]\cos(n/2-1)\theta - (n-2)\tilde{A}_n \cos(n/2-3)\theta + \frac{4}{n} h_n \right\}$$

$$\tilde{\sigma}_y^c = \sum_{n=1}^{\infty} r^{n/2-1} \frac{n}{4} \left\{ [(4-n)\tilde{A}_n + 2\tilde{B}_n]\cos(n/2-1)\theta + (n-2)\tilde{A}_n \cos(n/2-3)\theta + \frac{4}{n} p_n \right\}$$

$$\tilde{\tau}_{xy}^c = \sum_{n=1}^{\infty} r^{n/2-1} \frac{n}{4} \left\{ -[n\tilde{A}_n - 2\tilde{B}_n]\sin(n/2-1)\theta + (n-2)\tilde{A}_n \sin(n/2-3)\theta + \frac{4}{n} q_n \right\}$$

(5.15)

and displacements

$$\tilde{u}_x^c = \sum_{n=1}^{\infty} r^{n/2} \frac{n}{2G} \left\{ [(3-4\nu+n/2)\tilde{A}_n - \tilde{B}_n]\cos(n/2\theta) - n/2\tilde{A}_n \cos(n/2-2)\theta + 2Gf_n \right\} + \tilde{U}_0$$

$$\tilde{u}_y^c = \sum_{n=1}^{\infty} r^{n/2} \frac{n}{2G} \left\{ [(3-4\nu-n/2)\tilde{A}_n + \tilde{B}_n]\sin(n/2\theta) + n/2\tilde{A}_n \sin(n/2-2)\theta + 2Gg_n \right\}$$

(5.16)

where G is the shear modulus, $\tilde{U}_0$ indicates the horizontal displacement Laplace transformation at crack-tip $(r=0)$, h_n, p_n, q_n, f_n and g_n are due to the transient effects. For zero initial condition and $n=1,2,3$ and 4, they are zero, and for $n=5,6,7$ and 8, they are given by

$$h_n=\frac{s^2}{2c_s^2}\left\{\frac{1}{n-2}\left[\left(3-4\nu+\frac{n-6+4\nu}{2(1-2\nu)}\frac{c_s^2}{c_1^2}\right)\tilde{A}_{n-4}-\frac{1}{1-2\nu}\frac{c_s^2}{c_1^2}\tilde{B}_{n-4}\right]\cos(n/2-1)\theta\right.$$

$$\left.+\left[\left(\frac{n-4}{8}+\frac{n+4}{8}\frac{c_s^2}{c_1^2}\right)\tilde{A}_{n-4}-\frac{1}{4}\left(1+\frac{c_s^2}{c_1^2}\right)\tilde{B}_{n-4}\right]\cos(n/2-3)\theta-\frac{n-4}{8}\left(1+\frac{c_s^2}{c_1^2}\right)\tilde{A}_{n-4}\cos(n/2-5)\theta\right\},$$

$$p_n=\frac{s^2}{2c_s^2}\left\{-\frac{1}{n-2}\left[\left(3-4\nu-\frac{n-2-4\nu}{2(1-2\nu)}\frac{c_s^2}{c_1^2}\right)\tilde{A}_{n-4}+\frac{1}{1-2\nu}\frac{c_s^2}{c_1^2}\tilde{B}_{n-4}\right]\cos(n/2-1)\theta\right.$$

$$\left.-\left[\left(\frac{n-4}{8}+\frac{n-12}{8}\frac{c_s^2}{c_1^2}\right)\tilde{A}_{n-4}-\frac{1}{4}\left(1+\frac{c_s^2}{c_1^2}\right)\tilde{B}_{n-4}\right]\cos(n/2-3)\theta+\frac{n-4}{8}\left(1+\frac{c_s^2}{c_1^2}\right)\tilde{A}_{n-4}\cos(n/2-5)\theta\right\},$$

$$q_n=\frac{s^2}{2c_s^2}\left\{\frac{1}{n-2}\left(3-4\nu-\frac{c_s^2}{c_1^2}\right)\tilde{A}_{n-4}\sin(n/2-1)\theta\right.$$

$$\left.-\left(1+\frac{c_s^2}{c_1^2}\right)\left[(n-4)\tilde{A}_{n-4}-2\tilde{B}_{n-4}\right]\sin(n/2-3)\theta+\frac{n-4}{8}\left(1+\frac{c_s^2}{c_1^2}\right)\tilde{A}_{n-4}\sin(n/2-5)\theta\right\},$$

$$f_n=\frac{s^2}{16(n-2)Gc_s^2}\left\{-\frac{2}{n}\left(1+\frac{c_s^2}{c_1^2}\right)\left[(n-4)\tilde{A}_{n-4}-2\tilde{B}_{n-4}\right]\cos(n/2\theta)+\right.$$

$$\left.\begin{bmatrix}\left((8-16\nu+n)+(n-8)\dfrac{c_s^2}{c_1^2}\right)\tilde{A}_{n-4}\\ -2\left(1+\dfrac{c_s^2}{c_1^2}\right)\tilde{B}_{n-4}\end{bmatrix}\cos(n/2-2)\theta-(n-2)\left(1+\frac{c_s^2}{c_1^2}\right)\tilde{A}_{n-4}\cos(n/2-4)\theta\right\},$$

$$g_n=\frac{s^2}{16(n-2)Gc_s^2}\left\{-\frac{2}{n}\left(1+\frac{c_s^2}{c_1^2}\right)\left[(n-4)\tilde{A}_{n-4}-2\tilde{B}_{n-4}\right]\sin(n/2\theta)\right.$$

$$\left.+\left[\left((16-16\nu-n)-n\frac{c_s^2}{c_1^2}\right)\tilde{A}_{n-4}+2\left(1+\frac{c_s^2}{c_1^2}\right)\tilde{B}_{n-4}\right]\sin(n/2-2)\theta+(n-2)\left(1+\frac{c_s^2}{c_1^2}\right)\tilde{A}_{n-4}\sin(n/2-4)\theta\right\},$$

(5.17)

in which the elasticity waves $c_s = (G/\rho)^{\frac{1}{2}}$ and $c_1 = [2(1-\nu)/(1-2\nu)]^{\frac{1}{2}} c_s$ in plane strain (replace ν with $\nu/(1+\nu)$ in plane stress). Under the transient dynamic condition, the relationships between the coefficients are

$$\tilde{B}_n = -(-1)^n \tilde{A}_n \tag{5.18}$$

for $n = 1,2,3$ and 4. When $n \geq 5$, they are

$$2nc_s^2\left[\tilde{A}_n + (-1)^n \tilde{B}_n\right] = \left[1-(-1)^n\right]\left[c_{n1}\tilde{A}_{n-4} + c_{n2}\tilde{B}_{n-4}\right]s^2 + \left[1+(-1)^n\right]\left[d_{n1}\tilde{A}_{n-4} + d_{n2}\tilde{B}_{n-4}\right]s^2, \tag{5.19}$$

where c_{n1}, c_{n2}, d_{n1} and d_{n2} are constants and are given by

$$\begin{aligned} c_{n1} &= \frac{1}{n-2}\left(3-4\nu-\frac{c_s^2}{c_1^2}\right),\ d_{n1} = \frac{3-4\nu}{n-2} - \left(1+\frac{n-2-4\nu}{2(n-2)(1-2\nu)}\frac{c_s^2}{c_1^2}\right), \\ c_{n2} &= \frac{1}{4}\left(1+\frac{c_s^2}{c_1^2}\right),\ d_{n2} = -\frac{1}{4} - \frac{1}{4}\left(1-\frac{1}{(n-2)(1-2\nu)}\right)\frac{c_s^2}{c_1^2}. \end{aligned} \tag{5.20}$$

In the polar coordinate, we have

$$\begin{aligned} \tilde{\sigma}_r^c &= \tilde{\sigma}_x^c \cos^2\theta + \tilde{\sigma}_y^c \sin^2\theta + 2\tilde{\tau}_{xy}^c \sin\theta\cos\theta, \\ \tilde{\sigma}_\theta^c &= \tilde{\sigma}_x^c \sin^2\theta + \tilde{\sigma}_y^c \cos^2\theta - 2\tilde{\tau}_{xy}^c \sin\theta\cos\theta, \\ \tilde{\tau}_{r\theta}^c &= (\tilde{\sigma}_y^c - \tilde{\sigma}_x^c)\sin\theta\cos\theta + \tilde{\tau}_{xy}^c(\cos^2\theta - \sin^2\theta) \end{aligned} \tag{5.21}$$

and

$$\begin{aligned} \tilde{u}_r^c &= \tilde{u}_x^c \cos\theta + \tilde{u}_y^c \sin\theta, \\ \tilde{u}_\theta^c &= -\tilde{u}_x^c \sin\theta + \tilde{u}_y^c \cos\theta. \end{aligned} \tag{5.22}$$

In particular, we note that when $n = 1$, the usual stress intensity factors $\tilde{K}_I(s)$ and $n = 2$ the *T*-stress can be expressed in terms of coefficients as

$$\tilde{K}_I(s) = \tilde{A}_1\sqrt{2\pi}\ ,\ \ \tilde{T}(s) = 4\tilde{A}_2\,. \tag{5.23}$$

5.2.2 Numerical Examples

Circular and square sheets with central crack under dynamic load

Firstly, consider a circular disk with a central crack of length $2a$ subjected to uniformly distributed normal traction $\sigma_0 H(t)$ along the circumference, where $H(t)$ is a Heaviside function. Due to the symmetric, only a quarter of disk is modelled with plane stress assumption and the Poison's ratio $\nu = 0.3$. Let $a/R = 0.5$ and all other parameters $r_0/R = 0.1$ and the number of seeds for both the blocks and the collocation point are selected as the same as that in the example for static load in chapter 4. In the Laplace transform and the inverse procedure, L is selected as 25, $\sigma = 5$ and $T_0/t_0 = 20$, where $t_0 = R/c_0$ and $c_0 = \sqrt{E/\rho}$. The results of the SIF when $K \geq 25$ are very close.

Finally, consider a square sheet with central crack of length $2a$ under uniformly distributed normal tractions $\sigma_0 H(t)$ on the top and the bottom of the plate. The Poison's ratio $\nu = 0.3$, and $H/W = 1$, in the transformed domain, the Williams' series of stress and displacement are employed. In the Laplace transform and the Durbin's inverse procedure, $L = 25$, $\eta = 5$ and $T_0/t_0 = 20$, in which $t_0 = H/c_0$.

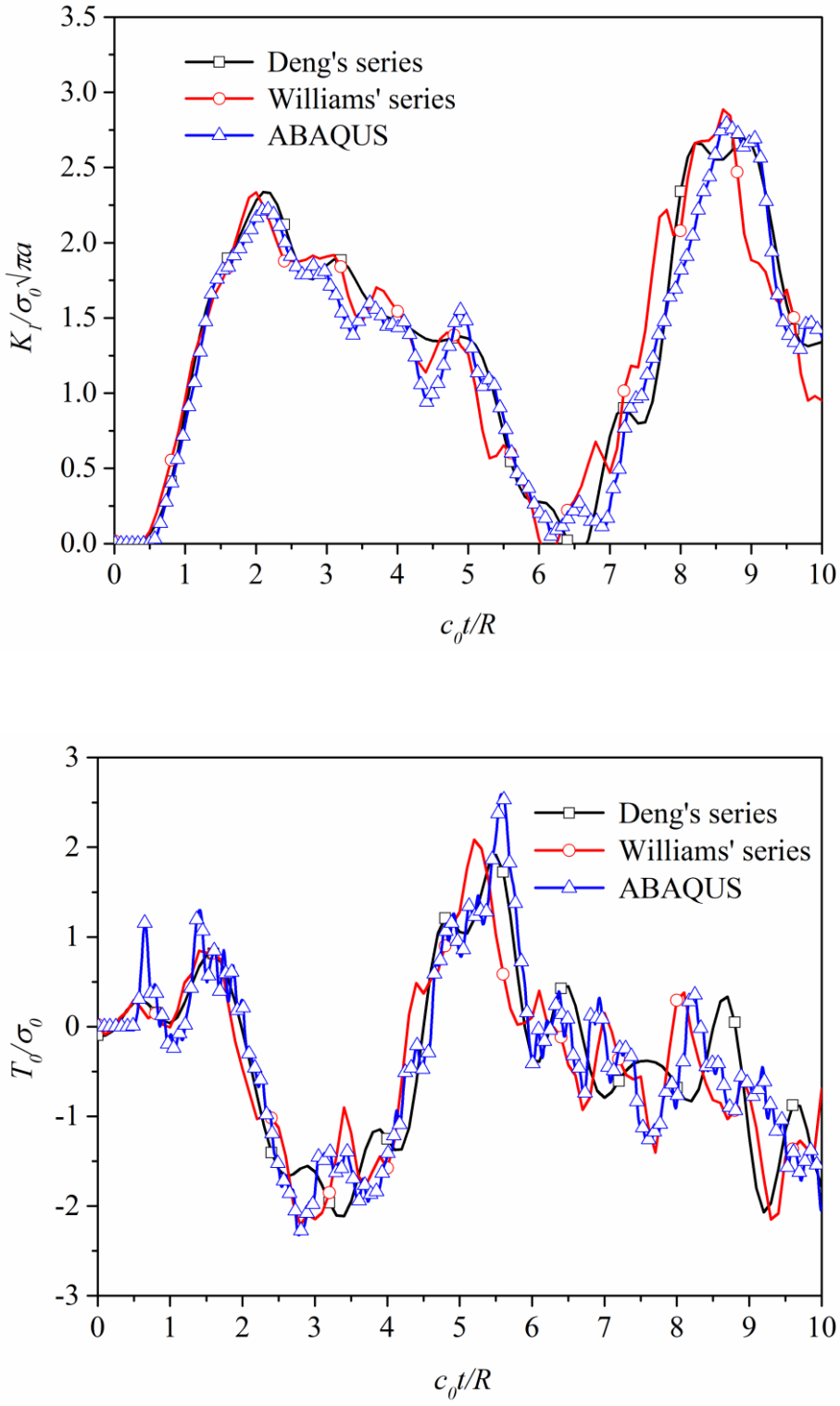

Figure 5.22 Time dependent normalized SIF and the *T*-stress when *a/R*=0.5 with comparison of the Deng's series, the Williams series and ABAQUS.

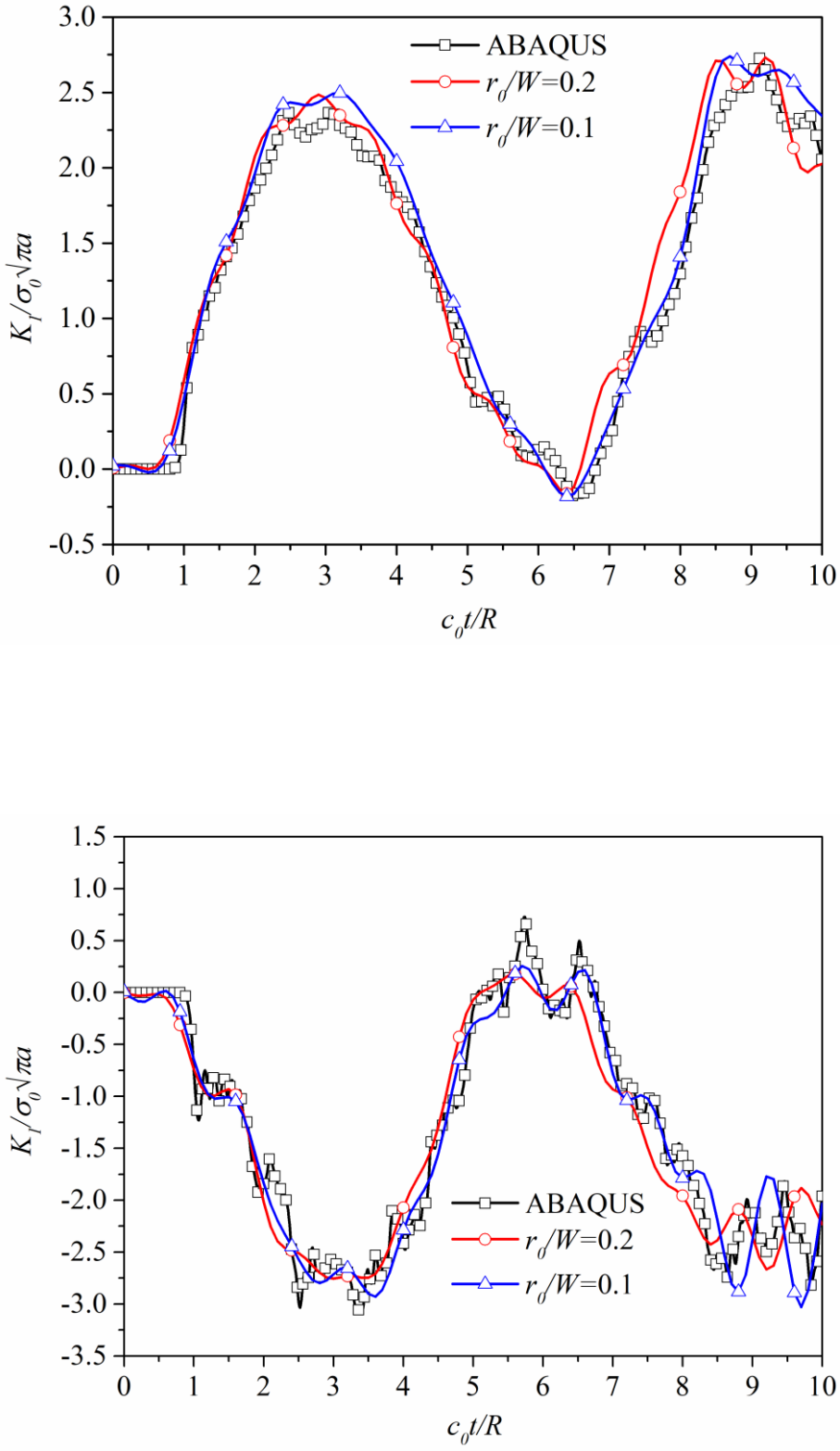

Figure 5.23 Time dependent normalized SIF and the *T*-stress when a/W=0.5 with comparison between different sizes of core and ABAQUS.

Figure 5.22 shows the variations of the normalised SIFs and the *T*-stresses versus the normalised time $c_0 t/R$ respectively. The results given by the FEM (ABAQUS) are presented in the same figures for comparison. Apparently, before the arrival time of dilatation wave travelling from the circumference to the crack-tip, the SIF and the *T*-stress should remain zero. The agreement between these solutions is reasonable. In addition, the results of the stress intensity and the *T*-stress with the Williams' series of stress function used in the Laplace space are presented in the figure for comparison. It is clear that the results with a different series of stress function are quite close and the Deng's series is a little better than the Williams' series. Therefore, the Williams' series for the static case can replace the Deng's series for the transient case in the dynamic analysis directly.

Figure 5.23 shows the variations of the normalised SIFs and the *T*-stresses versus the normalised time $c_0 t/H$ for different ratios of r_0/W. In addition, the results given by the Finite Element Method (ABAQUS) are presented in the same figures for comparison. It is observed that the difference is little, for different ratios of r_0/W. However, in the case of $r_0/W = 0.1$, it gives better results.

5.3 Conclusion

Firstly, the FBM was presented for both elastic materials and FGMs for dynamic analysis. This method which possesses all the advantages of Meshless Method is based on a first order differential matrix, and used for the governing equations in a strong form. The equilibrium equations of partial derivatives can be transferred to a series of algebraic functions by assistance of boundary conditions and connecting conditions for the interface between different blocks. Besides, the Laplace transformation was applied for the time dependent variables. In order to verify the accuracy of this method on dynamic analysis, numerical examples are given for the comparison with analytical results and previous researches. Furthermore, as the order of the partial differentials is evaluated by Lagrange series in the mapping domain, the computational effort is reduced significantly compared with RBM and MLS interpolations.

Secondly, the FBM was proposed to evaluate the *T*-stress of FGMs for dynamic analysis. The strategy of stress field and displacement field was presented in plane strain for the dynamic analysis. The singular core, which connected with the boundaries of the blocks, was applied to describe the stress field near the crack tip. A circular disk of central crack subjected to uniformly distributed stress was calculated by the FBM with Deng's series and William's series as well. High accuracy can be achieved when compare to the results by FEM (ABAQUS).

Chapter 6

Dynamic Analysis of Poroelasticity by Finite Block Method

6.1 Introduction

Recent investigation of poroelasticity material deformation has awakened many researchers' attention due to its significant application in civil and engineering problems. The theory of porous materials was presented by Biot [109] (low-frequency range) and [110] (high-frequency range) for the dynamic study of interaction between fluid flow and solid deformation based on elastic wave. Compared to elastic solid materials, the essential features of poroelasticity materials can be listed as follows:

1) Mechanical behavior. The application of porous materials can maintain the strength and stiffness of the structure, meanwhile reducing the density of the material. This results in a lightweight material.

2) Reflection performance. It is well known that when waves propagate to the interface of two materials, reflection and refraction occurs. Because of the existence of the pores, the possibility of reflection and refraction is increased. This means that the porous materials will have the superior ability in blocking waves involving sound transmission.

3) Permeability and Adsorption. It is controllable for engineers to design desire size pores and organized structure for porous materials with respect to different diameters of

gas or liquid molecule. Therefore, molecular sieves can be produced in term of this performance, such as high efficiency gas separation membrane and reusable special filter devices.

According to the properties above, the poroelasticity has been widely applied in geomechanics [111], hydrology [111], biomechanics [112], tissue mechanics [113] and micromechanics [114]. There applications appear in the literature which generally motivate many researchers for the investigation of porous materials in numerical analysis.

In 1991, Barry [115] found the analytical solutions for a shear flow over a thin deformable porous layer fixed to the wall of a two-dimensional channel with the aid of binary mixture theory, Darcy's law and the assumption of linear elasticity. In 2000, Schanz [116] solved the problems of transient wave propagation in porous materials for one dimensional case. By the theory of Biot, Schanz correctly presented the analytical solution in the Laplace transform domain with the simplification of the model for the two compressional waves. In 2009, Xue and Nie [117] proposed the analytical solutions of the Rayleigh-Stokes problem based on a fractional calculus method. A porous half-space containing the second-grade fluid under thermal compact is calculated. Also, the analytical solutions for a viscous fluid flow inside a deformable porous surface layer which was in a rigid cylinder tube was presented by Wen and Wang [118]. However, it is impossible to successfully obtain the exact solutions for the analysis of porous materials with any geometrical structure and/or under any conditions. Hence, the approximation methods such as FEM, BEM and Meshless Method are required.

It can be trace back to 1972 when Ghaboussi and Wilson [119] first presented the FEM dynamic analysis on poroelastic materials. The theory of Biot was applied for the

development of a Gurtin type variational principle. In 1999, Manfredini [120] proposed a finite element model to simulate the poroelastic solid of rectangular cross-section subjected to cyclic axial and bending load for the evaluation of bone behaviors. The accuracy of the FEM for poroelastic materials can be verified by the comparison with previous publications related to the pressure distribution of the pores along the z axis. Besides, in 2007, Zyserman [121] introduced the numerical dispersion properties of FEM for the analysis of the equations for the motion of the fluid at low frequency in the porous materials which were based on the theory of Biot. A nonconforming rectangular element was applied for the discretization of the displacement field in solid phase, and the Raviart-Thomas-Nedelec mixed finite element space of zero order was employed for the fluid phase. Also, in 2016, Lee [122] proposed a hybrid modelling technique for the dynamic process of poroelastic materials by the combination of FEM and Wave Based Method (WBM). The porous domain containing the viscous fluid was based on the theory of Biot which separated into two groups depended on the geometry and the boundary conditions. The FEM was utilized for the analysis of complex domain and/or boundary conditions with a large number of small elements, while the WBM was employed for the calculation of regular domains with several wave-based subdomains.

As for the BEM, it was Brady [123] in 1978 who applied this method to determine the stresses and displacements distribution along the long opening with arbitrary orientation in a triaxial stress field. Furthermore, in 1994, Abousleiman [124] represented the BEM for steady and unsteady Stokes flow in two and three dimensions. For the steady flow, the inertial force was eliminated while for unsteady flow, a local acceleration term was adopted in the equilibrium equations. This method was extended to the problems of poroelasticity in three dimensions by Schanz [125] in 2001. The

Convolution Quadrature Method (CQM) was used for the simulation of dynamic behavior of porous materials in term of Laplace transformed fundamental solution and a linear multistep method. Also, Pryl and Schanz [126] applied the BEM to the simulation of wave propagation phenomena in porous materials with the assistance of CQM. The bulk of their work was the improvement of mixed elements, i.e. the shape functions for the porous pressure were dissimilar as for the displacement. The accuracy and convergence of this method for dynamic analysis was introduced by numerical results. As for large-scale analysis, it was Park [127] in 2002, who proposed the particular integral formulations for two- and three-dimensional soil consolidation in conjunction with the theory of Biot and the global shape functions.

Although the FEM and BEM have evolved to be the numerical methods with high accuracy and efficiency for the analysis of poroelasticity, there is still a growing demand in the development of new advance methods for high adaptivity and low programming effort, such as Meshless Method. In 2001, the improved Point Interpolation Method (PIM) was applied for the evaluation of displacement field and pore water pressure in porous materials based on the theory of Biot by Wang [128]. The physical domain was discretized by a cluster of scattered points by PIM technique, while the time domain was computed by Crank-Nicholson's integration method. The next year, Wang [129] presented a radial point interpolation method instead of a polynomial basis function to avoid the singularity generated by the construction of shape functions subjected to unstructured domains. Both Multiquadric basis (MQ) and Gaussian basis were investigated by the numerical results with the comparison of the finite element solutions. Moreover, in 2007, Ferronato [130] introduced the Meshless local Petrov-Galerkin (MLPG) method for the calculation of poroelasticity on the physical domain symmetric

along the axis. The influence of several numerical parameters was investigated, including the optimal size of the local sub-domain for the weak form and the appropriate integration rule, as well as the linear system solver. In 2010, Wen [131] proposed this MLPG method derived from the radial basis function (RBF) on the problems of wave propagation in 3D poroelastic solids. The time dependent variables for the transient dynamic analysis were transferred by the Laplace parameter, while the displacement for the solid skeleton and the pore pressure were discretized by the local boundary integral equations.

In this Chapter, the FBM is applied for wave propagation in two- and three-dimensional problems in poroelasticity. To demonstrate the accuracy of the present method, a one-dimensional analytical solution has been derived for comparison. Several numerical examples are presented for various poroelastic materials subjected to dynamic loads and satisfactory agreements have been achieved.

6.2 Formula of Poroelasticity by FBM

By the theory of Biot, the water pressure of the pores works as the resistance to the mechanical load. The constitutive equations are as follows

$$\begin{aligned} &\sigma_{ij} = \sigma_{ij}^{s} - \alpha\delta_{ij} p, \\ &\sigma_{ij}^{s} = G(u_{i,j} + u_{j,i}) + (K - \frac{2}{3}G)u_{k,k}\delta_{ij} \end{aligned} \tag{6.1}$$

where G represents shear modulus, K is compression modulus, α denotes one of Biot's effective stress coefficient, p is the pore pressure, σ_{ij}^{s} is the stress in the skeleton of the solid, $i, j, k = x, y$ for two dimensions; x, y, z for three dimensions. The variation of fluid volume per unit reference volume ζ is given as

$$\zeta = \alpha u_{k,k} + \frac{\varphi}{R} p \tag{6.2}$$

where $\varphi = \frac{V_f}{V}, V_f$ the volume of the interconnected pores contained in a sample of bulk volume V, R is one of the Biot's coefficient parameter.

By the balance of mass, one can obtain that

$$\frac{\partial \zeta}{\partial t} + q_{i,i} = a, \quad q_i = \varphi \frac{\partial v_i}{\partial t} \tag{6.3}$$

here q_i denotes the specific flux, v_i is the relative displacement to solid, a represents a source term.

The equilibrium equations for the dynamic analysis of the solid frame in porous materials are given as

$$\sigma_{ij,j} + f_i = \rho \frac{\partial^2 u_i}{\partial t^2} + \varphi \rho_f \frac{\partial^2 v_i}{\partial t^2} \tag{6.4}$$

where f_i is the body force per unit volume, $\rho = (1-\varphi)\rho_s + \varphi \rho_f$, in which ρ_s is density of solid, ρ_f is density of fluid.

Moreover, by the application of a generalized Darcy's law, the specific flux is

$$q_i = -\kappa (p_{,i} + \rho_f \frac{\partial^2 u_i}{\partial t^2} + \frac{\rho_a + \varphi \rho_f}{\varphi} \frac{\partial^2 v_i}{\partial t^2}) \tag{6.5}$$

where κ is the permeability, $\rho_a = C \varphi \rho_f, C = 0.66$.

By applying the Laplace transform and vanishing initial conditions for u_i and v_i on Eq. (6.3), one obtains

$$\tilde{v}_i = -\frac{\beta}{s^2 \varphi \rho_f} (\tilde{p}_{,i} + s^2 \rho_f \tilde{u}_i), \tag{6.6}$$

where

$$\beta = \frac{\kappa\rho_f\varphi^2 s}{\varphi^2 + s\kappa(\rho_a + \varphi\rho_f)},$$

in which the initial conditions $u_i|_{t=0} = 0$, and s indicate the Laplace transform parameter and

$$\tilde{F}(\mathbf{x}, s) = \int_0^\infty e^{-st} F(\mathbf{x}, t) dt \tag{6.7}$$

Consequently, the general equations for the displacement $\tilde{u}_i$ and the pore pressure $\tilde{p}$ can be attained as

$$\begin{aligned} &\sigma^s_{ij,j} - (\alpha - \beta)\tilde{p}_{,i} - s^2(\rho - \beta\rho_f)\tilde{u}_i + \tilde{f}_i = 0, \\ &\frac{\beta}{s\rho_f}\tilde{p}_{,ii} - \frac{\phi^2 s}{R}\tilde{p} - (\alpha - \beta)s\tilde{u}_{i,i} + \tilde{a} = 0. \end{aligned} \tag{6.8}$$

The boundary conditions are as follows

$$\begin{aligned} &\tilde{u}_i = \tilde{u}_i^0 \text{ on } \Gamma_u, \\ &\sigma^s_{ij} n_j = \tilde{t}_i^0 \text{ on } \Gamma_t \end{aligned} \tag{6.9}$$

for the solid skeleton, and

$$\begin{aligned} &\tilde{p} = \tilde{p}^0 \text{ on } \Gamma_p, \\ &\tilde{q}_i n_j = \tilde{q}^o \text{ on } \Gamma_q \end{aligned} \tag{6.10}$$

for pore fluid with the initial condition defined as

$$u_i|_{t=0} = 0,\ v_i|_{t=0} = 0,\ p|_{t=0} = 0. \tag{6.11}$$

By substituting Eq. (6.1) to Eq. (6.8), and rewrite as

$$
\begin{aligned}
&G\left(\frac{\partial^2 \tilde{u}_x}{\partial x^2}+\frac{\partial^2 \tilde{u}_x}{\partial y^2}+\frac{\partial^2 \tilde{u}_x}{\partial z^2}\right)+\left(K+\frac{1}{3}G\right)\left(\frac{\partial^2 \tilde{u}_x}{\partial x^2}+\frac{\partial^2 \tilde{u}_y}{\partial x \partial y}+\frac{\partial^2 \tilde{u}_z}{\partial x \partial z}\right)\\
&-(\alpha-\beta)\frac{\partial \tilde{p}}{\partial x}-s^2(\rho-\beta\rho_f)\tilde{u}_x=0,\\
&G\left(\frac{\partial^2 \tilde{u}_y}{\partial x^2}+\frac{\partial^2 \tilde{u}_y}{\partial y^2}+\frac{\partial^2 \tilde{u}_y}{\partial z^2}\right)+\left(K+\frac{1}{3}G\right)\left(\frac{\partial^2 \tilde{u}_x}{\partial x \partial y}+\frac{\partial^2 \tilde{u}_y}{\partial y^2}+\frac{\partial^2 \tilde{u}_z}{\partial y \partial z}\right)\\
&-(\alpha-\beta)\frac{\partial \tilde{p}}{\partial y}-s^2(\rho-\beta\rho_f)\tilde{u}_y=0,\\
&G\left(\frac{\partial^2 \tilde{u}_z}{\partial x^2}+\frac{\partial^2 \tilde{u}_z}{\partial y^2}+\frac{\partial^2 \tilde{u}_z}{\partial z^2}\right)+\left(K+\frac{1}{3}G\right)\left(\frac{\partial^2 \tilde{u}_x}{\partial x \partial z}+\frac{\partial^2 \tilde{u}_y}{\partial y \partial z}+\frac{\partial^2 \tilde{u}_z}{\partial z^2}\right)\\
&-(\alpha-\beta)\frac{\partial \tilde{p}}{\partial z}-s^2(\rho-\beta\rho_f)\tilde{u}_z=0,\\
&\frac{\beta}{s\rho_f}\left(\frac{\partial^2 \tilde{p}}{\partial x^2}+\frac{\partial^2 \tilde{p}}{\partial y^2}+\frac{\partial^2 \tilde{p}}{\partial z^2}\right)-\frac{\varphi^2 s}{R}\tilde{p}-(\alpha-\beta)s\left(\frac{\partial \tilde{u}_x}{\partial x}+\frac{\partial \tilde{u}_y}{\partial y}+\frac{\partial \tilde{u}_z}{\partial z}\right)=0,
\end{aligned}
\tag{6.12}
$$

where

$$
\beta=\frac{\kappa\rho_f\varphi^2 s}{\varphi^2+s\kappa(\rho_a+\varphi\rho_f)}.
$$

The problems of poroelasticity can be scaled with the reference parameters shown in Eq. (6.12), all geometrical and physical quantities can be non-dimensionalised as follows

$$
\begin{aligned}
&\tilde{u}_x^*=\frac{\tilde{u}_x E}{L\sigma_0},\tilde{u}_y^*=\frac{\tilde{u}_y E}{L\sigma_0},\tilde{u}_z^*=\frac{\tilde{u}_z E}{L\sigma_0},x^*=\frac{x}{L},y^*=\frac{y}{L},z^*=\frac{z}{L},\\
&G^*=\frac{G}{E},K^*=\frac{K}{E},R^*=\frac{R}{E},\tilde{p}^*=\frac{\tilde{p}}{\sigma_0},\quad \rho_f^*=\frac{\rho_f}{\rho},\\
&\rho_a^*=\frac{\rho_a}{\rho},s^*=\frac{sL}{\sqrt{E/\rho}},\kappa^*=\frac{\kappa\sqrt{E\rho}}{L},
\end{aligned}
\tag{6.13}
$$

in which L indicates the unit length, E is the Young's Modulus, σ_0 is applied stress. Then the equilibrium equations with non-dimensional parameters are obtained as

$$
\begin{aligned}
&G^*\left(\frac{\partial^2\tilde{u}_x^*}{\partial x^{*2}}+\frac{\partial^2\tilde{u}_x^*}{\partial y^{*2}}+\frac{\partial^2\tilde{u}_x^*}{\partial z^{*2}}\right)+\left(K^*+\frac{1}{3}G^*\right)\left(\frac{\partial^2\tilde{u}_x^*}{\partial x^{*2}}+\frac{\partial^2\tilde{u}_y^*}{\partial x^*\partial y^*}+\frac{\partial^2\tilde{u}_z^*}{\partial x^*\partial z^*}\right)\\
&-(\alpha-\beta)\frac{\partial\tilde{p}^*}{\partial x^*}-s^{*2}(\rho-\beta\rho_f^*)\tilde{u}_x^*=0,\\
&G^*\left(\frac{\partial^2\tilde{u}_y^*}{\partial x^{*2}}+\frac{\partial^2\tilde{u}_y^*}{\partial y^{*2}}+\frac{\partial^2\tilde{u}_y^*}{\partial z^{*2}}\right)+\left(K^*+\frac{1}{3}G^*\right)\left(\frac{\partial^2\tilde{u}_x^*}{\partial x^*\partial y^*}+\frac{\partial^2\tilde{u}_y^*}{\partial y^{*2}}+\frac{\partial^2\tilde{u}_z^*}{\partial y^*\partial z^*}\right)\\
&-(\alpha-\beta)\frac{\partial\tilde{p}^*}{\partial y^*}-s^{*2}(\rho-\beta\rho_f^*)\tilde{u}_y^*=0,\\
&G^*\left(\frac{\partial^2\tilde{u}_z^*}{\partial x^{*2}}+\frac{\partial^2\tilde{u}_z^*}{\partial y^{*2}}+\frac{\partial^2\tilde{u}_z^*}{\partial z^{*2}}\right)+\left(K^*+\frac{1}{3}G^*\right)\left(\frac{\partial^2\tilde{u}_x^*}{\partial x^*\partial z^*}+\frac{\partial^2\tilde{u}_y^*}{\partial y^*\partial z^*}+\frac{\partial^2\tilde{u}_z^*}{\partial z^{*2}}\right)\\
&-(\alpha-\beta)\frac{\partial\tilde{p}^*}{\partial z^*}-s^{*2}(\rho-\beta\rho_f^*)\tilde{u}_z^*=0,\\
&\frac{\beta}{s^*\rho_f^*}\left(\frac{\partial^2\tilde{p}^*}{\partial x^{*2}}+\frac{\partial^2\tilde{p}^*}{\partial y^{*2}}+\frac{\partial^2\tilde{p}^*}{\partial z^{*2}}\right)-\frac{\varphi^2 s^*}{R^*}\tilde{p}^*-(\alpha-\beta)s^*\left(\frac{\partial\tilde{u}_x^*}{\partial x^*}+\frac{\partial\tilde{u}_y^*}{\partial y^*}+\frac{\partial\tilde{u}_z^*}{\partial z^*}\right)=0,
\end{aligned}
\tag{6.14}
$$

where

$$\beta=\frac{\kappa^*\rho_f^*\varphi^2 s^*}{\varphi^2+s^*\kappa^*(\rho_a^*+\varphi\rho_f^*)}.$$

By applying the FBM, the equilibrium Eq. (6.12) can be given as

$$
\begin{aligned}
&[(K^* + \frac{4}{3}G^*)\mathbf{D}_\mathbf{x}\mathbf{D}_\mathbf{x} + G^*\mathbf{D}_\mathbf{y}\mathbf{D}_\mathbf{y} + G^*\mathbf{D}_\mathbf{z}\mathbf{D}_\mathbf{z}]\tilde{\mathbf{u}}_\mathbf{x}^* + (K^* + \frac{1}{3}G^*)\mathbf{D}_\mathbf{x}\mathbf{D}_\mathbf{y}\tilde{\mathbf{u}}_\mathbf{y}^* + \\
&(K^* + \frac{1}{3}G^*)\mathbf{D}_\mathbf{x}\mathbf{D}_\mathbf{z}\tilde{\mathbf{u}}_\mathbf{z}^* - (\alpha - \beta)\mathbf{D}_\mathbf{x}\tilde{p}^* - s^{*2}(\rho - \beta\rho_f^*)\tilde{\mathbf{u}}_\mathbf{x}^* = 0, \\
&(K^* + \frac{1}{3}G^*)\mathbf{D}_\mathbf{x}\mathbf{D}_\mathbf{y}\tilde{\mathbf{u}}_\mathbf{x}^* + [G^*\mathbf{D}_\mathbf{x}\mathbf{D}_\mathbf{x} + (K^* + \frac{4}{3}G^*)\mathbf{D}_\mathbf{y}\mathbf{D}_\mathbf{y} + G^*\mathbf{D}_\mathbf{z}\mathbf{D}_\mathbf{z}]\tilde{\mathbf{u}}_\mathbf{y}^* + \\
&(K^* + \frac{1}{3}G^*)\mathbf{D}_\mathbf{y}\mathbf{D}_\mathbf{z}\tilde{\mathbf{u}}_\mathbf{z}^* - (\alpha - \beta)\mathbf{D}_\mathbf{y}\tilde{\mathbf{p}}^* - s^{*2}(\rho - \beta\rho_f^*)\tilde{\mathbf{u}}_\mathbf{y}^* = 0, \\
&(K^* + \frac{1}{3}G^*)\mathbf{D}_\mathbf{x}\mathbf{D}_\mathbf{z}\tilde{\mathbf{u}}_\mathbf{x}^* + (K^* + \frac{1}{3}G^*)\mathbf{D}_\mathbf{y}\mathbf{D}_\mathbf{z}\tilde{\mathbf{u}}_\mathbf{y}^* + [G^*\mathbf{D}_\mathbf{x}\mathbf{D}_\mathbf{x} + G^*\mathbf{D}_\mathbf{y}\mathbf{D}_\mathbf{y} + \\
&(K^* + \frac{4}{3}G^*)\mathbf{D}_\mathbf{z}\mathbf{D}_\mathbf{z}]\tilde{\mathbf{u}}_\mathbf{z}^* - (\alpha - \beta)\mathbf{D}_\mathbf{z}\tilde{\mathbf{p}}^* - s^{*2}(\rho - \beta\rho_f^*)\tilde{\mathbf{u}}_\mathbf{z}^* = 0, \\
&-(\alpha - \beta)s^*(\mathbf{D}_\mathbf{x}\tilde{\mathbf{u}}_\mathbf{x}^* + \mathbf{D}_\mathbf{y}\tilde{\mathbf{u}}_\mathbf{y}^* + \mathbf{D}_\mathbf{z}\tilde{\mathbf{u}}_\mathbf{z}^*) + \frac{\beta}{s^*\rho_f^*}(\mathbf{D}_\mathbf{x}\mathbf{D}_\mathbf{x} + \mathbf{D}_\mathbf{y}\mathbf{D}_\mathbf{y} \\
&+ \mathbf{D}_\mathbf{z}\mathbf{D}_\mathbf{z})\tilde{\mathbf{p}}^* - \frac{\varphi^2 s^*}{R^*}\tilde{\mathbf{p}}^* = 0,
\end{aligned}
\tag{6.15}
$$

in which $\mathbf{D}_\mathbf{x}, \mathbf{D}_\mathbf{y}, \mathbf{D}_\mathbf{z}$ are the coefficient differential matrix derived from the Lagrange Interpolation Method and the Mapping Technology in the FBM for three dimensional problems.

6.3 Analytical Solutions in One Dimensional Problems

To demonstrate the accuracy of the FBM on the problems for porous materials, the analytical solutions for one dimension is obtained in this section for comparison. The material properties $G = E/2, K = E/3$, where E is Young's modulus, in this case, $E = 1$ for simplification. The rest of the material properties are listed as example 1 or 2 for comparison with the results by the FBM. The governing equations for one dimensional problems on poroelasticity are given as

$$
\begin{aligned}
&E\frac{\partial^2\tilde{u}}{\partial x^2}-(\alpha-\beta)\frac{\partial\tilde{p}}{\partial x}-s^2(\rho-\beta\rho_f)\tilde{u}=0,\\
&\frac{\beta}{s\rho_f}\frac{\partial^2\tilde{p}}{\partial x^2}-\frac{\varphi^2 s}{R}\tilde{p}-(\alpha-\beta)\frac{\partial\tilde{u}}{\partial x}=0.
\end{aligned}
\tag{6.16}
$$

Therefore, one has

$$
(\frac{\partial\tilde{p}}{\partial x}-s\lambda_1\tilde{p})(\frac{\partial\tilde{p}}{\partial x}-s\lambda_2\tilde{p})(\frac{\partial\tilde{p}}{\partial x}-s\lambda_3\tilde{p})(\frac{\partial\tilde{p}}{\partial x}-s\lambda_4\tilde{p})=0, \tag{6.17}
$$

where λ_k are four roots of the following equation:

$$
\eta_4\lambda^4-\eta_2\lambda^2+\eta_0=0, \tag{6.18}
$$

here

$$
\eta_4=\frac{E\beta}{\rho_f(\alpha-\beta)},\eta_2=\frac{E\varphi^2}{R(\alpha-\beta)}+(\alpha-\beta)+\frac{(\rho-\beta\rho_f)\beta}{(\alpha-\beta)\rho_f},\eta_0=\frac{(\rho-\beta\rho_f)\varphi^2}{(\alpha-\beta)R}. \tag{6.19}
$$

The displacement $\tilde{u}$ can be attained by

$$
u=\beta_1\frac{\partial^3\tilde{p}}{\partial x^3}+\beta_2\frac{\partial\tilde{p}}{\partial x}, \tag{6.20}
$$

where

$$
\beta_1=\frac{E\beta}{s^4\rho_f(\rho-\beta\rho_f)(\alpha-\beta)},\ \beta_2=-\frac{1}{s^2(\rho-\beta\rho_f)}[\frac{E\varphi^2}{R(\alpha-\beta)}+(\alpha-\beta)]. \tag{6.21}
$$

The pressure and displacement distribution for one dimensional porous materials can be obtained as

$$
\tilde{p}(x)=\sum_{k=1}^{4}A_k e^{\lambda_k sx},\ \tilde{u}(x)=\sum_{k=1}^{4}(\beta_1 s^2\lambda_k^2+\beta_2)A_k\lambda_k s e^{\lambda_k sx}. \tag{6.22}
$$

Then the flux and stress can be obtained as

$$\tilde{q}(x) = -\frac{\beta}{s\rho_f}\sum_{k=1}^{4}[1+\rho_f s^2(\beta_1 s^2\lambda_k^2+\beta_2)]A_k\lambda_k s e^{\lambda_k s x},$$
$$\tilde{\sigma} = E\sum_{k=1}^{4}(\beta_1 s^2\lambda_k^2+\beta_2)A_k\lambda_k^2 s^2 e^{\lambda_k s x}. \tag{6.23}$$

To determine the four unknown coefficients A_k, the boundary conditions are given as follows

$$\tilde{u}(0)=0, \tilde{q}(0)=0, \tilde{p}(l)=0, \tilde{\sigma}(l)=\tilde{\sigma}^0. \tag{6.24}$$

By applying the boundary conditions in Eq. (6.24), A_k can be obtained from

$$\begin{aligned}
&\sum_{k=1}^{4}(\beta_1 s^2\lambda_k^2+\beta_2)A_k\lambda_k s = 0,\\
&\sum_{k=1}^{4}\lambda_k A_k = 0,\\
&\sum_{k=1}^{4}e^{\lambda_k s l}A_k = 0,\\
&\sum_{k=1}^{4}(\beta_1 s^2\lambda_k^2+\beta_2)A_k\lambda_k^2 s^2 e^{\lambda_k s x} = \tilde{\sigma}^0/E.
\end{aligned} \tag{6.25}$$

in which $\tilde{\sigma}^0$ is the Heaviside function applied at the top of the physical domain.

6.4 Numerical Examples

A. A square plate for dynamic analysis in poroelastic materials (rock)

Consider a square plate of porous materials with zero initial displacement and strain subjected to impact load shown in Figure 6.1. The properties of the materials in this example are identical to the ones in Wen [131] for comparisons shown as $K=8\times10^9(N/m^2)$, $G=6\times10^9(N/m^2)$, $\rho=2458(kg/m^3)$, $\rho_f=1000(kg/m^3)$, $\varphi=0.19$,

$R = 4.7\times10^{8}(N/m^{2})$, $\alpha = 0.867$, $\kappa = 1.9\times10^{-10}(m^{4}/Ns)$. The dimensions are selected as $h = 3, w = 1$. The boundaries of the plate are assumed to be rigid, frictionless and impermeable. The boundary conditions are given as

$$\begin{aligned} &u_x = t_y = q = 0, && x = 0 \text{ and } w \\ &u_y = t_x = q = 0, && y = 0 \\ &t_x = p = 0, t_y = -\sigma_0 H(t), && y = h \end{aligned} \tag{6.26}$$

in which $\sigma_0 = 1$.

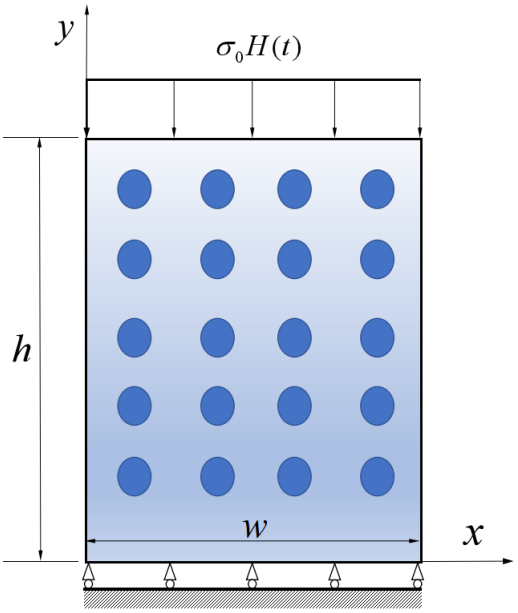

Figure 6.1 A square plate of porous materials under impact loads

In this case, the constants of the material are those of rock (Berea sandstone) as shown above exclusive of the Possion's ratio to be zero in this example for the comparison with the analytical results. The velocities of the fast wave are $1.2968\,c_0$ and $0.3975\,c_0$, respectively, in which $c_0 = \sqrt{E/\rho} = 2420$. For the analysis of the FBM, the number of node $N_x = 9$ and $N_y = 7,9,11$ respectively to confirm the convergence of

this method on poroelasticity. Two free parameters for the inverse of Laplace transformation domain are used as $w = 5/T_0$ and $T_0 = 60$. The number of sample point in the Laplace domain is given as $L = 25$. The displacement at points $P_{top}(0.5,3)$ and $P_{mid}(0.5,1.5)$ are plotted in Figure 6.2 and Figure 6.3 against normalized time. The time dependent pressure is shown in Figure 6.4 at the bottom of the plate $P_{bottom}(0.5,0)$ varying with normalized time.

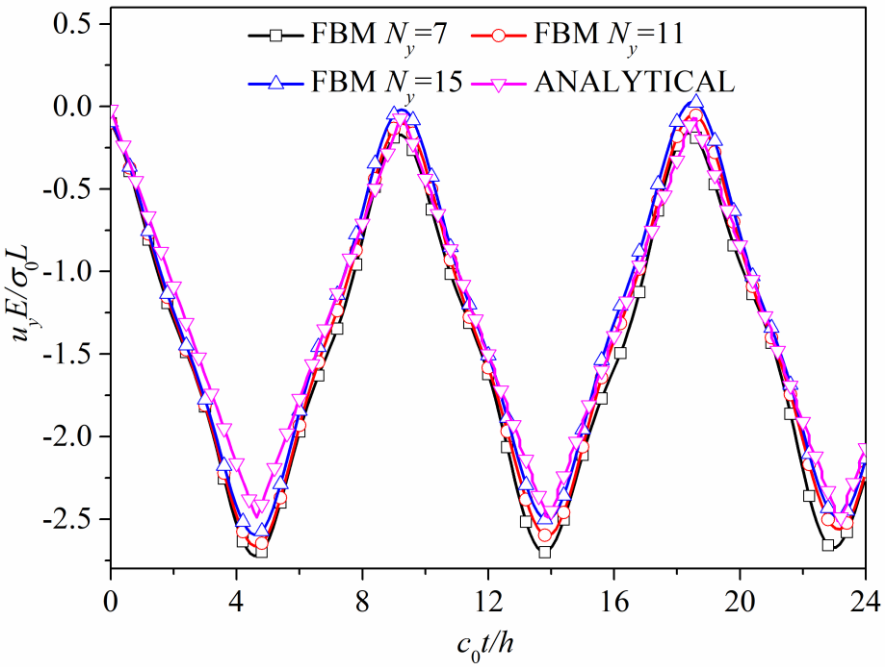

Figure 6.2 The normalized displacement at point $p_{top}(0.5,3)$.

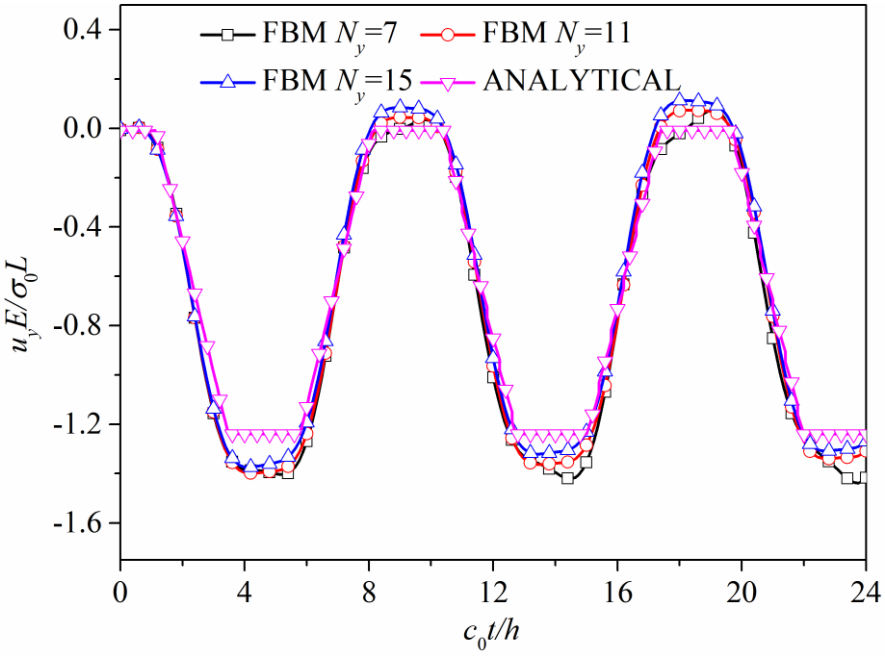

Figure 6.3 The normalized displacement at point $p_{mid}(0.5,1.5)$.

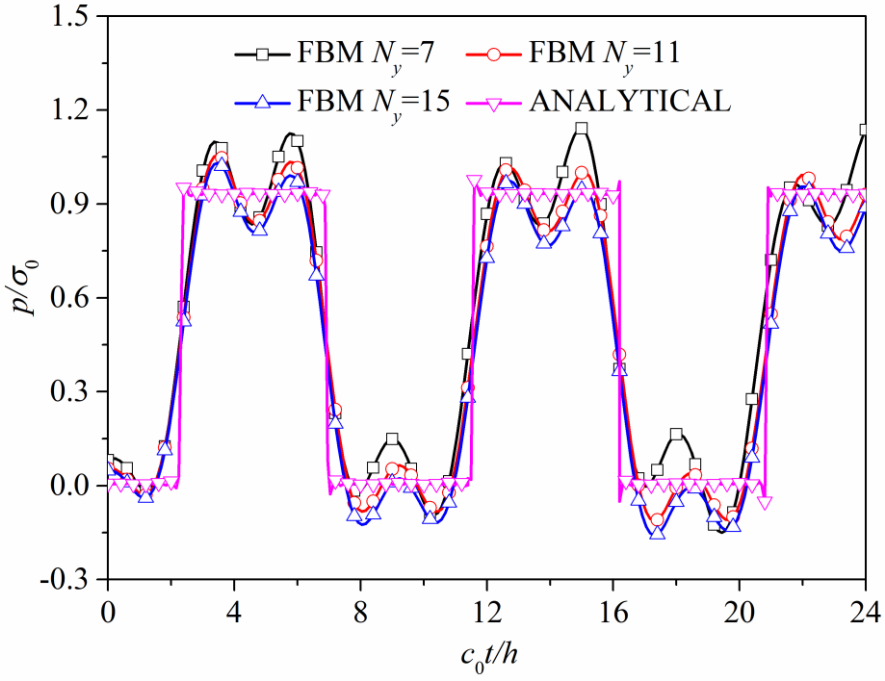

Figure 6.4 The normalized pressure at point $p_{bottom}(0.5,0)$.

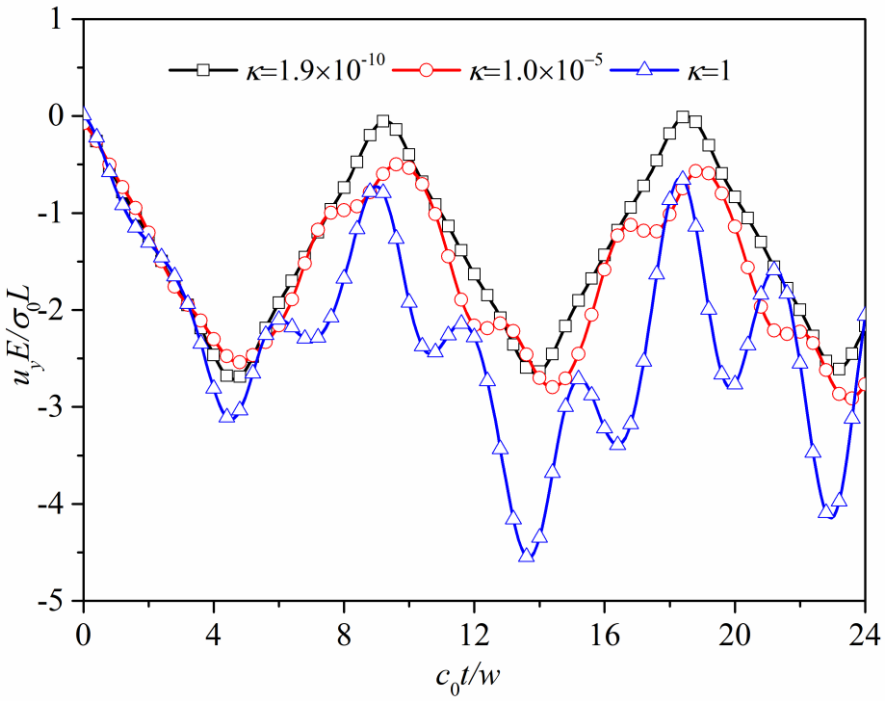

Figure 6.5 The normalized displacement at point $p_{top}(0.5,3)$.

It is noticeable that the arrival of the first wave (fast) at the bottom causes the step jump at $h/1.2968 = 2.3135$. The second jump is caused by the arrival of the first fast wave starting from the top, reflecting from the bottom, and then reflecting back from the top again, i.e., the arrival time should be $3\times 2.3135 = 6.94$. This wave is of negative amplitude and cancels exactly the first wave both for the pressure and stress as shown in Figure 6.2-6.4. In addition, the influence of the permeability κ is illustrated in Figure 6.5. The displacement is slightly decrease as the increasing of the permeability. However, it is hard to tell the law of the wave propagation in this case.

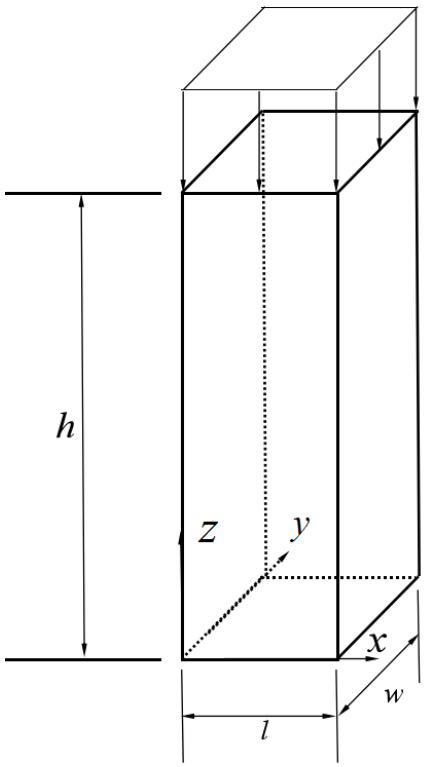

Figure 6.6 3D poroelastic rod under pressure.

A rod for dynamic analysis in poroelastic materials (soil) in 3D

Assume a poroelastic rod with the same initial conditions in the previous example for dynamic analysis shown in Figure 6.6. The geometry of the physical domain are $l = w = 1, h = 3.$ The constants of the material (soil) are selected as $K = 2.1\times10^{8}(N/m^{2}),$ $G = 9.8\times10^{7}(N/m^{2}),$ $\rho = 1884(kg/m^{3}),$ $\rho_{f} = 1000(kg/m^{3}),$ $\varphi = 0.48,$ $R = 1.2\times10^{9}(N/m^{2}),$ $\alpha = 0.981,$ $\kappa = 3.55\times10^{-9}(m^{4}/Ns).$ The boundary conditions are given as

$$\begin{aligned}
&u_x = t_y = t_z = q = 0, && x = 0,1,\\
&u_y = t_x = t_z = q = 0, && y = 0,1,\\
&u_z = t_x = t_y = q = 0, && z = 0,\\
&t_x = t_y = p = 0, t_z = -\sigma_0 H(t), && z = 3.
\end{aligned} \tag{6.27}$$

Some computational procedures have been carried out for soil in this case. However, for the comparison with the analytical results, the Poisson's ratio is considered as zero, thus, the shear modulus $G = E/3$ and bulk modulus $K = E/2$. Then the velocities of fast wave and slow wave are $4.8128\,c_0$ and $0.7476\,c_0$, respectively. Two free parameters for the inverse of Laplace transformation domain are used as $\eta = 5/T_0$ and $T_0/t_0 = 40$. The number of sample point in the Laplace domain is given as $L = 25$. The total number is $M = N_x \times N_y \times N_z$, in which $N_x = N_y = 5$, and $N_z = 11,13,15$ respectively. The displacement at points $P_{top}(0.5,3)$ is plotted in Figure 6.7 against normalized time. The time dependent pressure is shown in Figure 6.8 at the bottom of the plate $P_{bottom}(0.5,0)$ varying with normalized time.

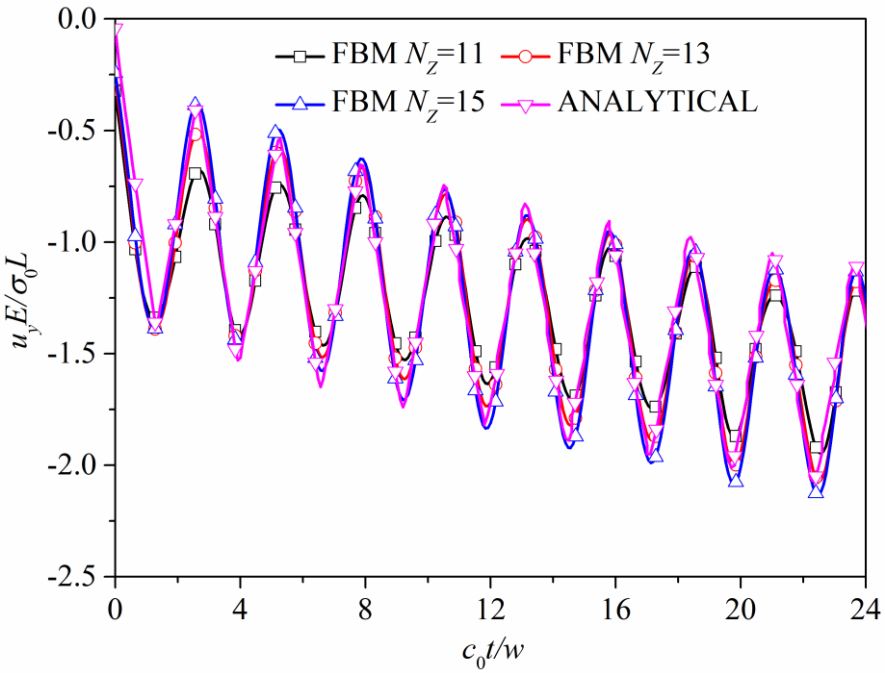

Figure 6.7 The normalized displacement at point $p_{top}(0.5,3)$.

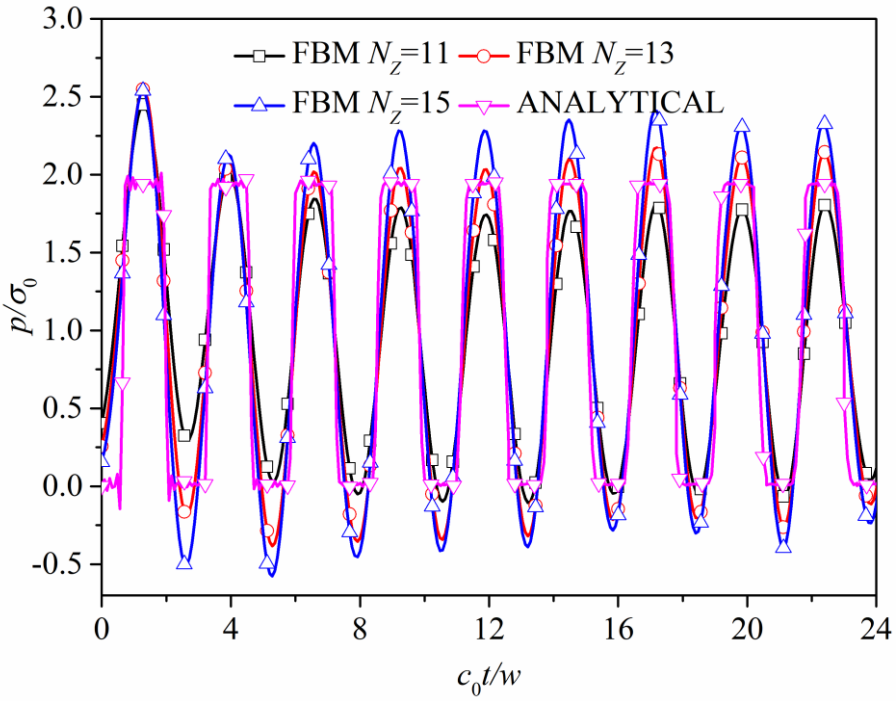

Figure 6.8 The normalized pressure at point $p_{bottom}(0.5,0)$.

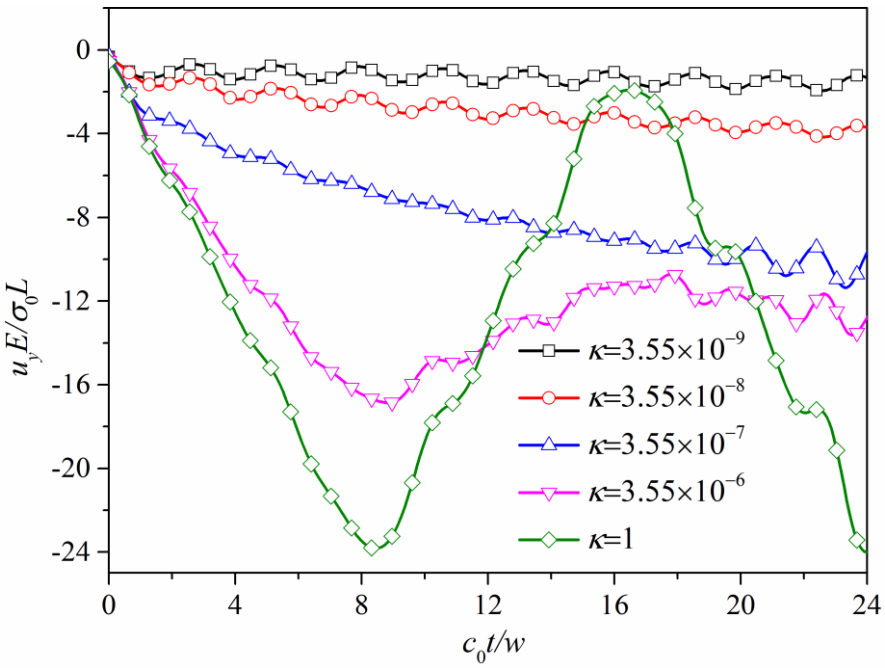

Figure 6.9 The normalized displacement at point $p_{top}(0.5,3)$.

The arrival time for the first wave at the bottom is $3/4.8128 = 0.623$ and then the arrival time for the second jump is at $0.623 \times 3 = 1.869$. For the purpose of comparison, in Figure 6.2, it is obviously that the displacement at the top of the column under impact load fluctuate around a constant value, while in Figure 6.7, the amplitude of displacement, lose its power to go back to the origin position due to fluid viscous dissipation. As the soil column is being drained, the time for the wave to transverse the column will gradually increase. Furthermore, the influence of the permeability κ is also calculated in Figure 6.9. It illustrates that as the permeability raises, the normalized displacement at the top of the column increase. For this type of materials, when permeability is large enough, there is a wave can be observed clearly in Figure 6.9.

6.5 Conclusion

In this Chapter, the FBM has been applied to both 2D and 3D problems in porous materials for dynamic analysis. The physical domain can be divided into several sub-domains in the FBM for complex structure, and these sub-domains can be computed by the corresponding normalized domain which can be defined by 8 seeds in 2D problems or 20 seeds in 3D problems. A series of algebraic functions can be constructed from equilibrium equations based on Biot's theory by the FBM with the applied boundary conditions and initial conditions. The Laplace transformation domain is utilized for the time dependent variables. The analytical solutions for one dimensional problem is obtained for the reason of comparison. The displacement and pressure for two different porous materials (rock and soil) are introduced in the numerical examples. The influence of the permeability has been evaluated. Compare to the analytical solution of 1D case, the results obtained by the FBM are acceptable when the number of

nodes N=11. The influence of permeability was discussed, as for the soil case, a peak of the displacement can be observed clearly when the permeability increases.

Chapter 7

Conclusions and Perspective

7.1 Summery of the Thesis

The bulk of this work is mainly focus on the investigation of FBM method for the mechanical properties of functionally graded materials for both static and dynamic problems. Cracks, inevitably exist in all type of structures, may propagation in some specified conditions and cause the failure of the structures. Therefore, the evaluation of cracks in functionally graded materials is also introduced in this thesis. Several factors that would affect the performance of the crack are discussed in the chapters above, including the length of the crack, the geometry of the physical domain and the applied stress et al. Moreover, the mechanical properties of the porous materials are also proposed in one of the chapters due to the high attentions by the researchers. The following conclusions in details can be obtained for each chapter:

In Chapter 3, the basic functions of the Finite Block Method were presented which based on a first order derivative matrix derived from the Lagrange interpolation method. By the application of a uniform node distribution or Chebyshev node distribution, the first order differential matrix can be determined by the Lagrange interpolation method. Consequently, the coefficient matrix for different orders can be obtained in a normalized system which based on the first order differential matrix. The physical domain is possible to be mapping into the normalized domain with 8 seeds for 2D and 20 seeds for

3D. The basic functions and strategy of Finite Block Method was presented in this chapter. In the end, to demonstrate the convergence and accuracy of the FBM, a simple function is chosen to compare with the analytical solutions. By the solutions obtained in this chapter, the essential features of the FBM can be summarized as follows:

The physical domain can be divided into several sub-blocks, and each block can be mapping into a normalized domain. In addition, the different orders of derivatives can be attained by a first order differential matrix derived from the Lagrange Interpolation Method in normalized domain. Moreover, the convergence and accuracy of the FBM is approved.

In Chapter 4, the Finite Block Method was proposed to analysis the stress intensity factors and *T*-stress for crack problems on both isotropic and anisotropic FGMs. The finite block method was introduced to formulate equations for static analysis of FGMs. The Stress Intensity Factors are calculated by Crack Opening Displacement for both isotropic and orthotropic FGMs. Several numerical examples are computed for static analysis of crack problems in two dimensions. To verify the accuracy of the FBM on the static analysis of FGMs, the results by FEM (ABAQUS) is adopted for comparison.

The normalized stress intensity factors were calculated for various material properties. From the results, as the increasing of Young's modulus, the normalized stress intensity factors were decrease. As for the *T*-stress, a singular core was applied to combine with the Finite Block Method for the calculation. Besides, the William's series was used for the description of stress field around the crack tip. For the reason of convenience, the number of node along the boundary of the blocks is chosen to be the same as the number of the truncation in Williams' stress function. It can be observed

that the normalized SIFs and *T*-stress can be attained with high accuracy by the comparison of FEM (ABAQUS).

In Chapter 5, the normalized stress intensity factors and T-stress were calculated for both elastic materials and FGMs by the FBM. This method, which possesses all the advantages of Meshless Method, is based on a first order differential matrix, and used for the governing equations in a strong form in this case. The setup of system functions for the FGMs is similar as the materials in elasticity with the aid of boundary conditions and initial conditions for dynamic problems. By the use of the FBM, the governing equations can be transferred to a series of algebraic functions. Moreover, the time dependent variables can be calculated in the Laplace domain with two free parameters. Several numerical examples are given for the accuracy and convergence of the FBM for dynamic analysis of crack problems.

It can be observed that the change of displacement of solid materials when the elastic wave propagates by the contour plot in ABAQUS. The velocity of the elastic wave can be calculated as $c = \sqrt{E / \rho}$, so that it is reasonable, before the arriving of the elastic wave, the stress and displacement keep zero. From the figures obtained, we can see that there is also reflection and superposition of the wave when it reaches the boundaries. Furthermore, as the order of the partial differentials is evaluated by Lagrange series in the mapping domain, the computational effort is reduced significantly compared with RBM and MLS interpolations. The dynamic *T*-stress was evaluated in the second part of this chapter with the assistance of Deng's series or William's series. Similar as the stress intensity factors, the *T*-stress are also calculated in the Laplace domain, and Durbin's inverse Laplace method was applied to transform the variables in Laplace domain to real time domain. It can be noticeable that the results by

these two series were quite close to each other. In addition, the influence of the radius of the singular core was also discussed. And the results showed that the best solution can be attained when $r_0 / W = 0.1$.

In Chapter 6, the mechanical properties of porous materials have been introduced by the FBM in both 2D and 3D problems. The system equations were set up depended on the theory of Biot with the applied boundary conditions and initial conditions. By the application of FBM, the complex structure can be divided into several sub-domains, and the derivatives respect to the spatial coordinate can be transferred to a series of algebraic functions. The Laplace transformation domain is utilized for the time dependent variables. The analytical solutions for one dimensional problem is obtained to verify the accuracy and convergence of the FBM on poroelasticity. The displacement and pressure for two different porous materials (rock and soil) are introduced in the numerical examples. The influence of the permeability has been evaluated.

7.2 Contributions of this work

By the application of the Finite Block Method on FGMs and Porous materials, it can be concluded that:

1. To verify the possibility of the Finite Block Method on the analysis of these types of materials. By the comparison with FEM or analytical result, the accuracy and convergence of the FBM applied on FGMs and Porous materials can be verified. The FBM is proposed for the continuous partial differential equations. Although only limited types of materials have been calculated in this thesis with FBM, the accuracy and convergence of the FBM can be guaranteed on most of the continuous problems.

2. To prove the advantages of the Finite Block Method by the comparison of Finite Element Method (ABAQUS). If the problem domain has been defined, $\mathbf{D}_x$ and $\mathbf{D}_y$ can be identified by a first order differential matrix which is directly derived from the Lagrangian interpolation method. Compare with the FEM (ABAQUS), the results of FBM have the same level of accuracy as the FEM and the CPU cost is reduced.

7.3 Future Work

The investigation in this thesis for the application of the Finite Block Method can be extended to following aspects:

- In the study of Finite Element Method, the triangle elements also play a significant role in the simulation of engineering problems. Therefore, one perspective for the future work would be the investigation of the Finite Block Method based on the normalized triangle domain.
- The Finite Block Method is flexible to combine with other Meshless Method or Boundary Element Method to deal with complex domain. For example, Li and Wen [58] proposed the Finite Block Method with the assistance of Petrov-Galerkin Method for the calculation of problems in heat conduction. In the study of the Finite Block Method in this thesis, only strong form formula is used for the simulations. It has been pointed out that the boundary conditions applied directly to the node may cause singularity, and result in large error especially when dynamic analysis is carried out.

- The bulk of this research is mainly on the analysis of two dimensional problems. The Finite Block Method can calculate problems in three dimensions without any difficulty.
- The Finite Block Method can be applied on all type of materials including poroelasticity. Hence, the utilization of this approach can be extended to other fields such as fluid problems, heat conduction and electromagnetic problems et al.

7.4 List of Publications

[1] Wen P, Li M, Meng L and Shi C (2016), Post buckling analysis for composite plate by finite block Petrov-Galerkin method, European Journal of Mechanics - A/Solids vol.61,443-455.

[2] M. Li, M. Lei, C. Shi, P.H. Wen and M.H. Aliabadi, On the validation of Williams' stress function for dynamic fracture mechanics, Fracture and Damage Mechanics, 2015.

[3] X.J.Huang, C. Chao, P.H. Wen, Finite Block Method and its Applications in Engineering, NUMISHEET, 2016 (Keynote Speech).

[4] Li, J.; Huang, T.; Yue, J. H.; Shi, C.; Wen, P. H., Anti-plane fundamental solutions of functionally graded materials and applications to fracture mechanics. The Journal of Strain Analysis for Engineering Design 2017, 52 (7), 422-433.

[5] Li, M.; Dou, F. F.; Korakianitis, T.; Shi, C.; Wen, P. H., Boundary node Petrov–Galerkin method in solid structures. Computational and Applied Mathematics 2016.

[6] J. Li, C. Shi., P.H. Wen., Numerical Analysis for Cracked Functionally Graded Materials by Finite Block Method, Key Engineering Materials, Vol. 754, pp. 145-148, 2017

References

1. Cho, J.R. and D.Y. Ha, *Averaging and finite-element discretization approaches in the numerical analysis of functionally graded materials.* Materials Science and Engineering: A, 2001. **302**(2): p. 187-196.

2. Atai, A.A., A. Nikranjbar, and R. Kasiri, *Buckling and post-buckling behaviour of semicircular functionally graded material arches: a theoretical study.* Proceedings of the Institution of Mechanical Engineers, Part C: Journal of Mechanical Engineering Science, 2011. **226**(3): p. 607-614.

3. Chin, E.S.C., *Army focused research team on functionally graded armor composites.* Materials Science and Engineering: A, 1999. **259**(2): p. 155-161.

4. Duga, J.J., Fisher,W.H., Buxbaum,R.W., Rosenfield,A.R., Honton,E.J. and McMillan, S.C, *The Economic Effects of Fracture in the United States*. 1983, Washington, DC: NBS Special Publication.

5. Erdogan, F., *Fracture mechanics of functionally graded materials.* Composites Engineering, 1995. **5**(7): p. 753-770.

6. Dolbow, J.E. and M. Gosz, *On the computation of mixed-mode stress intensity factors in functionally graded materials.* International Journal of Solids and Structures, 2002. **39**(9): p. 2557-2574.

7. Kim, J.-H., Paulino, G.H, *Finite element simulation of crack propagation in functionally graded materials under mixed-mode loading.* nternational Journal for Mechanics and Materials in Design, 2004. **1**: p. 63-64.

8. Kim, J.-H. and G.H. Paulino, *Finite element evaluation of mixed mode stress intensity factors in functionally graded materials.* International Journal for Numerical Methods in Engineering, 2002. **53**(8): p. 1903-1935.

9. Wen, P.H., P. Cao, and T. Korakianitis, *Finite Block Method in elasticity.* Engineering Analysis with Boundary Elements, 2014. **46**: p. 116-125.

10. Li, M. and P.H. Wen, *Finite block method for transient heat conduction analysis in functionally graded media.* International Journal for Numerical Methods in Engineering, 2014. **99**(5): p. 372-390.

11. Anderson, T.L., *Fracture Mechenics Fundamentals and Applications.* Taylor & Francis Group, 2005.

12. Griffith, A.A., *The Phenomena of Rupture and Flow in Solids.* Philosophical Transactions of the Royal Society of London. Series A, Containing Papers of a Mathematical or Physical Character, 1921. **221**(582-593): p. 163.

13. Westergaard, H.M.W., *BearingPressures-and-Cracks.* Journal of applied Mechan-ics, 1939.

14. Irwin, G.R., *Onset of Fast Crack Propagation in High Strength Steal and Aluminum Alloys.* sagamore Research Conference Proceedings, 1956. **2**: p. 289-305.

15. Irwin, G.R., *Analysis of Stresses and Strains Near the End of a Crack Traversing a Plate.* J. Appl. Mech., 1957.

16. Irwin, G.R., *Plastic Zone Near a Crack and Fracture Toughness.* sagamore Research Conference Proceedings, 1961. **4**: p. 63-78.

17. Dugdale, D.S., *Yielding of steel sheets containing slits.* Journal of the Mechanics and Physics of Solids, 1960. **8**(2): p. 100-104.

18. Barenblatt, G.I., *The Mathematical Theory of Equilibrium Cracks in Brittle Fracture.* Advances in Applied Mechanics, 1962. **7**: p. 55-129.

19. Wells, A.A., *Unstable Crack Propagation in Metals: Cleavage and Fast Fracture.* Proceedings of the Crack Propagation Symposium, 1961. **1**: p. 84.

20. Rice, J.R. and G.F. Rosengren, *Plane strain deformation near a crack tip in a power-law hardening material.* Journal of the Mechanics and Physics of Solids, 1968. **16**(1): p. 1-12.

21. Hutchinson, J.W., *Singular behaviour at the end of a tensile crack in a hardening material*. Journal of the Mechanics and Physics of Solids, 1968. **16**(1): p. 13-31.

22. Rice, J.R., *A Path Independent Integral and the Approximate Analysis of Strain Concentration by Notches and Cracks.* Journal of Applied Mechanics, 1968. **35**(2): p. 379-386.

23. Begley, J.A.a.L., J.D., *The J-Integral as a Fracture Criterion.* ASTM STP 514, American Society fro Testing and Materials, 1972: p. 1-20.

24. Inglis, C.E., *Stress in a Plate Due to the Presence of Crack and Sharp Corners.* Transactions of the Institute of Naval Architects, 1913. **55**: p. 219-241.

25. Ritz, W., *Über eine Neue Metode zur Lösung gewisser Variationsprobleme der Matematischen Physik.* Journal für die reine und angewandte Mathematik, 1909. **135**.

26. Courant, R., *Variational methods for the solution of problems of equilibrium and vibrations.* Bull. Amer. Math. Soc., 1943. **49**(1): p. 1-23.

27. Clough, R.W., *The finite element method in plane stress analysis.* 1960: p. 345-378.

28. J. H. Argyris D.Sc., S.K.B.S., *Energy Theorems and Structural Analysis*. 1960: Springer US.

29. A Turner, M.C., RW; Martin, HC & Topp, LJ, *Stiffness and Deflection Analysis of Complex Structures.* Journal of the Aeronautical Sciences, 1956. **23**(9): p. 805-823.

30. A., H., *Solution of Problems of Elasticity by the Framework Method.* Journal of Applied Mechanics, 1941. **8**: p. 169-175.

31. O. C. Zienkiewicz, Y.K.C., *The Finite Element Method in Structural and Continuum Mechanics: Numerical Solution of Problems in Structural and Continuum Mechanics*, ed. E.c.e. series. 1967: McGraw-Hill; First ed edition.

32. Gingold, R.A., Monaghan, J. J., *Smoothed particle hydrodynamics: Theory and application to non-spherical stars*. Mon.Not.Roy.Astron.Soc. Vol. 181. 1977.

33. Lucy, L.B., *A numerical approach to the testing of the fission hypothesis.* Astronomical Journal, 1977. **82**: p. 1013-1024.

34. Monaghan, J.J., *An introduction to SPH.* Computer Physics Communications, 1988. **48**(1): p. 89-96.

35. Monaghan, J.J., *Simulating Free Surface Flows with SPH.* Journal of Computational Physics, 1994. **110**(2): p. 399-406.

36. Chen, Y. and S. Kulasegaram, *Numerical modelling of fracture of particulate composites using SPH method.* Computational Materials Science, 2009. **47**(1): p. 60-70.

37. Shao, J.R., et al., *An improved SPH method for modeling liquid sloshing dynamics.* Computers & Structures, 2012. **100**(Supplement C): p. 18-26.

38. Nayroles, B., G. Touzot, and P. Villon, *Generalizing the finite element method: Diffuse approximation and diffuse elements.* Computational Mechanics, 1992. **10**(5): p. 307-318.

39. Breitkopf, P., et al., *Integration constraint in diffuse element method.* Computer Methods in Applied Mechanics and Engineering, 2004. **193**(12): p. 1203-1220.

40. Belytschko, T., L. Gu, and Y.Y. Lu, *Fracture and crack growth by element free Galerkin methods.* Modelling and Simulation in Materials Science and Engineering, 1994. **2**(3A): p. 519.

41. Wing Kam Liu, S.J., Shaofan Li, Jonathan Adee, Ted Belytschko, *Reproducing kernel particle methods for structural dynamics.* International Journal for Numerical Methods in Engineering, 1995. **38**: p. 1655-1679.

42. Liu, W.K., et al., *Generalized multiple scale reproducing kernel particle methods.* Computer Methods in Applied Mechanics and Engineering, 1996. **139**(1): p. 91-157.

43. Uras, R.A., et al., *Multiresolution Reproducing Kernel Particle Methods in Acoustics.* Journal of Computational Acoustics, 1997. **05**(01): p. 71-94.

44. Wagner, G.J. and W.K. Liu, *Turbulence simulation and multiple scale subgrid models.* Computational Mechanics, 2000. **25**(2): p. 117-136.

45. Oñate, E., et al., *A stabilized finite point method for analysis of fluid mechanics problems.* Computer Methods in Applied Mechanics and Engineering, 1996. **139**(1): p. 315-346.

46. Atluri, S.N. and T. Zhu, *A new Meshless Local Petrov-Galerkin (MLPG) approach in computational mechanics.* Computational Mechanics, 1998. **22**(2): p. 117-127.

47. Atluri S.N., S.S., *The Meshless Local Petrov-Galerkin (Mlpg) Method: A Simple & Less-Costly Alternative To The Finite Element And Boundary Element Methods.* Cmes-Computer Modeling In Engineering And Sciences 2002. **3**: p. 11-51.

48. Kansa, E.J., *Multiquadrics—A scattered data approximation scheme with applications to computational fluid-dynamics—II solutions to parabolic, hyperbolic and elliptic partial differential equations.* Computers & Mathematics with Applications, 1990. **19**(8): p. 147-161.

49. Lee, C.K., X. Liu, and S.C. Fan, *Local multiquadric approximation for solving boundary value problems.* Computational Mechanics, 2003. **30**(5): p. 396-409.

50. Buhmann, M.D., *Radial basis functions.* Acta Numerica, 2001. **9**: p. 1-38.

51. Flyer, N., et al., *A guide to RBF-generated finite differences for nonlinear transport: Shallow water simulations on a sphere.* Journal of Computational Physics, 2012. **231**(11): p. 4078-4095.

52. Soheil Soleimani, D.D.G., Esmaiil Ghasemi,Maziar Jalaal, *Meshless Local rbf-dq for 2-d Heat Conduction: a Comparative Study.* Thermal Science, 2011. **15**: p. s117-s121.

53. Y.T.Gu, G.R.L.a., *A point interpolation method for two dimensional solids.* Int. J. Numer. Methods Eng, 2001. **50**: p. 937-951.

54. Gu, Y.T. and G.R. Liu, *A boundary point interpolation method for stress analysis of solids.* Computational Mechanics, 2002. **28**(1): p. 47-54.

55. G.R.Liu, *Mesh Free Methods Moving Beyond the Finite Element Method*. 2003, USA: CRC Press.

56. Wen, P.H. and M.H. Aliabadi, *An improved meshless collocation method for elastostatic and elastodynamic problems.* Communications in Numerical Methods in Engineering, 2008. **24**(8): p. 635-651.

57. Li, M., et al., *Frictional contact analysis of functionally graded materials with Lagrange finite block method.* International Journal for Numerical Methods in Engineering, 2015. **103**(6): p. 391-412.

58. Li, M., et al., *Finite block Petrov–Galerkin method in transient heat conduction.* Engineering Analysis with Boundary Elements, 2015. **60**: p. 106-114.

59. Li, M., et al., *Finite block method for interface cracks.* Engineering Fracture Mechanics, 2016. **156**: p. 25-40.

60. Li, M., et al., *Post buckling analysis for composite plate by finite block Petrov-Galerkin method.* European Journal of Mechanics - A/Solids, 2017. **61**: p. 443-455.

61. Jeffreys, H.a.J., B.S., *Lagrange's Interpolation Formula.* Methods of Mathematical Physics, 1988: p. 260.

62. Aliabadi, M.H., *The Boundary Element, Application in Solids and Structures*. 2002, Chichester, England: John Wiley and Sons,Ltd.

63. Suresh S, M.A., *Fundamentals of functionally graded materials*. 1998, London: IOM communications.

64. Y. Miyamoto, W.A.K., B.H. Rabin, A. Kawasaki,R.G. Ford R, *Functionally Graded Materials*. 1999, Boston: Kluwer Academic Publishers.

65. Udupa, G., S.S. Rao, and K.V. Gangadharan, *Functionally Graded Composite Materials: An Overview.* Procedia Materials Science, 2014. **5**: p. 1291-1299.

66. Mahamood, R.M. and E.T. Akinlabi, *Laser metal deposition of functionally graded Ti6Al4V/TiC.* Materials & Design, 2015. **84**: p. 402-410.

67. Thieme, M., et al., *Titanium powder sintering for preparation of a porous functionally graded material destined for orthopaedic implants.* Journal of Materials Science: Materials in Medicine, 2001. **12**(3): p. 225-231.

68. Miao, X. and D. Sun, *Graded/Gradient Porous Biomaterials.* Materials, 2009. **3**(1): p. 26-47.

69. R.C.BATRA, Z.H.J.a., *Some basic fracture mechanics concepts in FGMs.* J.Mech.Phys.Solids, 1996. **44**(8): p. 1221-1235.

70. Eischen, J.W., *Fracture of nonhomogeneous materials.* International Journal of Fracture, 1987. **34**(1): p. 3-22.

71. Anlas, G., M.H. Santare, and J. Lambros, *Numerical Calculation of Stress Intensity Factors in Functionally Graded Materials.* International Journal of Fracture, 2000. **104**(2): p. 131-143.

72. Li, H., et al., *Experimental investigation of the quasi-static fracture of functionally graded materials.* International Journal of Solids and Structures, 2000. **37**(27): p. 3715-3732.

73. Marur, P.R. and H.V. Tippur, *Numerical analysis of crack-tip fields in functionally graded materials with a crack normal to the elastic gradient.* International Journal of Solids and Structures, 2000. **37**(38): p. 5353-5370.

74. Kim, J.-H. and G.H. Paulino, *Isoparametric Graded Finite Elements for Nonhomogeneous Isotropic and Orthotropic Materials.* Journal of Applied Mechanics, 2002. **69**(4): p. 502-514.

75. Ayhan, A.O., *Stress intensity factors for three-dimensional cracks in functionally graded materials using enriched finite elements.* International Journal of Solids and Structures, 2007. **44**(25-26): p. 8579-8599.

76. Ayhan, A.O., *Three-dimensional mixed-mode stress intensity factors for cracks in functionally graded materials using enriched finite elements.* International Journal of Solids and Structures, 2009. **46**(3-4): p. 796-810.

77. Sollero, P. and M.H. Aliabadi, *Fracture mechanics analysis of anisotropic plates by the boundary element method.* International Journal of Fracture, 1993. **64**(4): p. 269-284.

78. Yue, Z.Q., H.T. Xiao, and L.G. Tham, *Boundary element analysis of crack problems in functionally graded materials.* International Journal of Solids and Structures, 2003. **40**(13-14): p. 3273-3291.

79. Zhang, C., et al., *Transient dynamic analysis of a cracked functionally graded material by a BIEM.* Computational Materials Science, 2003. **26**: p. 167-174.

80. Zhang, C., J. Sladek, and V. Sladek, *Antiplane crack analysis of a functionally graded material by a BIEM.* Computational Materials Science, 2005. **32**(3-4): p. 611-619.

81. Gao, X., et al., *Fracture analysis of functionally graded materials by a BEM.* Composites Science and Technology, 2008. **68**(5): p. 1209-1215.

82. Sladek, J., V. Sladek, and C. Zhang, *An advanced numerical method for computing elastodynamic fracture parameters in functionally graded materials.* Computational Materials Science, 2005. **32**(3-4): p. 532-543.

83. Sladek, J., V. Sladek, and C. Zhang, *A meshless local boundary integral equation method for dynamic anti-plane shear crack problem in functionally graded materials.* Engineering Analysis with Boundary Elements, 2005. **29**(4): p. 334-342.

84. Jan Sladek, V.S., Chuangzeng Zhang, Choon-Lai Tan, *Evaluation of fracture parameters for crack problems in fgm by a meshless method.* journal of theoretical and applied mechanics, 2006. **44**(3): p. 603-636.

85. Dai, B., et al., *The complex variable meshless local Petrov–Galerkin method for elastodynamic analysis of functionally graded materials.* Applied Mathematics and Computation, 2017. **309**: p. 17-26.

86. Wen, P.H., et al., *Displacement discontinuity method for cracked orthotropic strip: Dynamic.* Wave Motion, 2008. **45**(3): p. 293-308.

87. Nilsson, F., *Dynamic stress-intensity factors for finite strip problems.* International Journal of Fracture Mechanics, 1972. **8**(4): p. 403-411.

88. Erdogan, F., *Stress Intensity Factors.* Journal of Applied Mechanics, 1983. **50**(4b): p. 992-1002.

89. Williams, M.L., *On the stress distribution at the base of a stationary crack.* J. Appl. Mech.,Trans.ASME, 1957. **24(1)**: p. 109-114.

90. Melin, S., *The influence of the T-stress on the directional stability of cracks.* International Journal of Fracture, 2002. **114**(3): p. 259-265.

91. Smith, D.J., M.R. Ayatollahi, and M.J. Pavier, *On the consequences of T-stress in elastic brittle fracture.* Proceedings of the Royal Society A: Mathematical, Physical and Engineering Science, 2006. **462**(2072): p. 2415.

92. Fett, T., *A Green's function for T-stresses in an edge-cracked rectangular plate.* Engineering Fracture Mechanics, 1997. **57**(4): p. 365-373.

93. Fett, T., *T-stresses in rectangular plates and circular disks.* Engineering Fracture Mechanics, 1998. **60**(5): p. 631-652.

94. Fett, T., *Stress intensity factors and T-stress for single and double-edge-cracked circular disks under mixed boundary conditions.* Engineering Fracture Mechanics, 2002. **69**(1): p. 69-83.

95. Sladek, J. and V. Sladek, *Evaluations of the T-stress for interface cracks by the boundary element method.* Engineering Fracture Mechanics, 1997. **56**(6): p. 813-825.

96. Sladek, J., V. Sladek, and P. Fedelinski, *Integral formulation for elastodynamic T-stresses.* International Journal of Fracture, 1997. **84**(2): p. 103-116.

97. Sladek, J., et al., *Evaluation of the T-stress for cracks in functionally graded materials by the FEM.* Theoretical and Applied Fracture Mechanics, 2016. **86**: p. 332-341.

98. Fett, T., *Stress intensity factors, T-stresses, weight functions*. 2008, Karlsruhe, Germany: University of Karlsruhe.

99. Chang-chun, W., H. Peixiang, and L. Ziran, *Extension of J integral to dynamic fracture of functional graded material and numerical analysis.* Computers & Structures, 2002. **80**(5): p. 411-416.

100. Song, S.H. and G.H. Paulino, *Dynamic stress intensity factors for homogeneous and smoothly heterogeneous materials using the interaction integral method.* International Journal of Solids and Structures, 2006. **43**(16): p. 4830-4866.

101. Sukumar, N., et al., *Extended finite element method for three-dimensional crack modelling.* International Journal for Numerical Methods in Engineering, 2000. **48**(11): p. 1549-1570.

102. Motamedi, D. and S. Mohammadi, *Dynamic analysis of fixed cracks in composites by the extended finite element method.* Engineering Fracture Mechanics, 2010. **77**(17): p. 3373-3393.

103. Fedelinski, P., M.H. Aliabadi, and D.P. Rooke, *A single-region time domain BEM for dynamic crack problems.* International Journal of Solids and Structures, 1995. **32**(24): p. 3555-3571.

104. Albuquerque, E.L., P. Sollero, and M.H. Aliabadi, *The boundary element method applied to time dependent problems in anisotropic materials.* International Journal of Solids and Structures, 2002. **39**(5): p. 1405-1422.

105. Belytschko, T., et al., *Element-free galerkin methods for static and dynamic fracture.* International Journal of Solids and Structures, 1995. **32**(17): p. 2547-2570.

106. Sladek, J., Sladek, V., Zhang, Ch, Solek, P., Pan, E., *Evaluation of fracture parameters in continuously nonhomogeneous piezoelectric solids.* International Journal of Fracture, 2007. **145**(4): p. 313-326.

107. F, D., *Numerical inversion of Laplace transforms: an efficient improvement to Dubner and Abate's method*. Vol. 17(4). 1974: Comput J. 371-6.

108. Deng, X., *The asymptotic structure of transient elastodynamic fields at the tip of a stationary crack.* Proceedings of the Royal Society of London. Series A: Mathematical and Physical Sciences, 1994. **446**(1926): p. 1.

109. Biot, M.A., *Theory of Propagation of Elastic Waves in a Fluid‐Saturated Porous Solid. I. Low‐Frequency Range.* The Journal of the Acoustical Society of America, 1956. **28**(2): p. 168-178.

110. Biot, M.A., *Theory of Propagation of Elastic Waves in a Fluid‐Saturated Porous Solid. II. Higher Frequency Range.* The Journal of the Acoustical Society of America, 1956. **28**(2): p. 179-191.

111. F.Wang, H., *Theory of Linear Poroelasticity with Applications to Geomechanics and Hydrogeology*. 2000: Princeton University Press.

112. Cowin, S.C., *Bone poroelasticity.* Journal of Biomechanics, 1999. **32**(3): p. 217-238.

113. Stephen C. Cowin, S.B.D., *Tissue Mechanics*. 2007: Springer New York.

114. Luc Dormieux, D.K., Franz-Josef Ulm, *Microporomechanics*. 2006: John Wiley & Sons, Ltd.

115. Barry, S.I., K.H. Parkerf, and G.K. Aldis, *Fluid flow over a thin deformable porous layer.* Zeitschrift für angewandte Mathematik und Physik ZAMP, 1991. **42**(5): p. 633-648.

116. Schanz, M. and A.H.D. Cheng, *Transient wave propagation in a one-dimensional poroelastic column.* Acta Mechanica, 2000. **145**(1): p. 1-18.

117. Xue, C. and J. Nie, *Exact solutions of the Rayleigh–Stokes problem for a heated generalized second grade fluid in a porous half-space.* Applied Mathematical Modelling, 2009. **33**(1): p. 524-531.

118. Wen, P.H., Y.C. Hon, and W. Wang, *Dynamic responses of shear flows over a deformable porous surface layer in a cylindrical tube.* Applied Mathematical Modelling, 2009. **33**(1): p. 423-436.

119. Wilson, J.G.a.E.L., *Variational formulation of dynamics of fluid-saturated porous elastic solids.* J. Engrg. Mech, 1972. **98**: p. 947-963.

120. Manfredini, P., et al., *Poroelastic finite element analysis of a bone specimen under cyclic loading.* Journal of Biomechanics, 1999. **32**(2): p. 135-144.

121. Zyserman, F.I. and J.E. Santos, *Analysis of the numerical dispersion of waves in saturated poroelastic media.* Computer Methods in Applied Mechanics and Engineering, 2007. **196**(45-48): p. 4644-4655.

122. Lee, J.S., et al., *A direct hybrid finite element–wave based modelling technique for efficient analysis of poroelastic materials in steady-state acoustic problems.* Computer Methods in Applied Mechanics and Engineering, 2016. **304**: p. 55-80.

123. Brady, B.H.G. and J.W. Bray, *The boundary element method for determining stresses and displacements around long openings in a triaxial stress field.* International

Journal of Rock Mechanics and Mining Sciences & Geomechanics Abstracts, 1978. **15**(1): p. 21-28.

124. Abousleiman, Y. and A.H.D. Cheng, *Boundary element solution for steady and unsteady Stokes flow.* Computer Methods in Applied Mechanics and Engineering, 1994. **117**(1): p. 1-13.

125. Schanz, M., *Application of 3D time domain boundary element formulation to wave propagation in poroelastic solids.* Engineering Analysis with Boundary Elements, 2001. **25**(4): p. 363-376.

126. Pryl, D. and M. Schanz, *Comparison of mixed and isoparametric boundary elements in time domain poroelasticity.* Engineering Analysis with Boundary Elements, 2006. **30**(4): p. 254-269.

127. Park, K.H. and P.K. Banerjee, *Two- and three-dimensional soil consolidation by BEM via particular integral.* Computer Methods in Applied Mechanics and Engineering, 2002. **191**(29): p. 3233-3255.

128. Wang, J.G., G.R. Liu, and Y.G. Wu, *A point interpolation method for simulating dissipation process of consolidation.* Computer Methods in Applied Mechanics and Engineering, 2001. **190**(45): p. 5907-5922.

129. Wang, J.G., G.R. Liu, and P. Lin, *Numerical analysis of Biot's consolidation process by radial point interpolation method.* International Journal of Solids and Structures, 2002. **39**(6): p. 1557-1573.

130. Ferronato, M., et al., *A meshless method for axi-symmetric poroelastic simulations: numerical study.* International Journal for Numerical Methods in Engineering, 2007. **70**(11): p. 1346-1365.

131. Wen, P.H., *Meshless local Petrov–Galerkin (MLPG) method for wave propagation in 3D poroelastic solids.* Engineering Analysis with Boundary Elements, 2010. **34**(4): p. 315-323.

Appendix

Appendix 1. A Brief Introduction

Abaqus is a very powerful package with different algorithms that are tailored to solve different types of problems ranging from simple linear or static analysis to the most challenging nonlinear analysis. Therefore, it is extensively used in both routine and sophisticated engineering problems covering a vast spectrum of industrial applications. When a model is created and analyzed, a set of files is generated in Abaqus/CAE which contain the definition of the model, the analysis input, and the results of the analysis. Three types of models can be created in Abaqus/CAE, including Standard & Explicit, CFD, and Electromegnetic. In this report, a standard model with crack is proposed, incorporating with a subroutine UMAT.

UMAT, with Abaqus/Standard, is used to define the mechanical constitutive behavior of a material, and will be called at all material calculation points of elements for which the material definition includes a user-defined material behavior. For any procedure that includes mechanical behavior, UMAT can be utilized. The stresses and solution-dependent state variables to their values at the end of the increment for which it is called have to be updated. The material Jacobian matrix, $\partial\Delta\sigma/\partial\Delta\varepsilon$, for the mechanical constitutive model has to be provided.

Appendix 2 The Study of Input File

In this section, the working scheme of input file for a comprehensive understanding ABAQUS is introduced as follows:

1) Heading Information

```
*Heading
** Job name: FGMSCRACK Model name: Model-1
```

2) Node Definition

```
*Node
      1,          -5., -0.100000001
      2,  0.899999976, -0.100000001
      3,          -1.,           0.
      4,           0.,           0.
      5,  0.899999976,           0.
```

3) Element Definition

```
*Element, type=CPS8R
  1,    1,   32,  806,  163, 4791, 4792, 4793, 4794
  2,   32,   33,  807,  806, 4795, 4796, 4797, 4792
  3,   33,   34,  808,  807, 4798, 4799, 4800, 4796
  4,   34,   35,  809,  808, 4801, 4802, 4803, 4799
```

4) Defining Sets

```
*Nset, nset=_PickedSet2, internal, generate
     1,  14204,      1
*Elset, elset=_PickedSet2, internal, generate
    1,  4624,     1
```

5) Materials Definition

```
** MATERIALS
**
*Material, name=Material-1
*Density, dependencies=1
```

6) Defining Steps

```
** STEP: Step-2
**
*Step, name=Step-2, nlgeom=NO, inc=5000
*Dynamic,direct
0.01,50.,
**
```

7) Boundary Conditions

```
** BOUNDARY CONDITIONS
**
** Name: BC-3 Type: Displacement/Rotation
*Boundary
_PickedSet27, 2, 2
** Name: BC-4 Type: Displacement/Rotation
*Boundary
_PickedSet28, 1, 1
_PickedSet28, 2, 2
_PickedSet28, 6, 6
```

8) Loads

```
** LOADS
**
** Name: Load-2   Type: Pressure
*Dsload
```

9) Output Requests

```
** OUTPUT REQUESTS
**
*Restart, write, frequency=0
**
** FIELD OUTPUT: F-Output-2
**
*Output, field, frequency=1
*Node Output
A, U, V
```

10) End Step

```
*End Step
```

Appendix 3 Subroutine UMAT

```
      INCLUDE 'ABA_PARAM.INC'
      CHARACTER*80 CMNAME
      DIMENSION STRESS(NTENS),STATEV(NSTATV),
     1 DDSDDE(NTENS,NTENS),DDSDDT(NTENS),DRPLDE(NTENS),
     2 STRAN(NTENS),DSTRAN(NTENS),TIME(2),PREDEF(1),DPRED(1),
     3 PROPS(NPROPS),COORDS(2)


      PARAMETER(ONE=1.D0,TWO=2.D0,ZERO=0.D0)
        open(unit=101,file='E:\WORKS\SIMULIA\datafile\umatdata.dat')
      X=COORDS(1)
      Y=COORDS(2)
      write(101,*) KSTEP,KINC,DTIME
      E0=PROPS(1)
      ANU=PROPS(2)
      DENSITY=PROPS(3)
      ALFA=PROPS(3)
      BETA=PROPS(4)


      E=E0*EXP(ALFA*X+BETA*Y)
      ALAMBDA=E*(ONE-ANU)/(ONE+ANU)/(ONE-TWO*ANU)
      AG=E/(ONE+ANU)/TWO
      DO I=1,NTENS
       DO J=1,NTENS
       DDSDDE(I,J)=0.0D0
       ENDDO
      ENDDO


        DDSDDE(1,1)=E*8.38*5.5
        DDSDDE(1,2)=E*0.52*5.5
        DDSDDE(1,3)=0.0
        DDSDDE(2,1)=E*0.52*5.5
        DDSDDE(2,2)=E*2.29*5.5
        DDSDDE(2,3)=0.0
        DDSDDE(3,1)=0.0
        DDSDDE(3,2)=0.0
        DDSDDE(3,3)=E*5.5


          DO J=1,NTENS
          STRESS(1)=STRESS(1)+DDSDDE(1,J)*DSTRAN(J)
          STRESS(2)=STRESS(2)+DDSDDE(2,J)*DSTRAN(J)
          STRESS(3)=STRESS(3)+DDSDDE(3,J)*DSTRAN(J)
          ENDDO
       RETURN
       END
```